Experimental and numerical investigations of propeller open water characteristics in calm water and regular head waves

Ocean Engineering 302 (2024) 117703

Contents lists available at ScienceDirect

Ocean Engineering

journal homepage: www.elsevier.com/locate/oceaneng

Experimental and numerical investigations of propeller open water characteristics in calm water and regular head waves

Mohsen Irannezhad [a,*], Martin Kjellberg [b], Rickard E. Bensow [a], Arash Eslamdoost [a]

[a] Department of Mechanics and Maritime Sciences, Chalmers University of Technology, 412 96, Gothenburg, Sweden
[b] RISE - SSPA Maritime Center, 412 58, Gothenburg, Sweden

ARTICLE INFO

Keywords:
EFD
CFD
Thrust
Torque
Regular head waves
Verification and validation

ABSTRACT

Propeller Open Water (POW) performance of a non-ventilating and fully-submerged propeller in model-scale is investigated in calm water and regular head waves using experimental tests (EFD) and Computational Fluid Dynamics (CFD). Laminar flow dominance is observed in calm water, particularly at higher advance ratios. Nevertheless, the findings in waves suggest increased turbulence, stemming from both the wave orbital velocities and the presumably increased turbulence level produced by the wave maker in the towing tank. Analysis of the CFD results obtained from the incident flow field and single-blade force and moment leads to the speculation that the observed discrepancies are associated with the inevitable asymmetric conditions and mechanical interference in the experiments which were absent in CFD. These can potentially alter the flow over the blades resulting in a different flow transition, separation, and coherent turbulent structure formation and hence forces and moments. The altered propeller performance in waves in comparison to calm water underlines the significance of waves on the propulsive factors and propeller design.

1. Introduction

Today, there is a growing tendency to study the hydrodynamic performance of ships in more realistic environmental conditions rather than traditional calm water considerations. Waves are playing a crucial role on the ship performance in an actual seaway. The interactions between waves, hull and the propulsion system of a ship may significantly affect the ship motions, resistance, wake and propeller/engine load in comparison to calm water operational conditions, ITTC (2017). It is well-established, e.g., by Gerritsma et al. (1961), Moor and Murdey (1970), Van Sluijs (1972) and Nakamura and Naito (1975), that the propulsive factors for ships operating in waves deviate from those in calm water, which may lead to a noticeable ship performance degradation.

While the operational condition for a ship's propeller in real seas is inherently complex due to the ship motions and wake variations, it remains necessary to study the propeller performance under controlled operational conditions to gain insights into performance deviations in complex in behind conditions. These controlled operational conditions for the propeller without the hull interactions are often called "open water" in the context of marine engineering and propulsion.

Evaluation of the Propeller Open Water (POW) performance is essential because it provides primary insights into the propeller's performance characteristics such as thrust, torque and efficiency. The POW performance has been widely investigated experimentally and numerically. The common experimental approaches, which are known as Experimental Fluid Dynamics (EFD), are the performance predictions using model tests, for example in towing tanks or cavitation tunnels. These experiments are called POW tests henceforth. Although the POW tests are expensive and time-consuming, often they provide a high level of accuracy in the predictions of the POW characteristics.

There are numerous studies on the evaluation of the POW performance through numerical methods. Generally, one major advantage of numerical methods over the POW tests is the possibility of acquiring in-depth information about the fluid flow, which is challenging, costly, and extremely cumbersome to achieve through the tests, if even possible. Each numerical method has a different level of fidelity with respect to its computational costs and accuracy. Generally, the approach in these methods is based on either Potential Flow methods (Vortex Methods or Three-Dimensional Panel Methods) or Computational Fluid Dynamics (CFD) techniques. The benefit of using state-of-the-art CFD methods lies in their more accurate predictions through high-fidelity nonlinear computations with fewer simplifications related to flow physics compared to the potential flow methods. However, CFD methods are often computationally expensive and time-consuming. Today, with the accessibility of large computational resources and the development of sophisticated computational tools, there is a growing

* Corresponding author.
E-mail address: mohsen.irannezhad@chalmers.se (M. Irannezhad).

https://doi.org/10.1016/j.oceaneng.2024.117703
Received 12 January 2024; Received in revised form 16 March 2024; Accepted 27 March 2024

Nomenclature

$(P/D)_{0.7R}$	Pitch ratio at $r/R = 0.7$ (–)
α	Multiplication constant in uncertainty analysis tool
$\alpha(r,\theta)$	Incidence angle at position (r,θ) on propeller disk (deg)
$\bar{\psi}$	Mean (time-averaged) of quantity under study in Fourier analysis
$\beta(r,\theta)$	Geometric advance angle at position (r,θ) on propeller disk (deg)
Δt	Time step (s)
δ_n	First layer cell thickness of prism layers in grid n (m)
η_O	Propeller open water efficiency (–)
γ_n	Growth ratio between layers of prism layers in grid n (–)
λ	Wave length (m)
μ	Heading angle (deg)
ν	Kinematic viscosity of water (m^2/s)
Ω	Propeller rotational angular velocity (rad/s)
ω	Fast Fourier Transform frequency (rad/s)
ω_E	Encounter wave frequency (rad/s)
ω_w	Wave frequency (rad/s)
Φ_0	Estimated exact solution in uncertainty analysis tool
Φ_i	Solution of the ith grid in uncertainty analysis tool
$\psi(t)$	Time series of the quantity under study in Fourier analysis
ψ_i	The ith harmonic amplitude of quantity under study in Fourier analysis
$\psi_{\epsilon i}$	The ith harmonic phase of quantity under study in Fourier analysis
ρ	Water density (kg/m^3)
θ	Azimuthal position on propeller disk (deg)
$\Theta(r)$	Geometric pitch angle at radius r on propeller disk (deg)
θ_{sk}	Skew angle (°)
ζ	Free surface elevation (m)
A	Wave amplitude $H/2$ (m)
A_E/A_O	Blade area ratio (–)
$C_{0.7R}$	Chord length at $0.7R$ (m)
D	Propeller diameter (m)
D_{hub}	Hub diameter (m)
Fr	Froude number (–)
g	Gravitational acceleration (m/s^2)
H	Wave height (m)
h_i	Typical cell size of the ith grid in uncertainty analysis tool
J	Advance ratio (–)
k	Wave number $360/\lambda$ (deg/m)
K_Q	Propeller torque coefficient (–)
K_T	Propeller thrust coefficient (–)
L	Length between perpendiculars (m)
n	Grid refinement level (–)
N_n	Total number of layers of prism layers in grid n (–)
n_P	Propeller rotational speed (rps)
p	Observed order of grid convergence in uncertainty analysis tool
Q	Propeller torque (N m)
$Q^{pressure}$	Pressure component of the torque around the axial axis of the Cartesian coordinate system (N m)
Q^{shear}	Shear component of the torque around the axial axis of the Cartesian coordinate system (N m)
Q_Y	Moment around the transversal axis of the Cartesian coordinate system (N m)
Q_Z	Moment around the vertical axis of the Cartesian coordinate system (N m)
R	Propeller radius (m)
r	Radial position on propeller disk (m)
R_{hub}	Hub radius (m)
Re	Reynolds number (–)
T	Propeller thrust (N)
t	Time (s)
$T^{pressure}$	Pressure component of the thrust in the axial axis of the Cartesian coordinate system (N)
T^{shear}	Shear component of the thrust in the axial axis of the Cartesian coordinate system (N)
T_E	Wave encounter period (s)
T_Y	Force in the transversal axis of the Cartesian coordinate system (N)
T_Z	Force in the vertical axis of the Cartesian coordinate system (N)
U	Ship velocity (m/s)
$u^{wave}_{axial}(r,\theta)$	Axial velocity component of the wave orbital velocities at position (r,θ) on propeller disk (m/s)
$u^{wave}_{vertical}(r,\theta)$	Vertical velocity component of the wave orbital velocities at position (r,θ) on propeller disk (m/s)
u_r	Radial velocity component at position (r,θ) on propeller disk (m/s)
u_θ	Azimuthal velocity component at position (r,θ) on propeller disk (m/s)
$u_{axial}(r,\theta)$	Axial velocity at position (r,θ) on propeller disk (m/s)
y^+	Non-dimensional wall distance for a wall-bounded flow (–)
η_{Oi}	The ith harmonic amplitude of open water efficiency at wave encounter frequency (–)
K_{Qi}	The ith harmonic amplitude of torque coefficient at wave encounter frequency (–)
K_{Ti}	The ith harmonic amplitude of thrust coefficient at wave encounter frequency (–)
$N_{cell\,i}$	Total number of cells of the ith grid in uncertainty analysis tool
SDR	Specific dissipation rate ($kg/m^3\ s^2$)
TKE	Turbulent kinetic energy ($kg/m\ s^3$)

trend towards utilization of CFD methods for the POW performance analysis, due to their capabilities in providing comprehensive flow field information. The so-called Reynolds-Averaged Navier–Stokes (RANS) approach is the most common CFD method in the context of ship hydrodynamics.

The vast majority of investigations in the literature are focused on assessing the POW performance in calm water conditions, and the identification of the effects of wave dynamics on the POW characteristics is seldom examined. Even when the effects of waves are taken into account, the studies predominantly concentrate on the propeller emergence and ventilation. Ventilation is a phenomenon where a propeller interacts with the free surface and pulls down air when it operates beneath the free surface, Califano and Steen (2011). This phenomenon depends on many conditions, such as the propeller loading, advance speed and the propeller submergence depth, i.e., the distance from the propeller to the free surface. For instance, the investigations carried out by Faltinsen et al. (1980), Minsaas et al. (1983), Politis (1999), Koushan et al. (2009), Xin (2012) and Eom et al. (2021a) are mainly focused on the ventilation occurrence and its effects on the POW characteristics in waves.

One of the initial investigations about the effects of waves on fully-submerged and non-ventilating propellers was carried out by McCarthy et al. (1961) through POW tests in calm water and regular head waves. It is illustrated that the fluctuations in the open water thrust and torque in regular head waves are in good agreement with the calm water uniform flow propeller performance curves, when the mean orbital velocities of the waves are taken into account in the advance ratio. Similar observations are also reported by Nakamura et al. (1975).

Although the experimental and numerical investigations performed by Zhao et al. (2017) on the POW performance in regular waves include the non-ventilating conditions, the main conclusions are made based on the propeller performance under ventilating conditions. Moreover, only one wave condition (wave length and height) is considered in this study, hence it lacks an assessment of the POW performance across various wave conditions.

Tokgoz et al. (2017) compared the CFD predictions of the POW performance in waves against the EFD data for two different propellers under various submergence depths, advance ratios and wave conditions. However, the discussions mainly focused on the propeller ventilation effects on the propeller performance and the discrepancies of the POW characteristics between the calm water and waves in the non-ventilating conditions are overlooked.

Jang et al. (2019, 2020) and Eom et al. (2021b) studied the POW performance in calm water and regular waves under various operational conditions, e.g., heaving propeller, pitching propeller, propeller with constant inclination angles and different submergence depths. The aim was to develop a performance prediction method for the propeller that follows the ship motions in waves. Although very interesting observations are reported in these investigations, they fail to illustrate a clear picture of the effects of different waves on the POW characteristics in comparison to calm water condition.

Kan et al. (2023) performed CFD investigations of the effects of waves on the propeller wake through the large-eddy simulation framework. In this study, the influences of incident waves on the propeller wake characteristics including turbulent kinetic energy and power spectral density are analyzed, but only in one wave condition.

Aside from the work by McCarthy et al. (1961), the studies by Zhang et al. (2021a,b) are among the most relevant investigations for the current paper, concerning the POW performance in waves. Although these studies are more focused on the ventilation effects from the perspective of the coupled oblique flow and free surface effects in various submergence depths, they include a brief analysis of the propeller performance in the non-ventilating condition. The dynamic behavior of the propeller thrust and torque, including the integral load variations in the entire period of encounter, single-blade load variations in different time intervals, as well as instantaneous loads at different azimuthal positions and instants are analyzed. It was concluded that, under the fully-submerged and non-ventilating condition, due to the wave orbital velocities, the propeller experiences non-uniform inflow with periodically varying magnitude and incidence angle. Therefore, the instantaneous load distribution on the propeller disk as well as the single-blade load variations are unsteady due to the non-uniform and unsteady oblique flow environment. The shortcomings of these investigations are the considerations of a limited number of wave conditions and advance ratios, hence lacking a complete analysis of the effects of waves in different operational conditions.

The main motivation behind this study stems from the limitations in current literature in offering comprehensive insights into the effects of waves on the POW performance in various operational conditions for propellers under fully-submerged and non-ventilating conditions. The key objective of the current paper is to perform systematic experimental and numerical (RANS) investigations of POW performance in calm water and regular head waves to study the impacts of waves on the POW characteristics of a propeller. The KP458 propeller, originally designed for the KVLCC2 tanker, is chosen as the case study in this paper. The choice of regular head waves is made because of their comparatively simpler effects on the POW performance and the involved flow physics. In order to obtain the objectives, the POW performance is studied in a wide range of operational conditions consisting of different advance ratios and wave conditions (wave heights and wave lengths), in which the effects of different contributing factors are studied. The submergence effects are also examined briefly through the comparison of the POW performance in waves between two different submergence depths. The advance ratios, wave conditions and submergence depths are selected to avoid propeller ventilation and remain fully-submerged during the whole encounter period, while still being affected by the incident waves.

The investigations include analysis of the instantaneous, time-averaged and harmonic amplitudes of propeller thrust, torque and efficiency as well as the single-blade load variations together with an incident flow field analysis from the numerical methods. To this end, suitable convergence criteria and post-processing techniques are utilized and then a formal verification and validation (V & V) procedure is applied to understand and control the numerical and modeling uncertainties/errors in the CFD computations. Verification is a purely mathematical exercise that intends to show that we are solving the equations right, whereas validation is an engineering practice that intends to show that we are solving the right equations, Roache (1998). In this paper, the main focus of such verification (uncertainty analysis) is on systematic grid convergence study. The POW performance analyses from this paper can shed more light onto the propeller–wave interaction effects and help the ship/propeller designers optimize their designs for more realistic environmental conditions than only calm water.

2. Propeller geometry and operational conditions

The employed propeller geometry in this study is the KP458, originally designed by Korea Research Institute of Ships and Ocean Engineering (KRISO, formerly MOERI) for the second variant of the MOERI tanker (KVLCC2). The propeller in model-scale with the scale factor of approximately 45.714 appended with a shaft and a dummy hub cap is considered. The main particulars of the propeller geometry are given in Table 1.

The Propeller Open Water (POW) performance operating in fresh water with the density of $\rho = 998.83$ kg/m^3 and the kinematic viscosity of $\nu = 1.089 \times 10^{-6}$ m^2/s is investigated. Different advance ratios $J = U/(n_P D)$ are considered, in which U is the advance velocity (carriage velocity in the POW model tests) and n_P is the propeller rotational speed in revolution per second rps. The design Froude number of the KVLCC2 hull is $Fr = U/\sqrt{gL} = 0.142$, hence resulting in the design ship speed of approximately 1.177 m/s for the $L = 7$ m long hull with the same scale factor as of propeller (≈45.714). Although a wide range of

Table 1
Main particulars of the propeller geometry in model-scale (scale factor ≈ 45.714).

Symbol	Value/Type	Unit	Denotation
D	0.2157	(m)	Propeller diameter
D_{hub}	$0.155D$	(m)	Hub diameter
$(P/D)_{0.7R}$	0.721	(–)	Pitch ratio at $r/R = 0.7$
A_E/A_O	0.431	(–)	Blade area ratio
θ_{sk}	21.15	(°)	Skew angle
$C_{0.7R}$	0.0494	(m)	Chord length at $r/R = 0.7$
–	4	(–)	Number of blades
–	FPP	(–)	Fixed Pitch Propeller type
–	Right-handed	(–)	Rotation direction

Table 2
Intended wave conditions from the wave calibration tests. The length of $L = 7$ m and the carriage speed of $U = 1.177$ m/s are used to calculate the non-dimensional wave lengths λ/L and the wave encounter periods T_E.

Wave condition	λ (m)	λ/L (–)	H (m)	H/λ (%)	T_E (s)
WC1	3.990	0.570	0.042	1.052	1.086
WC2	3.990	0.570	0.070	1.754	1.086
WC3	3.990	0.570	0.120	3.007	1.086
WC4	7.546	1.078	0.133	1.762	1.637

advance ratios is considered in calm water, the investigations in regular head waves mainly concern the advance ratios of $J \approx 0.35$, 0.45, 0.55 and 0.60, by considering $U = 1.177$ m/s and propeller rotational speeds of $n_P = 15.62$ rps, 12.15 rps, 9.94 rps and 9.11 rps, respectively.

The investigations are carried out in calm water and four regular head waves, including two different wave lengths λ and different wave heights H or steepnesses H/λ. Prior to the POW tests in waves, the wave calibration tests are carried out to examine the quality of the generated waves with regard to the wave maker's performance and its limitations and to document the characteristics of the actually generated waves. Table 2 provides the wave conditions results from the wave calibration tests. These are the four wave conditions that are used for the POW tests as well as the simulations. All the experimental and numerical POW studies in regular head waves are carried out with a constant carriage speed of $U = 1.177$ m/s, in order to be consistent with the KVLCC2 design Froude number. In Table 2, the non-dimensional wave lengths λ/L are given using the length of $L = 7$ m. The wave encounter frequency ω_E and encounter period T_E are computed for each wave length based on its respective wave frequency ω_w, heading angle $\mu = 180°$ and the carriage speed of $U = 1.177$ m/s as,

$$\omega_E = \omega_w - \frac{{\omega_w}^2 U}{g}\cos(\mu), \qquad T_E = 2\pi/\omega_E. \tag{1}$$

The majority of the investigations are carried out for the propeller in $3R$ submergence depth (distance of the propeller center to the undisturbed free surface, i.e., mean water level in calm water and waves), while a few studies are performed in $2R$ submergence depth in order to study the effects of submergence on the propeller performance. Both submergence depths are chosen in order to avoid propeller ventilation in the considered propeller operational conditions, while still being affected by the encountered waves.

3. Experimental method

The propeller open water model tests are carried out at the SSPA towing tank with a length of 260 m, breadth of 10 m, and depth of 5 m. The tank is equipped with a flap-type wave maker, capable of generating regular and irregular waves longer than 0.4 m (up to 2 Hz frequency) and up to 0.3 m height. The POW test setup is shown in Fig. 1. A load cell dynamometer, with the range of 700 N and 80 N m transducers, is installed between the shaft and the motor inside the "hull" of the POW device for the thrust and torque measurements. The incident wave height was measured by a linear servo-actuated rod wave gauge installed on the carriage at a distance of 4.68 m in front of the propeller. The actual measured incident wave length and height in each test may deviate from the expected waves given in Table 2 derived from the wave calibration tests, because of the performance of the wave generator and wave dampener systems in the tank. This will be addressed in Section 6. The sampling rate of the equipment in all measurements is 100 Hz.

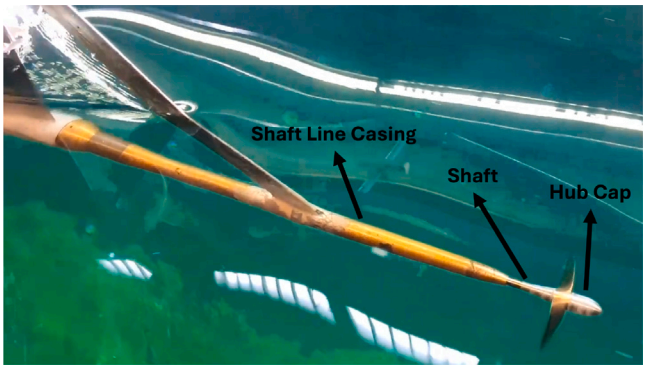

Fig. 1. Propeller geometry and POW test setup.

Although a wide range of advance ratios are tested in each carriage run (from the start to the end of the towing tank) in calm water, only two advance ratios are tested in each carriage run in regular head waves. The quality of the generated waves might be different depending on the distance between the carriage and the wave generator. Therefore, some POW tests in waves are repeated in the swapped order of advance ratios in the same wave condition to account for such uncertainties. To mitigate the disturbances in the tank, a 30-min pause was allocated between consecutive runs.

4. Numerical method

The continuity and momentum equations, commonly referred to as the Navier–Stokes equations, are the governing equations of a fluid flow derived from the basic laws of mass and momentum conservation. For Newtonian fluids, the Reynolds-Averaged Navier–Stokes (RANS) equations of incompressible viscous flow are derived from the Navier–Stokes equations through the Reynolds decomposition of pressure and velocity by time-averaged ($\overline{P}$ and $\overline{U_i}$) and fluctuating (p and u_i) quantities as,

$$P = \overline{P} + p, \qquad U_i = \overline{U_i} + u_i. \tag{2}$$

The RANS equations are then expressed as,

$$\frac{\partial \overline{U_i}}{\partial x_i} = 0,$$
$$\frac{\partial \overline{U_i}}{\partial t} + \overline{U_j}\frac{\partial \overline{U_i}}{\partial x_j} = -\frac{1}{\rho}\frac{\partial \overline{P}}{\partial x_i} + \nu\frac{\partial^2 \overline{U_i}}{\partial x_j \partial x_j} + g_i - \frac{\partial \overline{u_i u_j}}{\partial x_j}, \tag{3}$$

in which i and j are the Cartesian coordinates, ρ is the density, t is time, ν is the kinematic viscosity of the fluid and g_i represents the gravitational acceleration and is presumed to be the only body force considered in this equation. In this study, a closure equation for these partial differential RANS equations is acquired from modeling the Reynolds stress $\overline{u_i u_j}$ by an Eddy Viscosity model, i.e., Boussinesq's hypothesis, assuming $\overline{u_i u_j}$ to be proportional to the mean strain rate tensor. A linear constitutive relation is considered in the original Boussinesq's hypothesis as,

$$-\overline{u_i u_j} = \nu_t\left(\frac{\partial \overline{U_i}}{\partial x_j} + \frac{\partial \overline{U_j}}{\partial x_i}\right) - \frac{2}{3}k\delta_{ij}, \tag{4}$$

in which k is the turbulent kinetic energy, δ_{ij} is the Kronecker delta and ν_t is the turbulent viscosity, i.e., the factor of proportionality. Additional transport equations for other scalar quantities can be solved to obtain ν_t.

In the current study, a commercial CFD solver, Simcenter STAR-CCM+ (version 2020.3), is employed to perform the numerical simulations applying a RANS approach. A Finite Volume method is used to discretize the continuous equations, where a second-order spatial discretization scheme is considered. The conservation equations for mass, momentum and turbulence quantities are solved using a segregated approach for coupling velocity and pressure fields.

Additional transport equations for turbulent kinetic energy k (TKE) and specific dissipation rate ω (SDR) are solved to model ν_t through the $k-\omega$ SST turbulence model (with all y^+ wall treatment consideration) implemented according to Menter (1994). In the current study, the linear Boussinesq's hypothesis, shown in Eq. (4), is extended by adding nonlinear functions of the strain and vorticity tensors to obtain a quadratic constitutive relation and hence, taking into consideration the anisotropy of the turbulence. More information can be found in Simcenter STAR-CCM+ User Guide (2020).

The free surface is modeled using the Volume of Fluid (VOF) multiphase model in which the High-Resolution Interface Capturing scheme (HRIC) by Muzaferija and Perić (1998) is employed to preserve a sharp interface between the incompressible fluid phases. The 5th order Stokes waves are used in the regular head wave simulations, as they were found to be a better resemblance of the real-world waves, Fenton (1985).

In both experimental tests and numerical simulations, acquiring high-quality regular waves is a recognized challenge, as also discussed in ITTC (2021b,c) and Tavakoli et al. (2023). An extensive study has been performed by Irannezhad et al. (2021) and Irannezhad (2022) to investigate the modeling errors involved in the simulation of wave propagation and obtain a robust simulation setup for wave propagation in the employed solver. The goal was to diminish the wave propagation modeling errors, for instance, change of wave amplitude and period during propagation, wave reflection at the boundaries of the computational domain and presence of disturbances (wiggles) on the free surface. Perić and Abdel-Maksoud (2018, 2020), Berndt et al. (2021) and Perić et al. (2022) also suggested the tuning of the case-dependent simulation parameters to enhance the numerical wave propagation simulations.

In the aforementioned wave propagation investigations by Irannezhad et al. (2021), various user-defined simulation parameters were tuned in order to minimize the reflections from the boundaries. An example of such optimizations is the consideration of the angle factor of 0.15 under the HRIC scheme which influences the discretization of the volume fraction. Moreover, various effects originated from the quality of the cell size, local refinement zones and overset interpolations were evaluated and the discrepancies of the numerical wave from the analytical wave were examined. As a result, the numerical configuration proposed in Irannezhad et al. (2021) yielded numerical waves that closely resembled the analytical counterpart, in which the discrepancies of the 1st harmonic amplitude (i.e., the dominant harmonic component) remained primarily under 3%.

The flexibility and hydroelasticity of the propeller in the simulations are deemed negligible as the propeller is presumed to be rigid.

4.1. Transition modeling

A transition model is needed in the employed CFD approach to capture the phenomenon of laminar–turbulent transition in the boundary layer of the model-scale propeller. In this paper, the $\gamma - Re_\theta$ transition model is employed whenever a simulation is conducted including transition. Information about this transition model and its implementation in STAR-CCM+ can be found in Menter et al. (2004), Langtry (2006), Malan et al. (2009) and Simcenter STAR-CCM+ User Guide (2020). This transition model is a two-equation, correlation-based transition model that provides a semi-local approach to predict the onset of transition. The model in combination with the $k-\omega$ SST turbulence model predicts the onset of transition by solving additional transport equations for the intermittency γ and the transition momentum thickness Reynolds number $\overline{Re_\theta}$ that are coupled with the turbulence model through incorporating them into the transport equation for turbulent kinetic energy. Intermittency is a measure of the amount of time during which the flow is turbulent. An intermittency value of 1 corresponds to a fully turbulent flow (100% of the time) and an intermittency value of 0 corresponds to a fully laminar flow.

The sensitivity of the $\gamma - Re_\theta$ turbulence model to the local turbulence quantities is extensively discussed in literature, for instance by Bhattacharyya et al. (2015, 2016), Yao and Zhang (2018), Baltazar et al. (2018), Lopes et al. (2021) and Gaggero (2022). Turbulence quantities can be described using Turbulent Kinetic Energy (TKE) and Specific Dissipation Rate (SDR), or alternatively, Turbulence Intensity (TI) and Turbulent Viscosity Ratio (TVR), which can be again interpreted as TKE and SDR. TI is a representation of the root mean square of the local velocity fluctuations relative to the mean velocity. The ratio between the turbulent viscosity and the molecular viscosity is indicated by TVR. It influences the decay of the inflow turbulence from the inlet of the computational domain (upstream) and consequently its local value at the leading edge of the propeller. The decay can be intensified in the simulations due to the numerical diffusion, Lopes (2021) and Lopes et al. (2022).

In the current simulation setups incorporating the transition model, TKE and SDR sources are introduced in order to maintain the inflow turbulence from the inlet up to a distance $(0.6D)$ in front of the propeller center. The same distance is considered in Bhattacharyya et al. (2015), while only a TKE source is implemented in their study, disregarding the possible effects of TKE on the SDR and hence TVR. In the current study, to avoid the generation of disturbances on the free surface, the sources are applied from $0.5D$ under the free surface (the mean water level in calm water or regular head waves) downwards, while extended over the full width of the domain. Such dimensions are shown in Fig. 3. Optimization of the region in which the sources are active is out of the scope of the current investigations. These sources are added as source terms in the TKE and SDR transport equations. The source terms are applied in a way to maintain the intended turbulence intensity $\mathrm{TI}_{intended}$ and turbulent viscosity ratio $\mathrm{TVR}_{intended}$ from the existing values, i.e., $\mathrm{TI}_{existing}$ and $\mathrm{TVR}_{existing}$, in each computational cell within the activation region at each time step Δt as,

$$\mathrm{TKE}_{source} = \frac{\rho}{\Delta t} \times \frac{3}{2} U^2 \times (\mathrm{TI}^2_{intended} - \mathrm{TI}^2_{existing}),$$

$$\mathrm{SDR}_{source} = \frac{\rho}{\Delta t} \times \frac{\mathrm{TKE}_{existing}}{\nu} \times \left(\frac{1}{\mathrm{TVR}_{intended}} - \frac{1}{\mathrm{TVR}_{existing}}\right). \quad (5)$$

Although there might be a decay in the turbulence quantities from the edge of the active source region to the propeller geometry, the scope of such decay is expected to be relatively less significant than the simulation with no source considerations. Moreover, there are no measurements available for the turbulence quantities in the tank and the only possible way to judge the performance of the employed turbulence model incorporating the sources is through the comparison of its results with the experimental thrust and torque measurements. To this end, five different combinations of $\mathrm{TI}_{intended}$ and $\mathrm{TVR}_{intended}$ are considered in one operational condition ($J = 0.55$) in calm water. The combination with the lowest discrepancies with respect to the EFD data is adopted for performing the remaining simulations with transition model in all other operational conditions in calm water and regular head waves.

4.2. Grid generation

The computational domain is discretized employing a Sliding Mesh technique with in-place internal interface, consisting of a stationary fluid region and a rotating mesh region for the rotation of the propeller, considering particular treatment of cell sizes near the sliding mesh

interface (where the information is exchanged between the stationary fluid and rotating mesh regions). The STAR-CCM+ automatic mesh generator is used for the grid generation. Unstructured grids including the polyhedral meshes with local refinements near the propeller as well as prism layer meshes along the propeller surface and sliding mesh interface are used within the rotating mesh region. Unstructured grids including the trimmed hexahedral meshes with local refinements near the free surface and the rotating mesh region as well as prism layer meshes along the sliding mesh interface, shaft and hub cap surfaces are generated in the stationary fluid region.

For a higher computational efficiency, the height of the local refinement zone near the free surface in the calm water simulations is commonly opted to be narrower than the regular head wave simulations. Nonetheless, to minimize inconsistencies between these simulations, an identical grid is used for both calm water and regular head wave simulations in this study. Sigmund (2019) and Irannezhad et al. (2023) also considered the same grid for studying a bare hull performance in calm water and waves.

The primary focus of the performed uncertainty analysis in this paper lies in conducting a systematic grid convergence study. As outlined by Eça et al. (2016), for a valid grid convergence study, it is essential to generate progressively refined grids that exhibit precise "geometric similarity". Nevertheless, as it is also mentioned by Eça and Hoekstra (2014), it is extremely cumbersome, if not impossible, to generate geometrically similar unstructured grids. Consequently, we have considered various cautions to generate a set of "as geometrically similar as possible" unstructured grids in this study through diminishing the undesired grid refinements between two local refinement zones.

Four grids, systematically refined at different levels ($n = 0.75$ being the coarsest, followed by 1.00, 1.25, and 1.50 as the finest), are generated. The introduction of an extra coarser grid with $n = 0.50$ led to a notable decline in numerical wave quality, which is also discussed in Irannezhad et al. (2021). Thus, this grid is incapable of accurately capturing the main flow features, and its results may deviate significantly from those of the other grids. Consequently, no further analysis is conducted using this grid.

For isotropic volume meshes (Trimmed hexahedral meshes) in the stationary fluid region, every two adjacent cells with the same size in the grid $n = 1.00$ are refined into $2n$ cells in X, Y and Z directions, thus these two cells are replaced by $2n^3$ cells. Therefore, the local refinement zones dimensions as well as the refinement ratios between different zones are chosen cautiously to lay an integer number of cells in each direction and ensure that local refinements take place precisely within the specified local refinement zones, thus generating geometrically similar isotropic volume meshes. However, the undesired transition zones occurred while generating the grids with refinement levels of $n = 0.75$ and 1.25. Consequently, these grids exhibit marginal geometric differences from the others when the isotropic volume meshes are compared.

The approach outlined by Crepier (2017) is followed to attain geometrically similar prism layer meshes (anisotropic sub-layer), in which the total thickness of prism layers is maintained consistently across the grids but the adjustments are made to both the first layer cell thickness δ and the growth ratio between the layers γ based on,

$$\delta_n = \delta_1 \frac{1-\gamma_1^{\frac{1}{n}}}{1-\gamma_1}, \qquad \gamma_n = \gamma_1^{\frac{1}{n}}. \tag{6}$$

δ_1 and γ_1 are the first layer cell thickness and the growth ratio for the grid $n = 1.00$. Consequently, $N_n = nN_1$ is the total number of layers in each grid with refinement level n, where N_1 is the total number of layers for grid $n = 1.00$. Therefore, N_1 is chosen in a way to yield an integer number of layers via multiplication nN_1. Fig. 2 illustrates an overview of the grids for two refinement levels $n = 0.75$ and $n = 1.00$. It is worth mentioning that the prism layers in both regions near the sliding mesh interface are generated in order to make local refinements (smaller cells) and thus more accurate information exchange at the interface.

For the treatment of the near-wall region, a wall-resolved approach is employed. Therefore, the considered first layer thickness of the prism mesh in all grids results in the non-dimensional wall distance $y^+ < 1$ over the major part of the propeller surface area.

Despite the aforementioned efforts to generate a geometrically similar set of grids, there are inevitable differences between the generated unstructured grids, particularly between the polyhedral meshes as well as the zone between the last prism layers and their adjacent isotropic cells. Furthermore, the finer grids capture the geometry more accurately leading to geometrical differences between the prism layers for different grids. Therefore, the grids are "as geometrically similar as possible". Consequently, the total number of cells are 8 430 349, 16 418 462, 28 634 860 and 45 185 807 for $n = 0.75$, 1.00, 1.25 and 1.50, respectively, where more than half of the cells are within the rotating mesh region. The calm water simulations as well as the simulations in regular head waves of $\lambda/L = 0.570$, $H = 0.070$ m (WC2), only for the advance ratio of $J = 0.55$, are carried out in all four refinement levels (including a grid convergence study), while the rest of simulations are only carried out using the grid $n = 1.00$.

Based on the local refinement zone near the free surface, the cell size in the vertical Z direction is $(0.006\text{ m})/n$ in each grid refinement level n. Therefore, $H/(0.006/n)$ cells are considered per wave height H in each grid. For instance, in grid $n = 1.00$, roughly 7, 12, 20 and 22 cells are considered per wave height for $H = 0.042$ m, 0.070 m, 0.120 m and 0.133 m, respectively. The cell aspect ratio equal to 4 is considered in the longitudinal X and transversal Y directions in relation to the vertical Z direction. Therefore, the cell size in the X direction is $(0.024\text{ m})/n$. Consequently, there are $n\lambda/0.024$ cells per wave length for each wave in each grid. For instance, in grid $n = 1.00$, roughly 166 and 314 cells are considered per wave length for $\lambda = 3.990$ m and 7.546 m, respectively.

4.3. Computational domain

Fig. 3 depicts an overview of the dimensions of the computational domain (for the simulations with $3R$ submergence depth) and the considered boundary conditions. To minimize the wave reflection from the boundaries, a wave forcing function is utilized in the vicinity (distance equal to $14.8D$) of two boundaries as shown in Fig. 3. The wave forcing function forces the solution of the discretized Navier–Stokes equations, for simulations in regular head waves, towards the solution of the theoretical 5th order Stokes wave, and for calm water simulations, towards the solution of the still water.

The free surface elevation in the simulations is monitored at a wave probe located at a distance in front of the propeller. The actual incident wave at the position of the propeller may be different from the monitored wave due to the numerical wave propagation issues. However, since the free surface can be influenced by the propeller suction, the only feasible approach to evaluate the incident wave is through the monitored wave at the probe. We expect insignificant deviations between the actual incident wave and the analytical wave as the simulation setup in the current study complied with the wave propagation configurations derived by Irannezhad et al. (2021).

It is also worth mentioning that a simulation in a regular head wave condition is carried out using much wider domain in Y direction in order to examine any possible effects from the side boundaries. However, the results remained almost identical, hence the current domain width is found to be large enough for all of the POW simulations.

4.4. Time step

An implicit unsteady solver is utilized with a second-order temporal discretizational scheme. The time step is chosen in order to have 1° of propeller rotation per time step in grid $n = 1.00$, hence time step in each grid refinement level n is determined as $\Delta t = 1/(360 n_P n)$. The selected time step leads to a similar Courant number between the grids with the

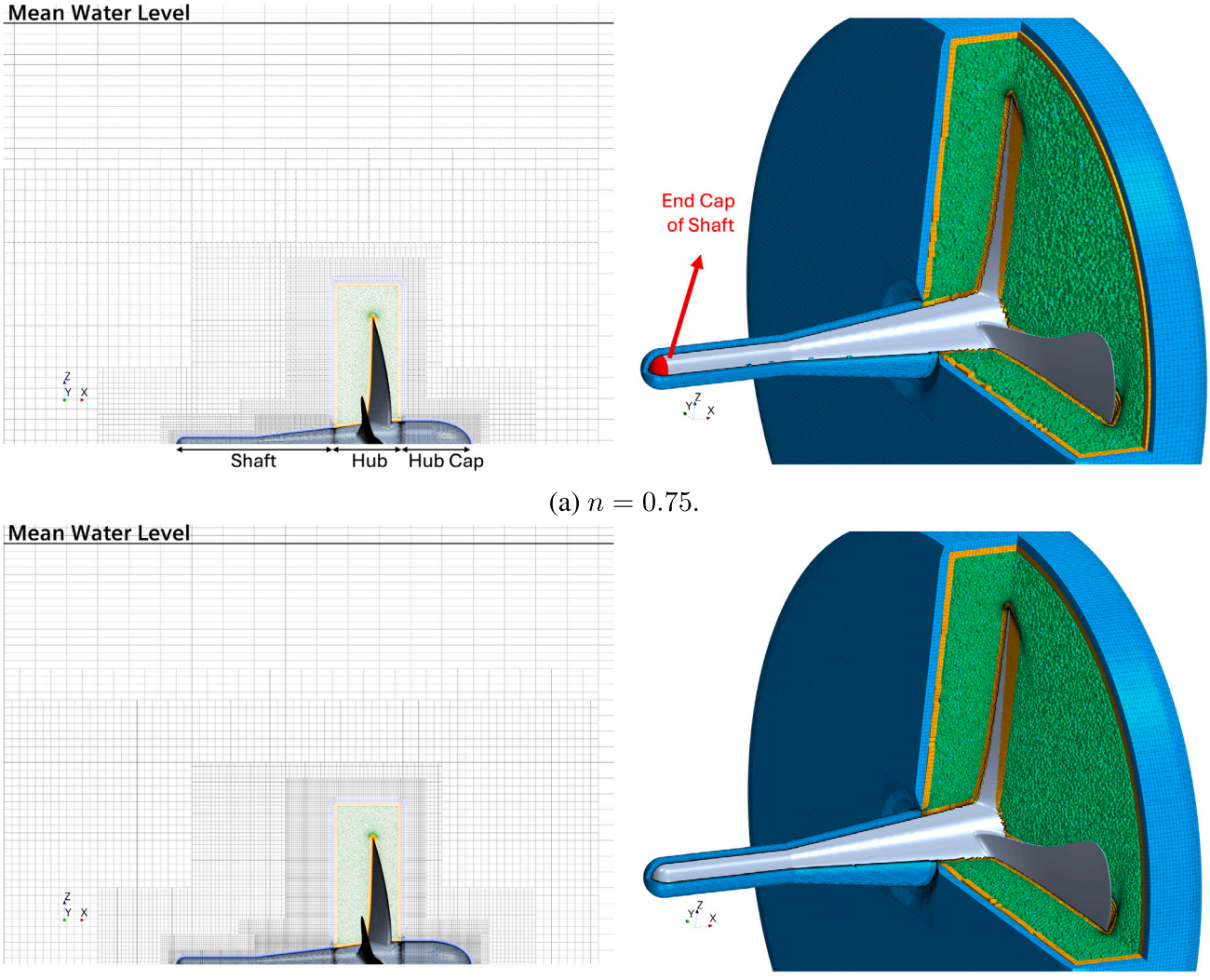

Fig. 2. Overview of the grids near the propeller. Gray lines represent the trimmed hexahedral mesh in the stationary fluid region. Blue and orange colors represent the prism layer meshes in the stationary fluid and rotating mesh regions, respectively. The green color represents the polyhedral mesh in the rotating mesh region.

same propeller rotational speed n_P. Furthermore, the Courant numbers on the free surface remain very small, hence fulfilling the ITTC (2014) recommendations and numerical wave propagation best practices. The maximum number of inner iterations per time step is set to 20.

A complete uncertainty analysis should include both iterative and grid convergence studies, while the uncertainty analysis in the current study only considers the grid convergence study. Therefore, to perform a valid uncertainty analysis, the time step size and maximum number of inner iterations per time step are chosen conservatively, hence diminishing the dependency of the results on the time step. To evaluate such dependencies, a selective set of simulations is carried out with considerably smaller time steps, nevertheless, the results remained almost unchanged.

4.5. Uncertainty analysis method

For the grid convergence study in the current paper, the numerical uncertainty analysis tool developed by Eça et al. (2019) is utilized. In the first step, the discretization error is assessed using power series expansions as a function of the typical cell size h_i which is determined based on,

$$h_i/h_1 = \sqrt[3]{N_{cell\,1}/N_{cell\,i}}, \tag{7}$$

where $N_{cell\,i}$ is the number of cells for the grid i. There should be at least four grids and $i = 1$ is the finest grid. Four types of expansions are assessed through,

$$\begin{aligned} \Phi_i - \Phi_0 &= \alpha {h_i}^p, \\ \Phi_i - \Phi_0 &= \alpha h_i, \\ \Phi_i - \Phi_0 &= \alpha {h_i}^2, \\ \Phi_i - \Phi_0 &= \alpha_1 h_i + \alpha_2 {h_i}^2, \end{aligned} \tag{8}$$

where Φ is the quantity under study, Φ_i is the solution for grid i, Φ_0 is the estimated exact solution, p is the observed order of grid convergence and α is a constant coefficient. Thereafter, the best fit to the data for each expansion is achieved in the least-squares sense considering different formulations (weighted and non-weighted fits of expressions). The choice of the optimal error estimate relies on the standard deviation of the fits. Subsequently, this error estimate is

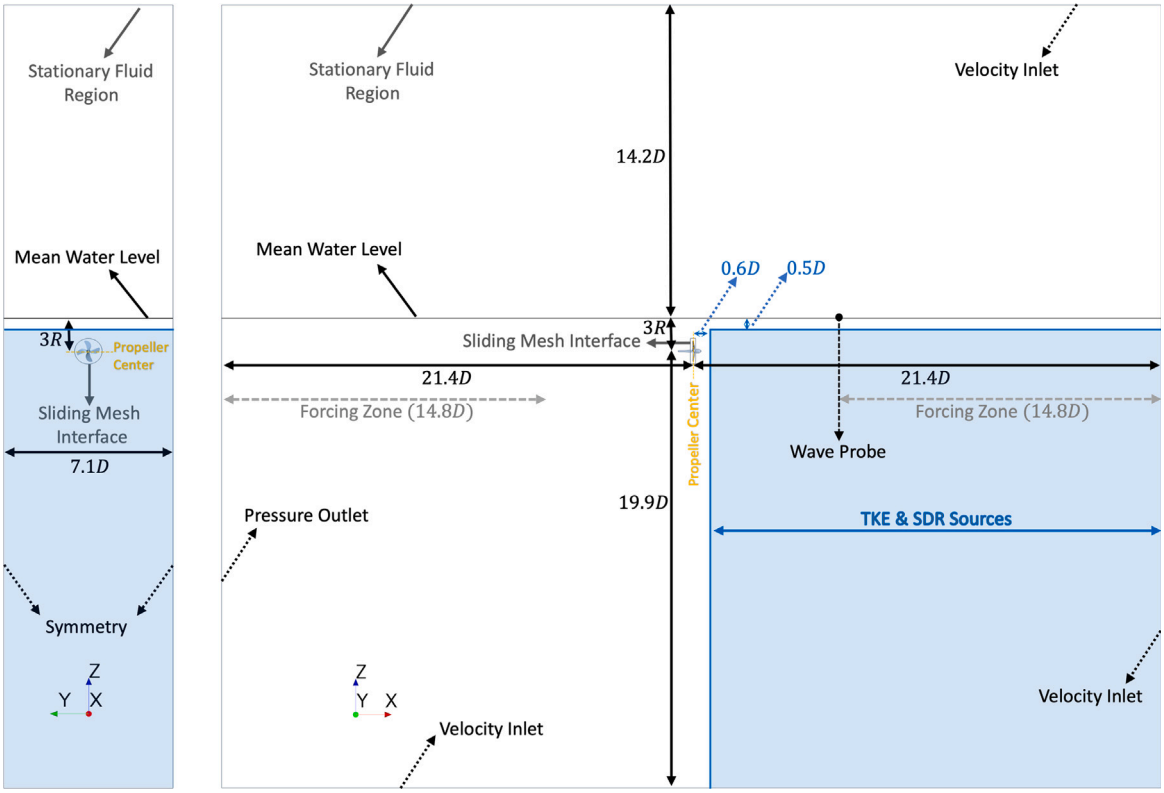

Fig. 3. Computational domain size, applied boundary conditions and active TKE and SDR sources region.

transformed into an uncertainty with a safety factor depending on both the observed order of grid convergence and the standard deviation of the fit. Further details regarding the tool and the involved methodology can be found in Eça and Hoekstra (2014).

4.6. Convergence criteria and post-processing techniques

Prior to post-processing of the simulations results, the convergence of the simulations should be evaluated in each time step as well as statistically for a trustworthy time period. Based on the ITTC (2014) recommendations, the convergence can be assessed through the variations observed in the mass and momentum equations residuals (indicating the deviations of the current estimated solution from the ideal mass and momentum conservation).

In the current simulations, the convergence in each time step is expected to be fulfilled due to the conservative choice of the number of maximum internal iterations (20 iterations) per time step. While ITTC (2014) recommends a convergence criterion based on the drop of normalized residuals by several orders of magnitude of their initial values, the residuals for the POW simulations show an oscillatory behavior during the solution time due to the complexity of the problem, thus this criterion may not be fulfilled. Furthermore, residuals may not be directly associated with quantities of engineering interest in the simulation, e.g., hydrodynamic forces. Consequently, in addition to the residual monitoring in this paper, the convergence is primarily assessed through the computed thrust and torque.

The same rotational speed as the rotating mesh region is applied to the shaft and hub cap in the stationary fluid region (shown in Fig. 2(a)), by specifying the wall tangential velocity boundary condition on these surfaces. Consequently, the whole geometry in the simulations rotates as in the towing tank experiment. The thrust and torque are obtained over the whole geometry surfaces, i.e., blades, hub, hub cap and shaft, except for the end cap of the shaft (see Fig. 2(a)) as this semi-sphere was not present in the experiments. The pressure force is significant on this end cap and its inclusion results in a departure from the forces measured in the experiments. Although the shaft in experiments was much longer (with a smaller part exposed to water and the rest in the shaft line casing as depicted in Fig. 1), the shaft length in the simulations is considered to be long enough to have negligible effect on the upstream flow and hence the propeller performance. It should be noted that a longer shaft would increase the number of cells in the simulations, hence increasing the computational costs.

The thrust and torque coefficients, i.e., K_T and K_Q, are defined as,

$$K_T = \frac{T}{\rho n_P^2 D^4}, \qquad K_Q = \frac{Q}{\rho n_P^2 D^5}, \tag{9}$$

in which T and Q are the propeller thrust and torque, respectively. The propeller open water efficiency η_O is then calculated as,

$$\eta_O = \frac{J K_T}{2\pi K_Q}. \tag{10}$$

It is worth mentioning that the mean value of the propeller efficiency in regular head waves is computed from the instantaneous propeller efficiency employing the instantaneous thrust and torque coefficients and not the mean values of these coefficients.

4.6.1. Convergence criterion for calm water simulations

The ideal convergence in calm water simulations requires obtaining infinitesimal oscillations in the thrust and torque signals and hence a single value for each quantity. Because of the unsteady nature of the problem, achieving ideal convergence is computationally extremely expensive and beyond a specific threshold, it might not lead to noteworthy alterations in the magnitude of the eventual value. In order to minimize the computational costs and attain reliable predictions from

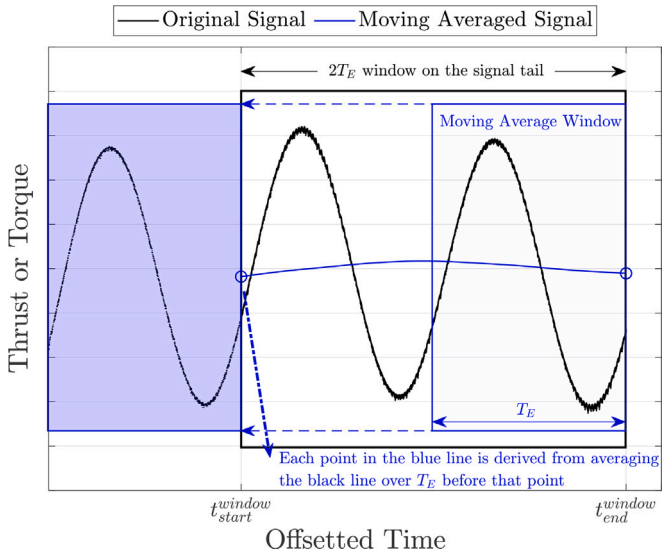

Fig. 4. A representative thrust/torque signal together with its periodic moving average for explaining the convergence criteria and post-processing techniques in regular head waves.

the simulations results, a convergence criterion on the thrust and torque signals is established.

A calm water simulation is deemed converged when the Standard Deviation (STD) of the thrust and torque time histories is below 1% of its Root Mean Square (RMS) for a certain time window of the signal tail. In all calm water simulations, a 1 s long time window is chosen. If STD%RMS < 1 for both thrust and torque, then the simulation is deemed converged and the calm water thrust and torque are computed by averaging the respective signals over the time window (the last 1 s of the signal tail).

4.6.2. Convergence criterion for regular wave simulations

The ideal convergence in regular head waves can be obtained if the thrust and torque signals become periodic (harmonic) with respect to the wave encounter frequency with consistent harmonic amplitudes. Because of the unsteady nature of the problem, achieving ideal convergence is almost impossible in regular head waves. Similar to calm water, a convergence criterion on the thrust and torque signals is established in regular head wave simulations to derive trustworthy predictions for these quantities.

While the hydrodynamic analysis of the signals is performed for the original time series, the convergence criterion in regular head waves is defined on the "periodic moving average" of the thrust and torque time series. The periodic moving average is extracted from the original time series, where its value at each time instance is the average of the original signal values over a moving average window prior to that certain instance of time. In Fig. 4 a representative plot is illustrated for a thrust/torque signal sample alongside its periodic moving average in regular head waves simulations.

The horizontal axis displays the offset time, focusing solely on the tail of the computed signal while excluding the initial segment. The black line is the original thrust or torque signal. A moving average window (blue rectangle) is chosen to extract the periodic moving average signal (blue line). Selecting a time interval equal to an integer multiple of the encounter wave period T_E would be a suitable choice for the moving average window. Based on the preliminary studies and to keep the computational costs low, here, the moving average window is defined as $1 \times T_E$ for each respective wave length.

Then, a time window is extracted from the original signal tail and marked with a black rectangle. The original signal consists of a dashed line part starting at an arbitrary instance of time and a solid line part starting from the kick-off time of the extracted time window and extending to the end of the original signal.

It is assumed that the convergence in regular head waves is achieved when the Standard Deviation (STD) of the periodic moving averaged signal (blue line) for the chosen moving average window (blue rectangle) is lower than 1% of its Root Mean Square (RMS) over a chosen time window (black rectangle). If the STD%RMS < 1, then the simulation is deemed converged, and the original signal is post-processed over the chosen time window. In the current study, the time window in each wave length is chosen to be $2 \times T_E$ and the Fourier analysis is performed (for each quantity being investigated $\psi(t)$) as,

$$\psi(t) = \psi_0 + \psi_1 \cos(\omega_E t + \psi_{\varepsilon 1}) + \psi_2 \cos(2\omega_E t + \psi_{\varepsilon 2}) + \psi_3 \cos(3\omega_E t + \psi_{\varepsilon 3}) + \cdots, \tag{11}$$

in which ψ_i is the ith harmonic amplitude, and $\psi_{\varepsilon i}$ is the ith harmonic phase component. The choice of $2 \times T_E$ time window is made to minimize the spectral leakage in the Fast Fourier Transform (FFT) results.

4.6.3. Reconstruction of time series

In order to analyze the instantaneous values of different quantities and their correlations during the wave encounter, the reconstructed time series can be used. The reconstruction is carried out to derive reconstructed time series for 1 encountered wave period T_E in each wave length. The dominant harmonic components (HC), i.e., harmonic amplitudes (HA) and harmonic phases, from the FFT results from Eq. (11) over the chosen time window are employed for the reconstruction of the time series. The origin of time $t/T_E = 0$ in the reconstructed time series is defined as the zero up-crossing of the analytical wave elevation at the propeller center, to ensure compatibility for both EFD and CFD among all the reconstructed time series.

The wave elevation time series are reconstructed considering up to (and including) the 5th harmonic components, as the 5th order Stokes waves are employed in the simulations. Nevertheless, the propeller thrust, torque and efficiency are reconstructed considering up to (and including) the 3rd harmonic components since the higher harmonic amplitudes are negligible.

In Fig. 5, a representative plot for torque in an operational condition in regular head waves is shown consisting the original EFD measurement signal, the reconstructed EFD signal considering the dominant (up to the 3rd) harmonic amplitudes at the wave encounter frequency, the CFD results for the full propeller geometry and the CFD results of a single blade multiplied by 4 (total number of blades). One of the main differences between CFD and EFD time series lies in the presence of the oscillations at the propeller rotation frequency (i.e., matching the propeller rotational speed n_P) in the original EFD time series which are almost negligible and extremely small in the full propeller CFD time series (the comparison between the black and blue solid lines in Fig. 5). Nevertheless, the one-blade CFD results exhibit oscillations at the propeller rotation frequency due to the varying incident inflow at different blade positions, but such oscillations in the full propeller CFD time series are smoothed out. Therefore, in CFD results, the loading variation on the blades is almost canceled out when the full geometry is taken into account. We speculate that shaft line vibration due to the asymmetry nature of the flow into the propeller (e.g., from the wave orbital velocities and slight shaft inclination) in the towing tank POW tests is the main reason for the sustained oscillations in the original EFD results. Nevertheless, the reconstruction is performed considering solely the harmonic amplitudes at the wave encounter frequency (similar to a low-pass filter application), hence the oscillations at the propeller rotation frequency are eliminated in the performed analyses in this paper.

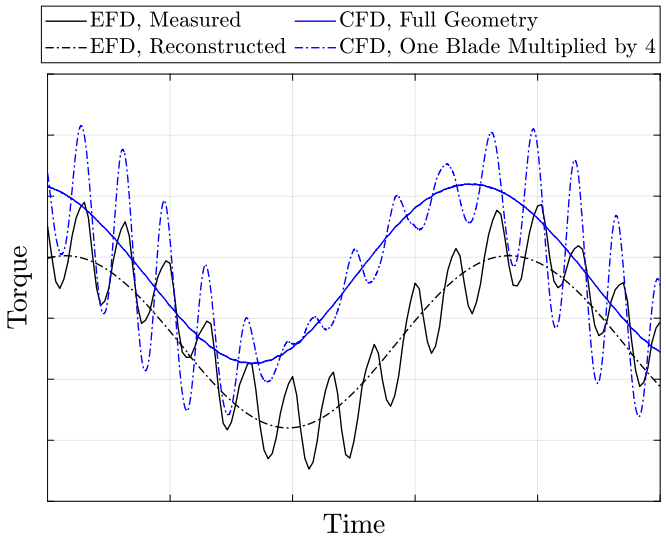

Fig. 5. Representative EFD and CFD signals for explaining the oscillations in the propeller rotation frequency.

4.6.4. Incident flow field

In this section, the incident flow field analysis techniques are provided in order to lay a foundation for the discussions regarding the dynamic load distribution and variations. To this end, a schematic representation of the incident flow field for a generic blade section at radius r (disregarding the propeller induced velocities) is shown in Fig. 6. There are two coordinate systems defined at the propeller center: a Cartesian coordinate system with X-axis (longitudinal axis) pointing in the propeller advance direction and Z-axis (vertical axis) pointing upwards, and a Cylindrical coordinate system with radial coordinate r pointing away from the propeller rotation axis and azimuthal coordinate θ with its reference, $\theta = 0°$, shown in Fig. 6(b). The azimuthal positions of $\theta = 90°$, $180°$ and $270°$ are also illustrated in this figure. The propeller rotational angular velocity Ω is in the decreasing θ direction. The axial coordinate of the Cylindrical coordinate system is aligned with the longitudinal axis of the Cartesian coordinate system, but pointing in the opposite direction.

In Fig. 6(a), the "Geometric Pitch Angle" $\Theta(r)$ is defined as the angle between the blade section chord line and the azimuthal direction. The blade section lift and drag, and hence thrust and torque forces, are shown at the trailing edge of the blade section. The in-plane axial and rotational velocities faced at the leading edge of the blade section (neglecting the propeller induced velocities) are shown in Fig. 6(a). The axial velocity at the position (r,θ), i.e., $u_{axial}(r,\theta)$, can be calculated from the modification of the advance velocity of the propeller U by the axial velocity component of the wave orbital velocities $u^{wave}_{axial}(r,\theta)$ at that position. Moreover, the rotational velocity at position (r,θ), i.e., $u_{rotational}(r,\theta)$, is calculated from the blade section rotational speed $\Omega r = 2\pi n_P r$ and the projection of the vertical velocity component of the wave orbital velocities, $u^{wave}_{vertical}(r,\theta)\sin(\theta) = u_\theta(r,\theta)$, on the blade section rotational speed direction.

The angle between the resultant in-plane incident velocity $\sqrt{u^2_{axial}(r,\theta) + u^2_{rotational}(r,\theta)}$ and the chord line is called "Incidence Angle" $\alpha(r,\theta)$. Accordingly, the "Geometric Advance Angle" $\beta(r,\theta)$ is defined as,

$$\beta(r,\theta) = \Theta(r) - \alpha(r,\theta) = \Theta(r) - \text{atan}\left(\frac{u_{axial}(r,\theta)}{2\pi n_P r + u_\theta(r,\theta)}\right). \quad (12)$$

The analysis of the geometric advance angle could help understanding the dynamics of blade loading during the propeller performance in regular head waves. As mentioned before, the idea is to eliminate the propeller induced velocities when studying the geometric advance angle. Therefore, the geometric advance angle is derived on a "representative propeller disk" identical to the propeller disk (excluding the hub) and located at a distance $(2.4D)$ in front of the propeller center, which found to be negligibly affected by the induced velocities in this study. Then, the time is offset in order to introduce an identical condition between the representative propeller disk and the propeller geometry with respect to the analytical wave elevation above the propeller. In Fig. 7, the geometric pitch angle $\Theta(r)$ on the representative propeller disk is shown which is purely dependent on the propeller geometry, i.e., the blade pitch distribution in the radial direction.

The vertical component of the wave orbital velocity has another component in the radial direction defined as, $u_r(r,\theta) = u^{wave}_{vertical}(r,\theta)\cos(\theta)$. This velocity component results in an out-of-plane velocity component with respect to the circumferential sections. The intriguing three-dimensional effects of this component have not been considered in the analysis of the flow over the blades.

5. Calm water - V & V

In this section, the calm water results are provided including a verification and validation analysis of the propeller characteristics. Solely the propeller with the submergence depth of $3R$ is considered in the calm water investigations. The convergence criterion, explained in Section 4.6.1, is fulfilled in all of the calm water simulations in which STD%RMS remains lower than 0.5 for both thrust and torque.

5.1. Experimental results

The model tests in calm water are carried out for a series of advance ratios $J = U/(n_P D)$. The desired advance ratios are obtained in two ways: either by keeping the carriage speed constant U_{cte} and adjusting the propeller rotational speed n_P or by keeping the propeller rotational speed constant $n_{P_{cte}}$ and adjusting the carriage speed U. The EFD results for the propeller characteristics considering $U_{cte} = 1.177$ m/s or $n_{P_{cte}} = 21.9$ rps are shown in Fig. 8, which also includes a data set of previous measurements for the same propeller from SSPA database with constant propeller rotational speed $n_{P_{cte}}$.

The flow over each propeller blade can be a combination of laminar, transitional and turbulent flow, Baltazar et al. (2021). The propeller Reynolds number based on the chord length at $0.7R$ defined as $Re = C_{0.7R}\sqrt{U^2 + (0.7\pi D n_P)^2}/\nu$ is commonly used in order to assess the flow regime in POW performance studies. Although the Reynolds number in full-scale propellers often leads to a fully turbulent flow regime, the Reynolds number in model-scale propellers may approach the laminar flow range. It is important to note that for an identical advance ratio $J = U/n_P D$ of a propeller, both the advance velocity U and propeller rotational speed n_P can be increased/decreased, i.e., both scaled by the same factor, resulting in a higher/lower propeller Reynolds number. Therefore, the way the propeller is operated may directly affect the Reynolds number for the same advance coefficient.

In this study, due to the small size of the tested propeller diameter and its operating conditions, the Reynolds number will approach the laminar flow range, resulting in the occurrence of laminar flow on the blades. The amount of laminar flow becomes more significant for the performed model tests with constant carriage speed U_{cte}, because of the smaller Reynolds numbers in these tests. For instance, the propeller Reynolds number in U_{cte} condition at $J = 0.35$ and 0.60 is approximately 3.38×10^5 and 2.03×10^5, respectively. On the other hand, the propeller Reynolds number in $n_{P_{cte}}$ condition at $J = 0.35$ and 0.60 is almost 4.78×10^5 and 4.88×10^5, respectively.

According to the ITTC (2021a) recommendations, in order to obtain a reliable open water model test data for full-scale power prediction, the propeller Reynolds number should be larger than $2 \times 10^5 - 5 \times 10^5$, depending on the propeller type. However, the aim of the current study is to evaluate the POW performance in calm water and regular head waves for the propeller under a similar operational condition as the

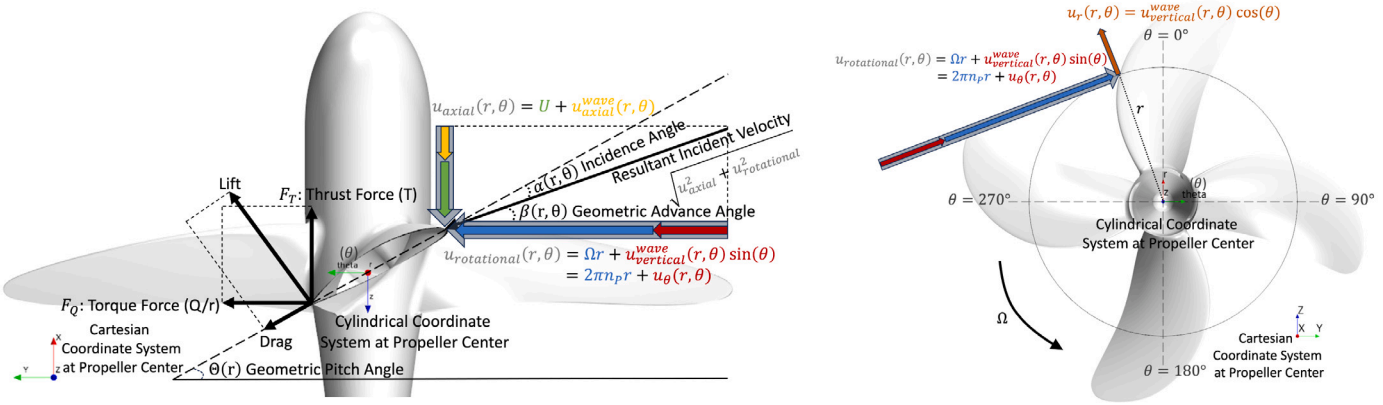

(a) Top view. (b) Front View.

Fig. 6. Schematic representation of the incident flow for a generic blade section at radius r disregarding the propeller induced velocities.

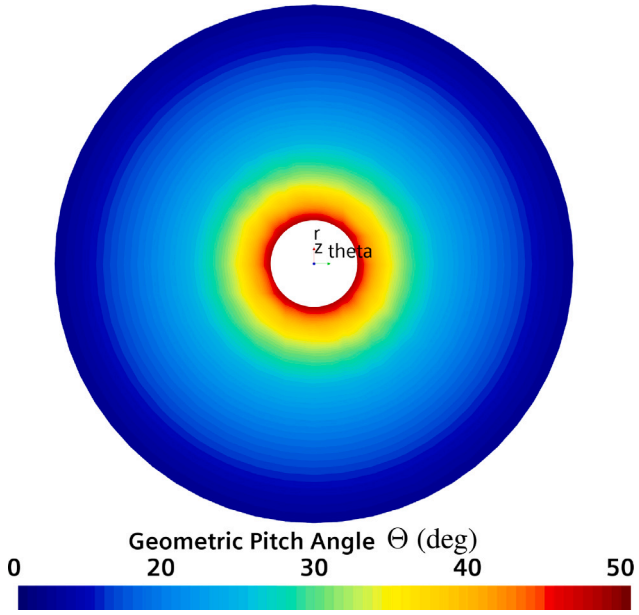

Fig. 7. Geometric pitch angle distribution on a representative propeller disk.

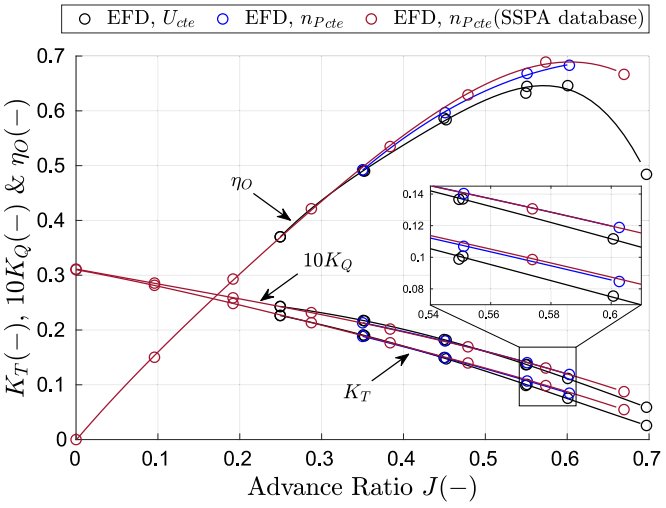

Fig. 8. Open water curves from the calm water towing tank tests.

propeller experiences behind the self-propelled KVLCC2 at its design speed, but disregarding the hull interactions. Therefore, it is decided to perform all the POW tests and CFD simulations in regular head waves for the propeller with an advance velocity (carriage speed) matching the corresponding KVLCC2 design speed at the same geometrical scale ratio as the propeller. Different advance ratios are then achieved through the variation of the propeller rotational speed. The dominance of the laminar flow regime may then become crucially important in the current investigations.

As seen in Fig. 8, the flow regime has significant effects on the propeller performance. For instance, at $J \approx 0.60$, the thrust and torque coefficients, i.e., K_T and K_Q, increase approximately 12.2% and 6.5%, respectively, from the constant carriage speed condition U_{cte} to the constant propeller rotational speed condition $n_{P_{cte}}$. Consequently, K_T/K_Q and hence propeller open water efficiency η_O are increased approximately 5.4%. Given that the experimental and numerical investigations in regular head waves in the current paper cover only the constant carriage speed condition U_{cte}, the subsequent POW performance analyses in calm water and regular head waves will solely focus on this condition and a constant speed of $U = 1.177$ m/s. Henceforth, this speed which corresponds to the design Froude number for the model-scale KVLCC2 ($L = 7$ m) is adopted for all the presented EFD and CFD results.

5.2. Transition modeling

As mentioned in Section 4.1, the $\gamma - Re_\theta$ transition model is employed in particular simulations in order to account for the effects of flow regime on the propeller performance. Moreover, due to the decay of the upstream turbulence in the computational domain, the Turbulent Kinetic Energy (TKE) and Specific Dissipation Rate (SDR) sources are applied in the region shown in Fig. 3. The aim is to minimize the turbulence decay and maintain the Turbulence Intensity (TI) and Turbulent Viscosity Ratio (TVR), defined at the inlet, throughout the domain until the flow reaches the propeller.

Due to the lack of information about the turbulence quantities in the towing tank at the time of model tests, five arbitrary turbulence source conditions are investigated in the calm water simulations with the transition model. The investigated conditions represent various combinations of TI and TVR. These simulations are all carried out for the grid $n = 1.00$ at advance ratio $J \approx 0.55$, which almost corresponds to the maximum propeller efficiency. The results are shown in Fig. 9 which also includes the fully turbulent simulation results (without the transition model). The vertical axis is segmented into different intervals in order to accommodate all results in a single plot without sacrificing key features, despite significant differences in magnitude. Although the

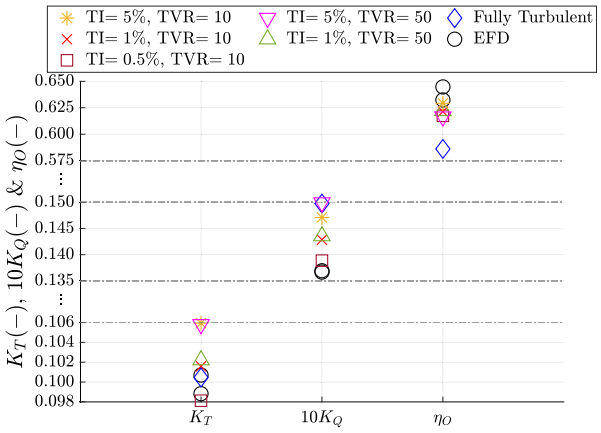

Fig. 9. Effects of turbulence source condition (TI and TVR) on the propeller performance in the calm water simulations incorporating the $\gamma - Re_\theta$ transition model with grid $n = 1.00$ at $J \approx 0.55$. The fully turbulent simulation results as well as the EFD results are also shown.

TI in which the propeller operates may also affect the fully turbulent simulation results, the significance of such effects is much lower in comparison to the simulations considering transition model, Baltazar et al. (2021). Here, the turbulent intensity of the flow approaching the propeller is around 0.2% in the fully turbulent simulation.

There is no straightforward way to compare the results of these five turbulence source conditions from the physical perspective, especially when there are no paint tests available as in the current investigations. Moreover, the full performance analysis of the employed transition model with the source considerations is out of the scope of the current investigations. Therefore, the choice of the best turbulence source condition is made through the comparison of the propeller characteristics with the respective experimental results. There are two experimental measurements in Fig. 9 with similar K_Q but different K_T and η_O, as it was also seen in Fig. 8, which may reflect the uncertainty of the experimental data in this advance ratio. While K_T is similar between the fully turbulent simulation result and EFD, K_Q and η_O vary significantly.

On the one hand, the comparison between each turbulence source condition and EFD in calm water should mainly concern K_T and K_Q because η_O is a consequence of thrust and torque. As a result, depending on the relative error of thrust and torque, their variations can lead to small or very large errors in the resultant efficiency. On the other hand, propeller thrust is correlated with its torque. Therefore, the propeller open water efficiency η_O can also be examined aiming at assessing the thrust and torque correlations.

The turbulence source conditions with higher turbulence intensity TI = 5% resulted in much higher thrust and torque in comparison to the EFD data. For the turbulence source conditions with TI = 1%, the thrust and toque predictions are improved especially for the case with lower TVR value. For the turbulence source condition with the lowest turbulence intensity TI = 0.5%, a significantly better torque prediction is observed. It is worth mentioning that a simulation with the fully laminar flow consideration is also carried out (not presented in Fig. 9). Although the torque prediction from this simulation ($10K_Q = 0.1354$) is very similar to the EFD data, the thrust is significantly under-predicted ($K_T = 0.0949$). Consequently, it is believed that although there was laminar flow dominance in the model tests, the transition to turbulent has occurred to some extent.

To conclude, the turbulence source condition with TI = 0.5% and TVR = 10 is found to be a better resemblance of the turbulence quantities in the towing tank, and hence it is considered for all the simulations with transition model henceforth. In spite of this conclusion, it is important to emphasis that certifying the turbulence characteristics of the flow preceding the propeller remains unfeasible. Furthermore, there is a possibility of additional, unaccounted-for combined effects that could contribute to the observed favorable correspondence between the calculated and measured propeller quantities using the above-mentioned TI and TVR. The fully turbulent simulations and the transition model simulations with the turbulence source condition of TI = 0.5% and TVR = 10 are hereafter tagged as "FT" and "TM", respectively.

Fig. 10 presents the effects of the adopted turbulence source condition (TI = 0.5% and TVR = 10) in the calm water simulation with the transition model (TM) by comparing different flow quantities with those of fully turbulent simulation (FT) in the last time step. A transitional flow is characterized by intermittent bursts of turbulence within an otherwise predominantly laminar flow. Turbulence intermittency represents the fraction of time during which the flow over a certain location in the flow is turbulent. Intermittency in Fig. 10(a) and velocity vectors in Fig. 10(b) are shown on three cylindrical cross sections at $r = 0.04$ m, 0.06 m and 0.08 m ($r/R \approx 0.37$, 0.56 and 0.74) in the vicinity of the propeller blade located at the azimuthal position $\theta \approx 30°$. The intermittency is only available in the simulations incorporating the transition model. The constrained streamlines (limiting streamlines) are also shown which are defined as the paths traced by imaginary particles following the direction of the local shear stress of the fluid at any given point and time. The velocity vectors represent the velocity in the rotating reference frame which is equal to the propeller rotational speed. However, the vectors are colored by the radial velocity u_r (including the propeller induced velocities) non-dimensionalized by the magnitude of the resultant velocity from the rotational speed of the propeller $r\Omega$ and the axial velocity u_a (including the propeller induced velocities).

The transition to turbulent flow in the suction side of the blade can be perceived by the value of intermittency on the sections shown in Fig. 10(a). The flow near the wall over the pressure side of the blade mainly remains laminar. The constrained streamlines in a laminar boundary layer (TM simulation) are radially directed due to the dominance of the centrifugal forces. The converging constrained streamlines on the suction side of the blade demonstrate that the laminar separation might play a significant role in the onset of transition. The velocity vectors for TM simulation in Fig. 10(b) also reveal the existence of cross-flow in the vicinity of the trailing edge across the blade, which is also shown by the constrained streamlines.

The velocity vectors and hence the constrained streamlines of the FT simulation exhibit notable differences relative to TM simulation, shown in Fig. 10(b). The limiting streamlines in a turbulent boundary layer (FT simulation) exhibit a greater circumferential orientation due to the existence of high shear forces. Although the constrained streamlines in the suction side represent separation in the FT simulation, the separation occurs much closer to the trailing edge of the blade with a significantly smaller extension over the blade area in comparison to TM simulation. The constrained streamlines near the tip of the blade are more aligned with the rotation direction of the propeller in FT simulation on both suction side and pressure side of the blade in comparison to TM simulation.

The variation of the wall shear stress magnitude over the blade, shown in Fig. 10(c), as well as the constrained streamlines, facilitate the flow regime assessment. The dominance of the laminar flow is evident through the smaller magnitudes of the wall shear stress approximately across the entire blade on both suction side and pressure side in TM simulation. Lower magnitudes of the wall shear stress for TM simulation may account for the lower torque reported in Fig. 9. Nonetheless, the wall shear stress magnitude is larger in the vicinity of the blade trailing edge on the suction side in TM simulation in comparison to FT simulation. However, the shear stress in this region is mainly aligned in the radial direction and thus will not contribute to propeller torque.

The distribution of the hydrodynamic pressure, shown in Fig. 10(d), is rather similar between the FT and TM simulations. The main differences are seen close to the trailing edge of the blades with higher

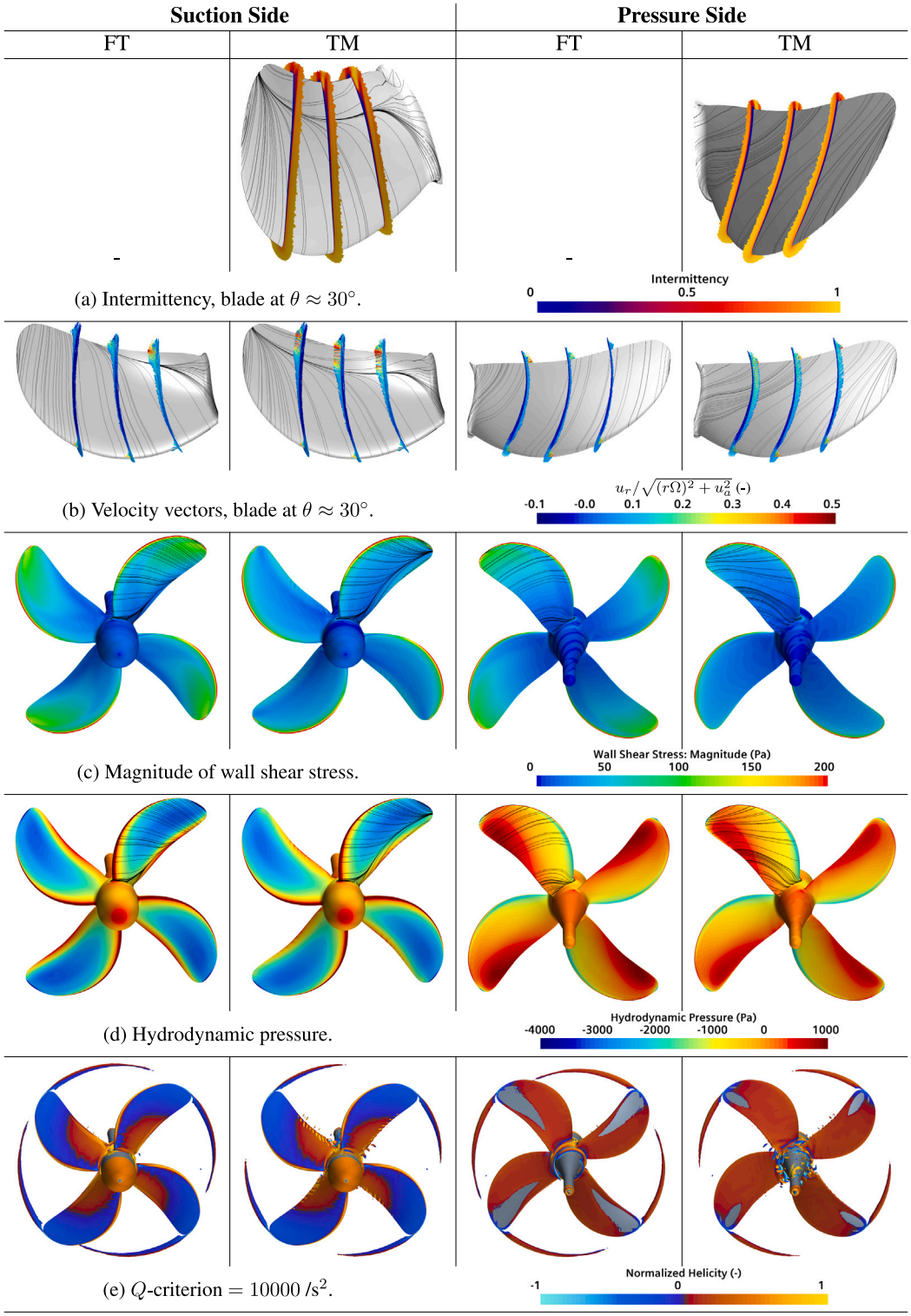

(a) Intermittency, blade at $\theta \approx 30°$.

(b) Velocity vectors, blade at $\theta \approx 30°$.

(c) Magnitude of wall shear stress.

(d) Hydrodynamic pressure.

(e) Q-criterion $= 10000\ /s^2$.

Fig. 10. Comparison between the FT and TM calm water simulations results (last time step), both with grid $n = 1.00$ at $J \approx 0.55$ over the suction and pressure sides of the propeller blade.

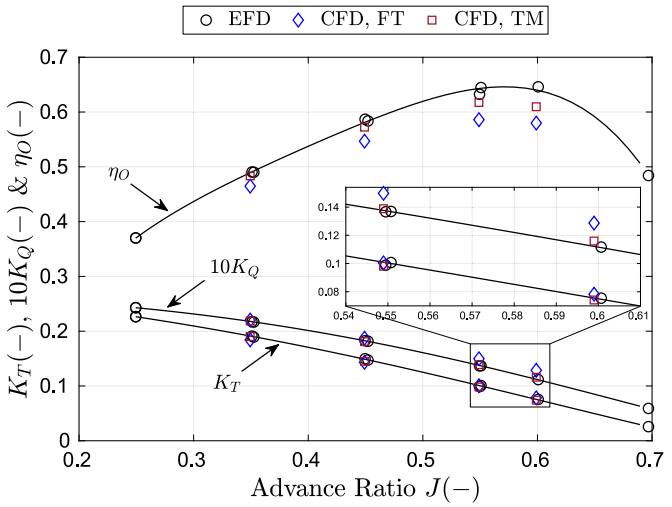

Fig. 11. Comparison between EFD and CFD results in both fully turbulent simulations and the simulations incorporating the transition model, all with grid $n = 1.00$ in calm water.

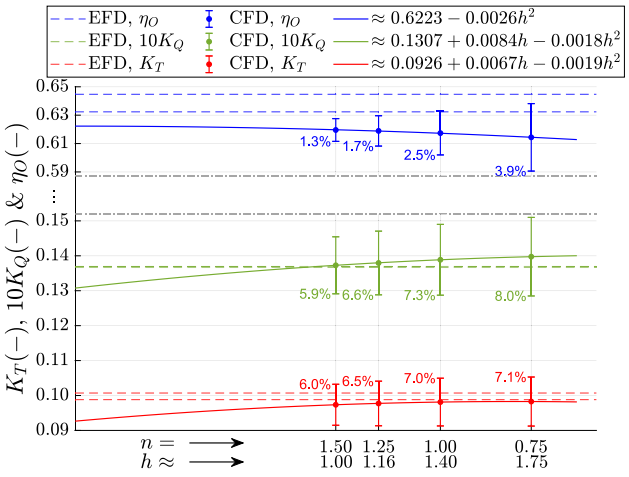

Fig. 12. Grid convergence study in calm water for the simulations incorporating the transition model (TM) at the advance ratio $J \approx 0.55$.

pressure values for the FT simulation on both suction side and pressure side. Interestingly, the more extensive separation seen in TM simulation resulted in a larger reduction of pressure at the trailing edge on the suction side, which is favorable in terms of thrust generation. Nevertheless, the pressure at the trailing edge in both suction and pressure sides must be continuous, therefore, the reduction in the trailing edge on the suction side also reduces the pressure close to the trailing edge on the pressure side, which is unfavorable for thrust generation. This adverse effect on the pressure side is rather significant which may be the main reason for the smaller K_T in TM simulation in comparison to FT simulation seen in Fig. 9.

Fig. 10(e) depicts the Q-criterion isosurface colored by the normalized helicity. Due to the more pronounced separation in TM simulation, the propeller loading drops which leads to a weaker tip vortex formation. The generated vortices near the blade trailing edge in the separation area on the suction side are different between FT and TM simulations. These vortices interact considerably in the TM simulation due to the large radial velocities, leading to a strong trailing edge vortex shedding. Moreover, the trailing root vortices close to the hub is more dispersed in the TM simulation. The discontinuous pattern of the shaft vortices emerges due to a larger separation bubble near the blade root in TM simulation, which potentially exhibits dynamic behavior (unsteady flow). This unsteady flow characteristic may lead to a fragmented hub vortex.

5.3. Validation

In Fig. 11 and Table 3 the propeller characteristics extracted from the FT and TM simulations with the grid $n = 1.00$ are compared to those of EFD data. The results of the repeated model tests at each advance ratio are also presented in Fig. 11. The EFD data at each advance ratio are averaged in order to present a single value representing the EFD data at that advance ratio in Table 3, i.e., $\overline{T_{\text{EFD}}}$, $\overline{K_{T\,\text{EFD}}}$, $\overline{Q_{\text{EFD}}}$, $\overline{K_{Q\,\text{EFD}}}$ and $\overline{\eta_{O\,\text{EFD}}}$. Then, the errors, i.e., E_T, E_{K_T}, E_Q, E_{K_Q} and E_{η_O}, are calculated by subtracting the averaged EFD data from the CFD values, i.e., T_{CFD}, $K_{T\,\text{CFD}}$, Q_{CFD}, $K_{Q\,\text{CFD}}$ and $\eta_{O\,\text{CFD}}$. Thereafter, the propeller characteristics errors in the percentage of the experimental values, i.e., $E\%D_{K_T}$, $E\%D_{K_Q}$ and $E\%D_{\eta_O}$, are presented. Finally, the averaged absolute error $\overline{|E\%D|}$ is computed by taking the average of the absolute errors in all advance ratios in the respective simulation (FT or TM).

It is clear in Fig. 11 and Table 3 that the validation errors are mainly reduced for the TM simulations in comparison to the FT simulations. As discussed before, the dominance of the laminar flow is more relevant in larger advance ratios for the current investigations. Therefore, the benefits of using the transition model are more pronounced in the higher J values, especially for the prediction of torque despite the insignificant errors in dimensional form E_Q. For instance, $E\%D_{K_Q}$ is reduced approximately from 15.2% to 3.8% at $J \approx 0.60$ for TM simulation. The improved thrust and torque predictions resulted in a better prediction of efficiency in all advance ratios.

Although more accurate predictions can be achieved by refining the turbulence source settings and its activation region, this falls beyond the scope of the current investigations as the main objective of this paper focuses on the effects of waves on the POW performance rather than transition modeling. As shown in Table 3, the averaged absolute errors, derived from averaging the absolute errors in different advance ratios, are smaller in the TM simulations in comparison to the FT simulations. This highlights the importance of flow regime on the POW performance in calm water. Thus, for the CFD investigations of the POW performance in calm water, the TM simulations are found to yield reasonably accurate predictions of the propeller characteristics.

5.4. Verification

In the final step of the calm water investigations, the grid convergence study is carried out for the TM simulation setup at the advance ratio $J \approx 0.55$. The simulations are carried out across all of the considered grids, i.e., $n = 0.75$, 1.00, 1.25 and 1.50. It is worth mentioning that the time step is modified based on the grid refinement level, as explained in Section 4.4, in order to keep a similar Courant number between the grids. The results are shown in Fig. 12. The uncertainty value for each grid is presented next to its error bar.

The uncertainty of both thrust and torque coefficients lies within the range of approximately 6% and 8% while it is decreasing for the finer grids. Although the fitted curves from the uncertainty analysis tool in both K_T and $10K_Q$ have the form $\Phi_i = \Phi_0 + \alpha_1 h_i + \alpha_2 {h_i}^2$, the constant coefficients for the second order term α_2 are relatively small in comparison to α_1. Moreover, since the CFD results in different grids are very similar, a linear line may be a better candidate for curve fitting. Furthermore, the estimated exact solutions in the fitted curves are significantly lower than the EFD results whereas the CFD results in all grids are very similar to the EFD data.

The uncertainty of efficiency is lower than those of thrust and torque coefficients, and the fitted curve has the observed order of grid convergence $p = 2$ with a rather small constant coefficient for the second order term. Interestingly, the calculated efficiency derived from the estimated

Table 3
Calm water results of the fully turbulent (FT) simulations and the simulations with the transition model (TM) all with grid $n = 1.00$ in comparison to the EFD data.

$J \approx$		E_T (N) $T_{\text{CFD}} - \overline{T_{\text{EFD}}}$	$E\%D_{K_T}$ (%) $100E_{K_T}/\overline{K_{T\,\text{EFD}}}$	E_Q (N m) $Q_{\text{CFD}} - \overline{Q_{\text{EFD}}}$	$E\%D_{K_Q}$ (%) $100E_{K_Q}/\overline{K_{Q\,\text{EFD}}}$	$E\%D_{\eta_o}$ (%) $100E_{\eta_o}/\overline{\eta_{O\,\text{EFD}}}$
0.35	FT	−1.768	−3.131	0.071	1.520	−5.219
	TM	1.391	0.018	0.053	0.780	−1.419
0.45	FT	−1.324	−3.595	0.045	2.793	−6.572
	TM	−0.758	−2.401	0.003	−0.588	−2.199
0.55	FT	0.245	0.698	0.063	9.481	−8.216
	TM	−0.256	−1.651	0.012	1.508	−3.315
0.60	FT	0.578	3.719	0.068	15.237	−10.250
	TM	−0.158	−1.719	0.019	3.847	−5.628
$\overline{\lvert E\%D \rvert}$	FT	–	2.785	–	7.258	7.564
	TM	–	1.447	–	1.681	3.140

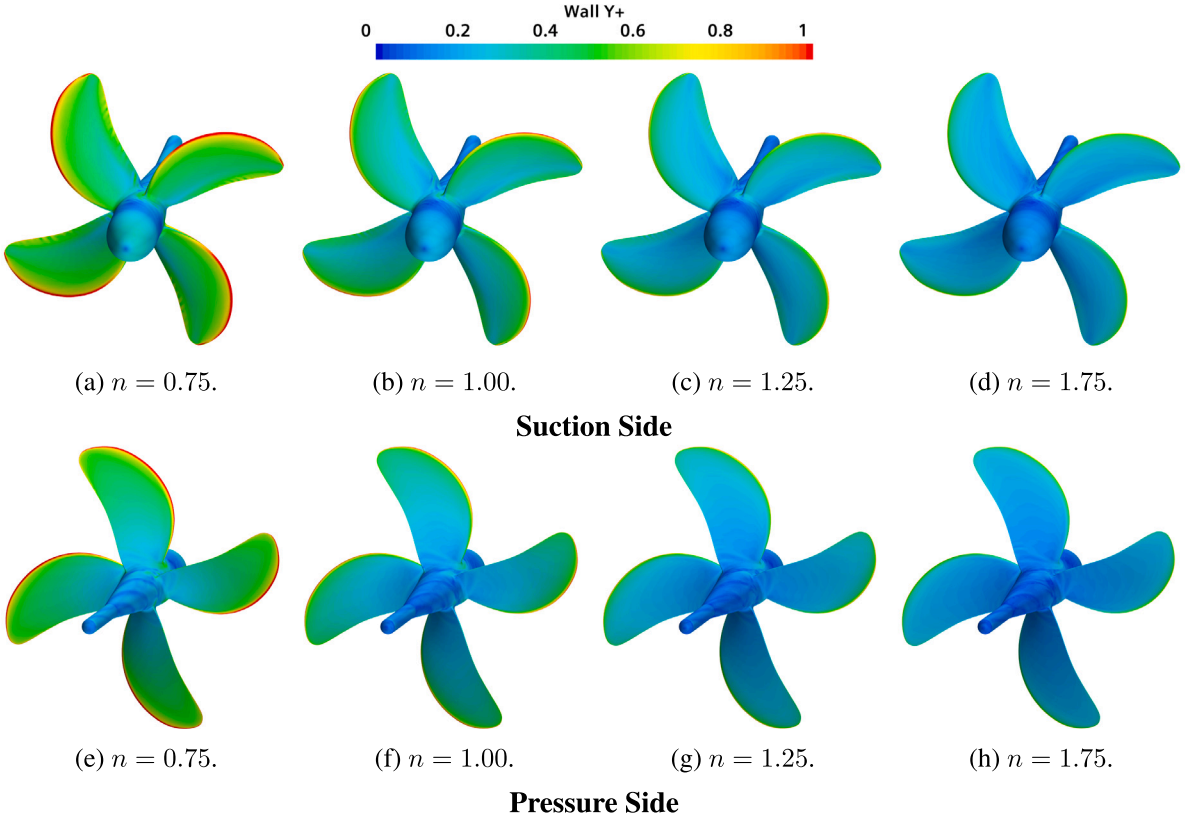

Fig. 13. Wall y^+ distribution on suction side and pressure side of propeller in the last time step of the simulations incorporating the transition model (TM) in calm water at $J \approx 0.55$ and different grids.

exact solutions of the thrust and torque coefficients yields a value of approximately 0.6190, which is lower than the estimated exact solution of efficiency from the grid convergence study (0.6223, as reported in Fig. 12) and closer to the CFD data. Overall, the largest uncertainties are seen for the propeller thrust and torque coefficients, for which the smallest discrepancies between CFD and EFD are observed.

The distribution of wall y^+ values on the suction side and pressure side of the propeller in the last time step of the TM simulations with the adopted transition model in calm water are shown in Fig. 13 for different grids at $J \approx 0.55$. The surface-averaged $\bar{y}^+$ values on the whole propeller geometry are approximately 0.38, 0.27, 0.21 and 0.18 for the coarsest grid to the finest one. On the other hand, the surface-averaged $\bar{y}^+$ values for grid $n = 1.00$ at $J \approx 0.35$, 0.45, 0.55 and 0.60 are approximately 0.38, 0.32, 0.27 and 0.26, respectively.

6. Regular wave - V & V

In this section, the regular head wave results are provided including a convergence assessment as well as an extensive verification and validation analysis of the propeller open water characteristics. The investigations are performed for a series of advance ratios $J = 0.35$, 0.45, 0.55 and 0.60 in four wave conditions (WC) given in Table 2. The CFD simulations in regular head waves are carried out across all of the considered grids, i.e., $n = 0.75$, 1.00, 1.25 and 1.50, for the wave condition WC2 at $J \approx 0.55$, where the grid convergence study is also carried out. However, only the grid $n = 1.00$ is considered for the rest of the simulations in different wave conditions and advance ratios. First, the propeller with the submergence depth of $3R$ is considered for the major part of the investigations, and then the propeller performance in

submergence depth of $2R$ is studied in some selective operational conditions. It is worth mentioning that the convergence criterion, explained in Section 4.6.2, is fulfilled for all of the simulations where STD%RMS remains under 0.2 for both thrust and torque.

The quality of actual incident waves plays an important role in the POW performance operating in regular waves. Based on the preliminary investigations in Irannezhad et al. (2021), insignificant deviations are expected for the numerical waves compared to the analytical ones in the current paper. However, the deviations may become notable between the actual incident waves in the current model tests and the analytical waves, mainly due to the performance of the wave generator and wave dampener systems in the towing tank. Such deviations may be counted as an important source of discrepancy in the validation of the results.

6.1. Experimental results

The reconstructed time series, explained in Section 4.6.3, are shown in Fig. 14 for the experimental measurements carried out in WC2 and different advance ratios. The repeated POW tests are distinguished by the same line color but different line style. The mean values as well as the important harmonic amplitudes are also shown in each respective plot's legend.

The actual incident wave elevation at the propeller plane ζ_{PP} (derived from the wave elevation measurements at the wave gauge) in different model tests are shown in Fig. 14(a). The actual incident wave height H (trough to crest), non-dimensional wave length λ/L and wave steepness H/λ expressed in percentage as well as the 1st and 2nd harmonic amplitudes of wave elevation, i.e., A_1 and A_2, are given in the plot's legend. Although there are some differences seen between the reconstructed time series in different model tests, these discrepancies are rather insignificant and the waves are rather similar to the analytical wave in WC2.

The reconstructed time series of K_T and $10K_Q$ are shown in Figs. 14(b) and 14(c), respectively. Both thrust and torque coefficients in all J values decrease/increase depending on whether the analytical wave crest or trough is located at the propeller disk. Their minimum and maximum occur around $t/T_E \approx 0.25$ and 0.75, respectively. One of the primary contributors to the oscillating torque and thrust values is the alteration of the advance ratio, which arises from the temporal change in advance velocity caused by the wave orbital velocities. In the wave crest/trough the wave orbital velocity in the axial direction becomes maximum/minimum, thus increasing/decreasing the advance ratio resulting on the lower/higher propeller loading and hence thrust and torque. For the repeated model tests with a similar advance ratio J, the thrust and torque coefficients are similar and no significant effects are observed from the differences in the actual incident wave conditions.

The 0th harmonic amplitudes of thrust and torque, i.e., $\bar{K}_T$ and $10\bar{K}_Q$, equal to the mean values of the time series, are decreasing for the higher advance ratios, following the same trend as of calm water. The 1st harmonic amplitude is the dominant harmonic amplitude in all of the conditions and the higher harmonic amplitudes are relatively small. The 1st harmonic amplitudes of both thrust and torque coefficients, i.e., K_{T1} and K_{Q1}, are higher for the higher advance ratios. This may be related to the fact that in the higher advance ratios the propeller rotational speed is lower, hence the effects of the axial component of the wave orbital velocities become more significant on the advance ratio. For instance, in the wave condition WC2, the analytical wave orbital velocity in the axial direction over a representative propeller disk located in the $3R$ submergence depth changes roughly between ± 0.082 m/s during one encounter wave period, resulting in the approximate change of the advance ratio ± 0.042 (obtained from $\pm 0.082/n_P D$) at $J \approx 0.60$ but ± 0.024 at $J \approx 0.35$.

It is interesting that although the reconstructed time series of the propeller open water efficiency, shown in Fig. 14(d), exhibit a rather similar trend as of K_T and K_Q with respect to the wave trough and crest, the harmonic amplitudes are not following a similar trend in different advance ratios. Firstly, although the 1st harmonic amplitude of efficiency η_{O1} is the dominant harmonic amplitude, the 2nd harmonic amplitude η_{O2} is not negligible, especially in the higher advance ratios. Secondly, although η_{O1} is increasing for the higher advance ratios similar to K_{T1} and K_{Q1}, such growths are much more significant for η_{O1} from the smallest advance ratio to the highest one. Last but not least, the mean value of efficiency $\bar{\eta}_O$ increases from $J \approx 0.35$ to 0.55 and again decreases at $J \approx 0.60$.

The smaller $\bar{\eta}_O$ in waves in comparison to the calm water value at $J \approx 0.60$ can be basically perceived by looking at the calm water efficiency curve in Fig. 8 and considering the variation of advance ratio approximately between 0.60 ± 0.042 due to the axial component of the wave orbital velocities. The variation of J and the non-linear behavior of the efficiency curve around this advance coefficient leads to a smaller mean value $\bar{\eta}_O$ compared to the calm water value. However, one important point is that in all advance ratios a similar trend as of K_T and K_Q is seen for η_O with respect to the analytical free surface elevation above the propeller. Nonetheless, the trend of η_O at lower advance ratios cannot be justified by considering the propeller open water efficiency curve in calm water and the temporal change of advance ratio due to the axial component of the wave orbital velocities. To get the full picture, it is required to consider the possible effects of both axial and vertical wave orbital velocities on the flow regime as well as any alternation within the associated physical phenomena, such as flow separation. For instance, a significant decrease in the reconstructed time series of η_O at $J \approx 0.60$ is seen close to the wave crest $t/T_E \approx 0.25$ which may represent a more significant deterioration of the generated thrust at the time of the less significant torque deterioration.

The reconstructed time series in the other wave conditions also exhibit a similar behavior to the one presented here for WC2, hence they are provided in Figs. A.1–A.3 in Appendix, but not analyzed individually in this paper.

6.2. Transition modeling

The POW performance in the wave condition WC2 is compared with the calm water results in Fig. 15. The CFD results include the fully turbulent flow simulations (FT) and the simulations incorporating the transition model (TM) with the adopted source condition (TI = 0.5%, TVR = 10) all with the grid $n = 1.00$.

The 0th harmonic amplitudes (mean values) are shown in Fig. 15(a). It should be reminded that the mean propeller efficiency $\bar{\eta}_O$ in this plot is derived from averaging the instantaneous propeller open water efficiency calculated based on the instantaneous thrust and torque coefficients. However, the difference between $\bar{\eta}_O$ calculated from the instantaneous efficiency and from the mean thrust and torque coefficients is very small, hence the mean thrust and torque coefficients can be used for an overall analysis here.

A significant reduction of the mean propeller efficiency $\bar{\eta}_O$ is observed at the higher advance ratios from calm water to WC2 for the EFD data. This mainly originates from the decrease of $\bar{K}_T$ and an slight increase of $10\bar{K}_Q$ in waves in comparison to calm water. Similar to the explanations given for the mean efficiency at $J \approx 0.60$ in Fig. 14(d), the variation of $\bar{K}_T$ and $10\bar{K}_Q$ in waves in comparison to calm water can be justified to some extent by taking into account the calm water curves in Fig. 8 and considering the change of advance ratio due to the axial component of the wave orbital velocities, keeping in mind that such fitted curves are not linear. However, as mentioned before, the variation of the mean values of the propeller characteristics in waves in comparison to the calm water values is more complicated than just considering the calm water curves, because of the complex change of the encountered flow field in waves.

From the CFD investigations, it is observed that the FT simulations results in calm water and WC2 are almost identical. The same is

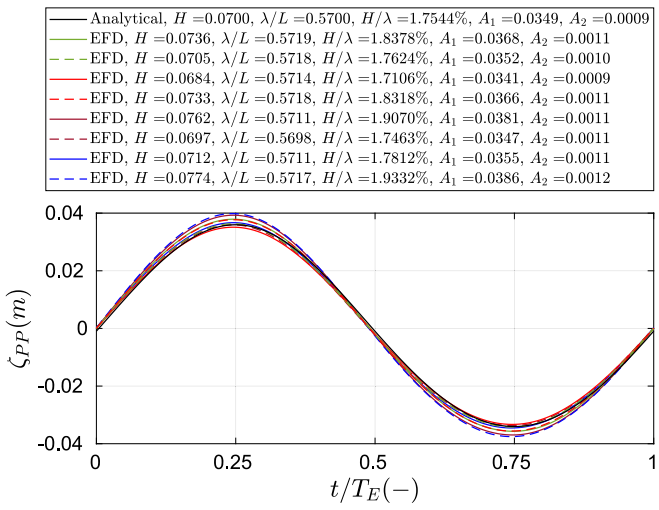

(a) Wave elevation at propeller center.

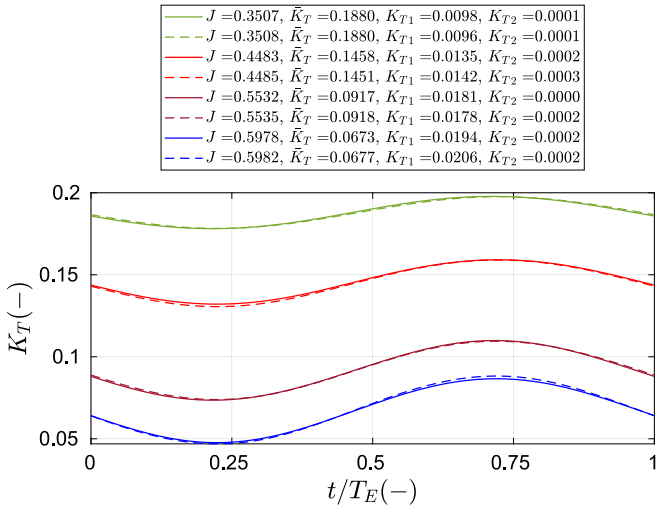

(b) Thrust coefficient.

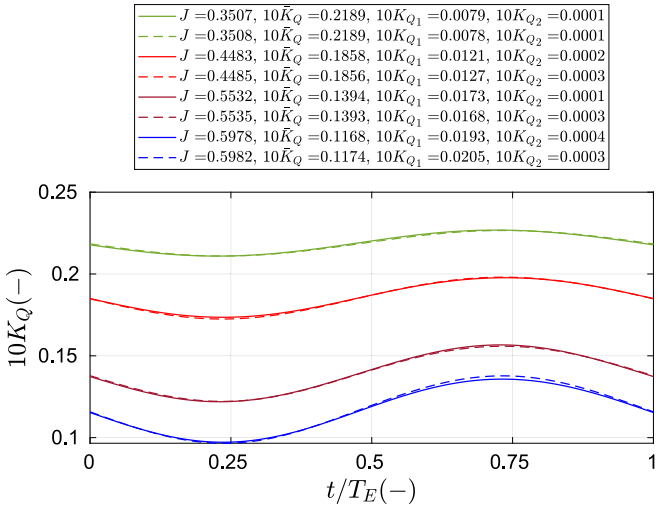

(c) Torque coefficient.

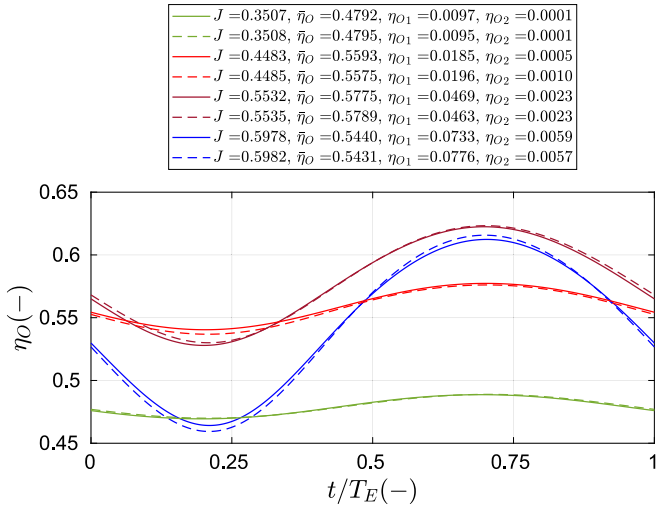

(d) Efficiency.

Fig. 14. Reconstructed time series of experimental measurements results in wave condition WC2.

also valid for the TM simulations results in calm water and waves. Therefore, neither FT nor TM RANS simulations are solely capable of resolving the full effects of waves on the propeller performance in comparison to the calm water conditions for the investigated operational conditions. For the studied operational conditions in this paper, the usage of a transition model is promoted for capturing the laminar flow dominance in calm water simulations, explained in Section 5. However, such laminar flow dominance may not hold in the case of regular head waves, because of the complex change of the encountered flow field in waves due to the unsteady and non-uniform oblique flow environment as well as the presumably higher turbulence level in the towing tank during the tests in waves. Based on the EFD data, there is a clear change of propeller characteristics in waves in comparison to calm water, which may be related to this change of flow regime on the blades.

The main discrepancies of the thrust and torque coefficient between EFD and CFD in waves are seen at the higher advance ratios, whereas at the smaller J values the EFD and CFD are rather close. Although the TM simulations results for $10\bar{K}_Q$ at $J \approx 0.55$ and 0.60 are very similar to the EFD data, $\bar{K}_T$ is over-predicted, resulting in significant over-prediction of $\bar{\eta}_O$. Moreover, a simulation with fully laminar considerations are also carried out in WC2 at $J \approx 0.55$ (not provided in the plot), in which the predicted propeller characteristics ($\bar{K}_T = 0.0947$, $\bar{K}_Q = 0.135$ and $\bar{\eta}_O = 0.610$) are rather close to the TM simulations results. On the other hand, both $\bar{K}_T$ and $10\bar{K}_Q$ are over-predicted by the FT simulations at $J \approx 0.55$ and 0.60. In Section 5.2, it is discussed that although the thrust and torque predictions should be mainly examined as the physics-related quantities, the assessment of the predicted propeller open water efficiency may provide extra information about the correlation between the predicted thrust and torque. Here the predicted $\bar{\eta}_O$ from the FT simulations are much closer to the EFD data than predictions by the TM simulations.

The 1st harmonic amplitudes of the thrust, torque and efficiency, i.e., K_{T1}, K_{Q_1} and η_{O1}, in WC2 are shown in Figs. 15(b)–15(d), respectively. In order to take into account the actual incident wave height measurements in the model tests, the normalized 1st harmonic amplitudes of the thrust, torque and efficiency by the measured wave height in each respective model test are also provided. To this end, K_{T1}, K_{Q_1} and η_{O1} are normalized by (H/D). Interestingly, the results of the repeated model tests at each advance ratio tend to be very similar

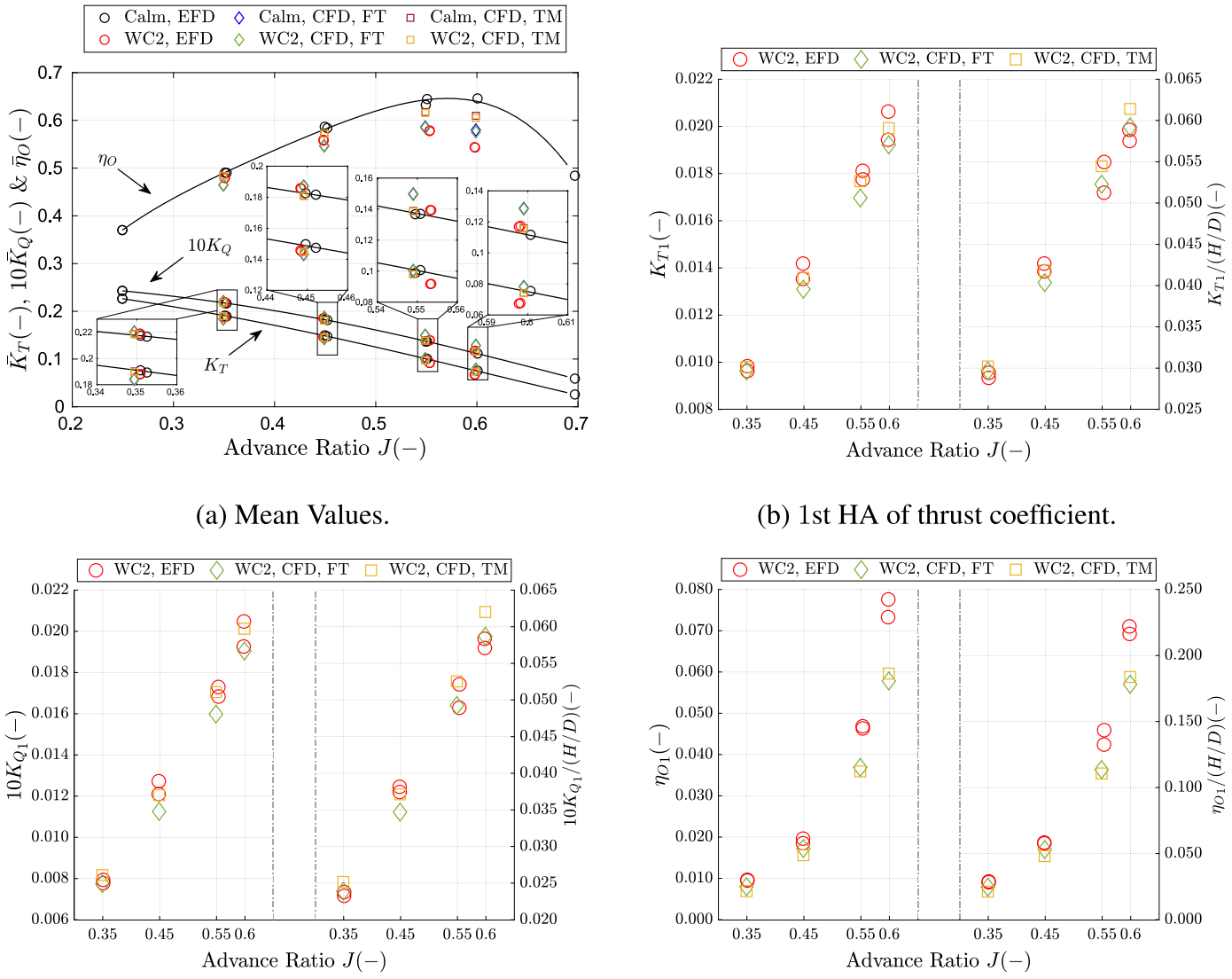

(a) Mean Values.

(b) 1st HA of thrust coefficient.

(c) 1st HA of torque coefficient.

(d) 1st HA of efficiency.

Fig. 15. EFD and CFD (only with grid $n = 1.00$) results of the propeller performance in wave condition WC2 in terms of the mean values (a) as well as the 1st harmonic amplitudes (b, c, d) both in their original form (left) and when normalized to the actual incident waves (right) in model tests.

for the normalized quantities. This may reveal an approximate linear relation between the wave height and the 1st harmonic amplitudes of the propeller characteristics that will be addressed later in this paper. In order to normalize the CFD data, the analytical wave height is used as the waves in the CFD are expected to be very similar to their analytical counterpart.

Although the 1st harmonic amplitudes of thrust and torque coefficients from the FT and TM simulations are very similar, FT results are slightly closer to the EFD data at $J \approx 0.60$. The largest discrepancies are seen for the 1st harmonic amplitudes of propeller efficiency at $J \approx 0.55$ and 0.60 where both FT and TM simulations under-predicted η_{O1}. These may reflect the under-resolved physical phenomena in both TM and FT simulations that were present in the experiments, despite the aforementioned possible sources of discrepancies. It is worth noting that here in this study the RANS approach is employed which inherently includes simplifications and approximations that may have shortcomings in capturing the flow physics. Higher fidelity turbulence models, such as Large Eddy Simulation, are recommended to carry out similar investigations as the ones performed here. Nevertheless, in Section 7 a detailed analysis of the flow from the current RANS investigations, regardless of the existing discrepancies versus EFD, is presented for identification of the impacts of waves on propeller performance in comparison to calm water from the hypothetical flow regime change perspective.

Overall, the better predictions of the 1st harmonic amplitudes of thrust and torque coefficients as well as the more accurate results of the mean propeller efficiency at the higher advance ratios from the FT simulations motivate the use of the FT setup to perform the remaining simulations in regular head waves. Therefore, the TM simulations in calm water and the FT simulations in regular head waves are the main focus of the presented results henceforth.

6.3. Validation

In Fig. 16 the reconstructed time series are compared between EFD and CFD (only for FT simulations with grid $n = 1.00$) for different wave conditions at $J \approx 0.55$. The reconstructed time series at $J \approx 0.35$, 0.45 and 0.60 are provided in Appendix in Figs. A.4–A.6, but not analyzed individually here. The results of the repeated model tests are all plotted with the same line style and color. In the legends of the plots for the

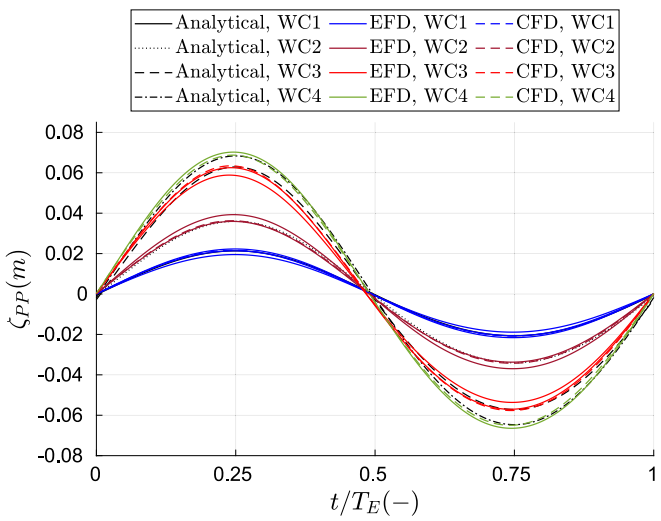

(a) Wave elevation at propeller center.

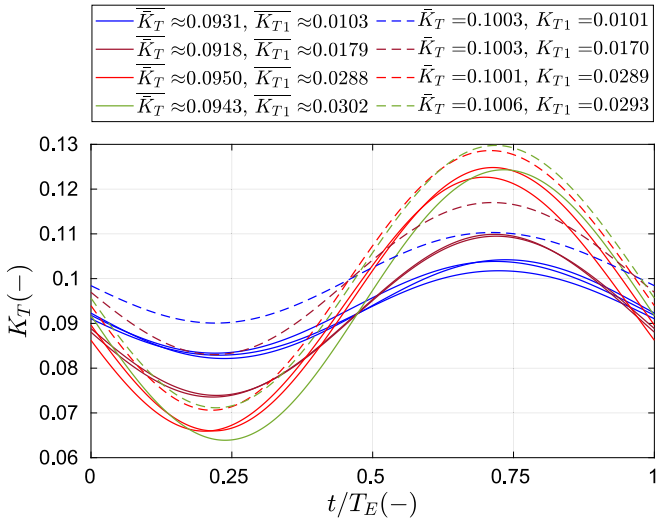

(b) Thrust coefficient.

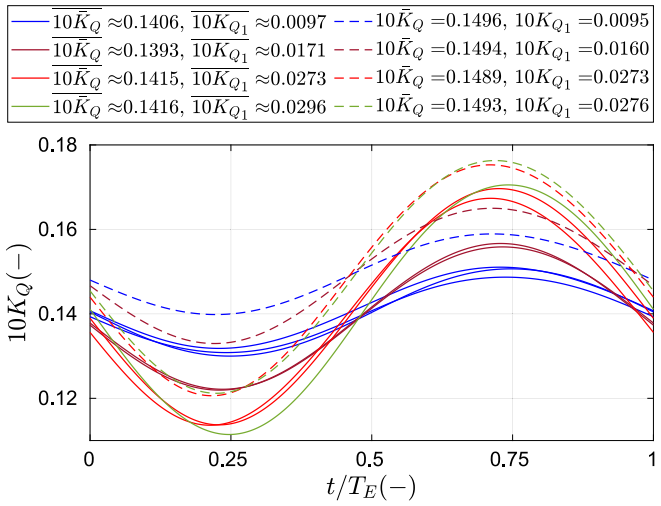

(c) Torque coefficient.

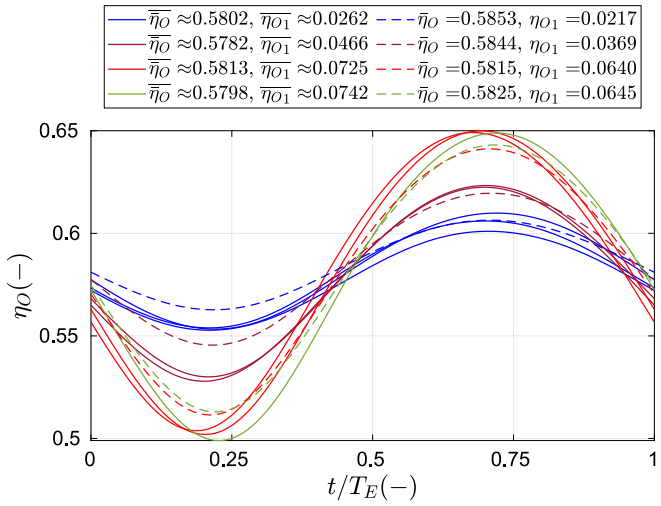

(d) Efficiency.

Fig. 16. Reconstructed time series from the results of EFD and CFD (only for FT simulations with grid $n = 1.00$) in different wave conditions at $J \approx 0.55$.

thrust, torque and efficiency, the 0th and 1st harmonic amplitudes of each quantity are provided. For the EFD data, the averaged values over all the repeated model tests are shown as $\overline{\bar{K}_T}$, $\overline{\bar{K}_Q}$, $\overline{\bar{\eta}_O}$, $\overline{K_{T1}}$, $\overline{K_{Q1}}$ and $\overline{\eta_{O1}}$.

The reconstructed incident wave elevation at propeller plane in EFD and CFD is rather close to the analytical wave in each wave condition in Fig. 16(a). It is also worth mentioning that the wave length and hence encounter wave period T_E is different in WC4 in comparison to the other wave conditions, however, the reconstruction is carried out in a way to have $1 \times T_E$ in all of the wave conditions.

The overall trends of thrust, torque and efficiency with respect to the analytical incident wave elevation at the propeller plane are similar in all of the wave conditions which are also similar to the ones seen in Fig. 14. It is interesting that there are no significant changes in the mean values for thrust, torque and efficiency between different wave conditions, in both EFD and CFD. On the other hand, the 1st harmonic amplitudes of these quantities are increasing from WC1 to WC4. Although the wave steepness of WC2 and WC4 are rather similar, the 1st harmonic amplitudes are quite different. However, the 1st harmonic amplitudes exhibit a relatively close proximity for WC3 and WC4, revealing the dependency of the 1st harmonic amplitudes to the wave height, as the wave height is slightly higher in WC4 and so the 1st harmonic amplitudes.

The 1st harmonic amplitudes of thrust and torque demonstrate close similarity between EFD and CFD, while the mean values of thrust and torque are over-predicted by CFD. In contrast to the similarity of propeller mean efficiency obtained from CFD and EFD, the 1st harmonic amplitudes of efficiency exhibit significant differences. These observations are very similar to the ones seen in Fig. 15 for the wave condition WC2 at $J \approx 0.55$.

In order to obtain a better understanding of the effects of regular head waves on the POW performance, the propeller characteristics in all of the considered regular head waves and advance ratios are compared to those of calm water in Fig. 17. Only the TM simulations results in calm water and FT simulations results in regular head waves are presented. Furthermore, the propeller characteristics extracted from the FT simulations with the grid $n = 1.00$ in regular head waves are compared to those of EFD data in Table 4. The simulations in each wave condition cover different advance ratios, as presented in this table.

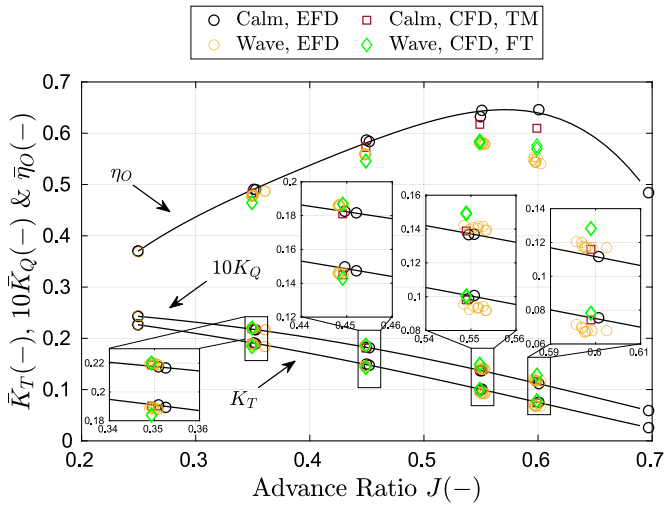

(a) Mean values.

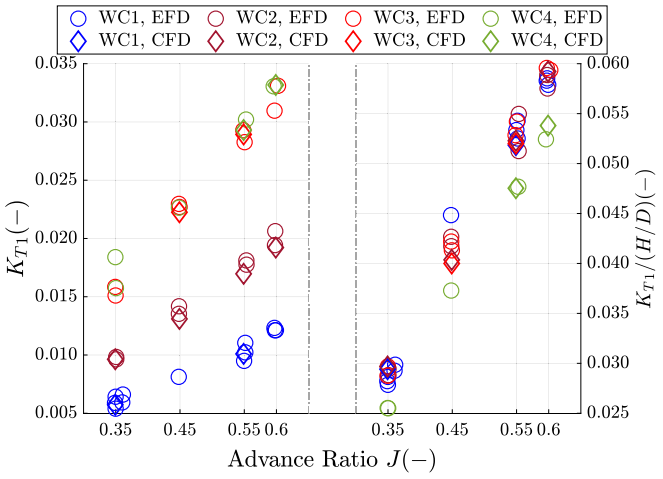

(b) 1st HA of thrust coefficient.

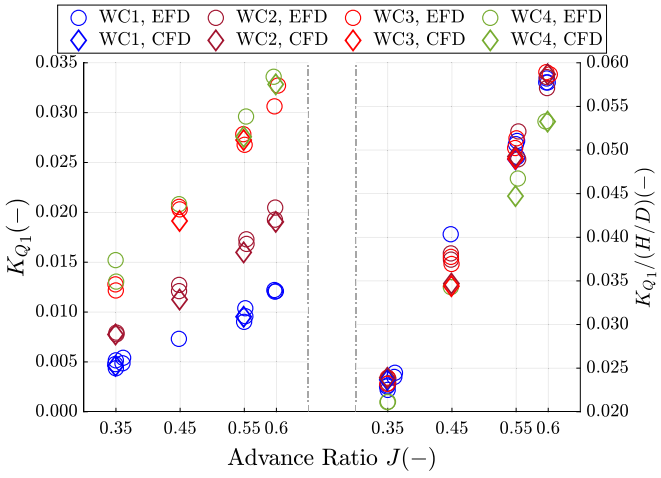

(c) 1st HA of torque coefficient.

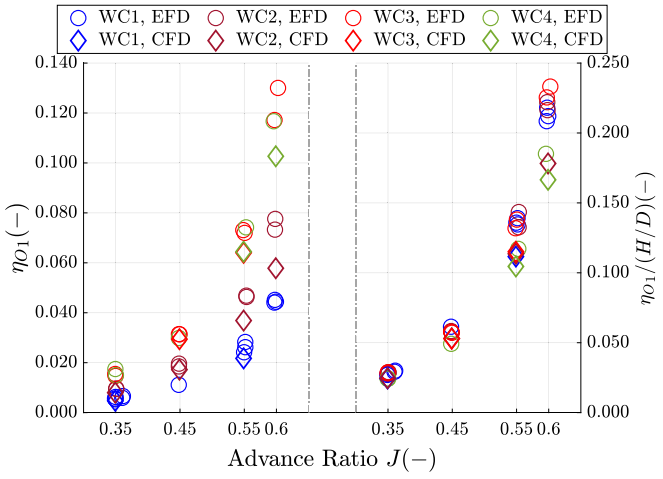

(d) 1st HA of efficiency.

Fig. 17. EFD and CFD (TM simulation in calm water and FT simulation in waves all with the grid $n = 1.00$) results of the propeller performance in terms of the mean values as well as the 1st harmonic amplitudes with and without taking into account the effects of the actual incident waves in model tests in all studied wave conditions and advance ratios.

The mean values as well as the 1st harmonic amplitudes of the propeller characteristics are also presented in Table 4. The results of repeated model tests at each wave condition and at each advance ratio are averaged in order to present a single value in this table representing the EFD data, i.e., $\overline{\bar{T}_{\text{EFD}}}$, $\overline{\bar{K}_{T\,\text{EFD}}}$, $\overline{\bar{Q}_{\text{EFD}}}$, $\overline{\bar{K}_{Q\,\text{EFD}}}$ and $\overline{\bar{\eta}_{O\,\text{EFD}}}$ for the mean values as well as $\overline{K_{T\,1\text{EFD}}}$, $\overline{K_{Q\,1\text{EFD}}}$ and $\overline{\eta_{O\,1\text{EFD}}}$ for the 1st harmonic amplitudes. Then, the errors, i.e., $E_{\bar{T}}$, $E_{\bar{K}_T}$, $E_{\bar{Q}}$, $E_{\bar{K}_Q}$ and $E_{\bar{\eta}_O}$ for the mean values as well as $E_{K_{T1}}$, $E_{K_{Q1}}$ and $E_{\eta_{O1}}$ for the 1st harmonic amplitudes, are calculated by subtracting the averaged EFD values from the CFD values, i.e., $\bar{T}_{\text{CFD}}$, $\overline{K}_{T\,\text{CFD}}$, $\bar{Q}_{\text{CFD}}$, $\overline{K}_{Q\,\text{CFD}}$ and $\overline{\eta}_{O\,\text{CFD}}$ for the mean values as well as $K_{T\,1\text{CFD}}$, $K_{Q\,1\text{CFD}}$ and $\eta_{O\,1\text{CFD}}$ for the 1st harmonic amplitudes. Thereafter, the propeller characteristics errors in percentage of the experimental values, i.e., $E\%D_{\bar{K}_T}$, $E\%D_{K_{T1}}$, $E\%D_{\bar{K}_Q}$, $E\%D_{K_{Q1}}$, $E\%D_{\bar{\eta}_O}$ and $E\%D_{\eta_{O1}}$, are presented. Finally, the averaged absolute error $\overline{|E\%D|}$ is computed from averaging the absolute of errors at all advance ratios and in all wave conditions.

In Fig. 17(a) the mean values of the propeller characteristics are compared between EFD and CFD, both in calm water (only TM CFD simulations) and in waves (only FT CFD simulations). The same plot marker is used for all the considered waves. The first observation is that the EFD mean values in all of the examined waves are clustered at each advance ratio. Thus, a similar effect is seen by different waves. The same conclusion can be derived for the CFD, as the results in different waves at the same advance ratio are almost identical. However, the discrepancy between EFD and CFD that has been observed for WC2 in Fig. 15(a) persists here as well. Such discrepancies for the mean thrust and torque coefficients are smaller for the smaller advance ratios and larger for the higher advance ratios, which can be observed by the values of $E\%D_{\bar{K}_T}$ and $E\%D_{\bar{K}_Q}$ at different wave conditions in Table 4.

The large discrepancies at $J \approx 0.55$ and 0.60 reveals over-predictions of CFD for mean thrust and torque coefficients, while the mean propeller efficiency and hence the correlation between the thrust and torque agrees better between CFD and EFD. The average absolute error $\overline{|E\%D|}$ for the mean values of the thrust and torque coefficients are approximately 6.3% and 4.2% respectively, which are higher than $\overline{|E\%D|}$ in calm water for the TM simulation (1.4% and 1.7%). On the other hand, $\overline{|E\%D|}$ for the mean propeller efficiency is almost similar between the TM simulations in calm water (3.1%) and FT simulations in waves (2.3%)

Overall, based on the experimental measurements, at the higher advance ratios, i.e., $J \approx 0.55$ and 0.60, the mean values of the

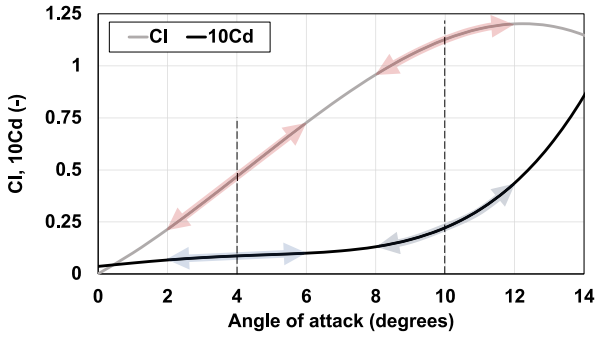

Fig. 18. Schematic presentation of lift and drag coefficients of a two-dimensional hydrofoil against angle of attack.

thrust/torque coefficient are reduced/increased in regular waves in comparison to calm water, however, they stay almost unaffected at the lower advance ratios. In the experimental test setup, the propeller rotation speed was used to achieve the desired advance ratio. Higher advance ratios are obtained through reduced propeller rotation speed. As can be concluded from Fig. 6, decreased propeller speed results in increased geometric advance angle. A more detailed analysis of geometric advance angle variation in calm water and in waves are presented in Sections 7.1.2 and 7.2.2.

Fig. 18 shows a schematic representation of lift and drag coefficients for a generic two-dimensional hydrofoil. As observed here, lift coefficient increases almost linearly with increased angle of attack until stall occurs. In contrast, drag coefficient forms a so called bucket where its variation are marginal for the angle of attacks inside the drag bucket, however, it increases exponentially at higher angle of attacks. Therefore, it can be concluded that the lower advance ratios are operating points well inside the drag bucket and within the linear lift coefficient range, but the higher advance coefficients are closer to the edge of the drag bucket where the drag coefficient increases exponentially as well as lift stall angle. These two distinct ranges are schematically highlighted in Fig. 18 assuming that the angle of attack oscillates ±2 degrees. The altering inflow velocity in waves, caused by the orbital velocity of the waves, results in oscillation of angle of attack. As seen in Fig. 18, the oscillation of lift and drag coefficients caused by such oscillations can be linear for smaller angle of attacks, resulting in unchanged mean value of lift and drag. However, due to proximity with the outer ranges of drag bucket, the averaged drag coefficient increases for higher angle of attacks, while the average lift coefficient may drop due to proximity with lift reduction rang caused by stall. This is the hypothesis that we have for explaining the reasons behind reduced/increased thrust/torque coefficient in regular waves.

Unlike the EFD results, the above mentioned trends are not captured in the CFD. We speculate that the unsteady and non-uniform encountered flow field in waves in conjunction with the disturbances generated from the wave maker flaps in the towing tank as well as potential inevitable asymmetric conditions (e.g., slight misalignment of the shaft with respect to the inflow direction) and mechanical interference (e.g., shaft line vibrations, explained in Section 4.6.3) in the experiments may alter the flow behavior over the blades. Consequently, these can introduce a different flow transition, separation and coherent structures behavior and hence distinct thrust and torque measurements in comparison to the fairly ideal conditions in CFD. In Section 7, further analysis is carried out for a selective operational condition using the CFD results, despite the present under-resolved challenges, in order to identify the possible origins.

The 1st harmonic amplitudes of the propeller characteristics in regular head waves as the dominant harmonic amplitudes are compared between EFD and CFD in Figs. 17(b)–17(d). Similar observations as the ones discussed for Fig. 15 for the wave condition WC2 are seen for the other wave conditions. In each wave condition, K_{T1}, K_{Q1} and η_{O1} are increasing for the higher advance ratios, which is already justified by considering the change of advance velocity according to the axial component of the wave orbital velocities. Moreover, in each advance ratio the 1st harmonic amplitudes are increasing for the larger wave heights, except the rather similar values between WC3 and WC4. The normalized values using the actual wave heights are very close at each advance ratio, which may confirm the approximate linear relation between the 1st harmonic amplitudes to the wave height. However, again the WC4 does not follow the same trend and the normalized values are quite different from other waves. It should be reminded that the wave length is different in WC4 which might propose another factor for the dependency of the 1st harmonic amplitudes. Moreover, it was seen that the higher harmonic amplitudes become noticeable for the wave conditions with larger wave heights, hence defying the approximate linear relation between the 1st harmonic amplitude and the wave height.

Overall, a good agreement is seen between the EFD and CFD results for the 1st harmonic amplitudes of thrust and torque coefficients. Based on $E\%D_{K_{T1}}$ and $E\%D_{K_{Q1}}$ in Table 4, both K_{T1} and K_{Q1} are mainly under-predicted by CFD with the averaged absolute errors of approximately 2.7% and 4.1%, respectively. However, the largest discrepancies are seen for the 1st harmonic amplitude of efficiency η_{O1} which is significantly under-predicted with an averaged absolute error of 14.7%. No clear trend between different advance ratios for $E\%D_{K_{T1}}$, $E\%D_{K_{Q1}}$ and $E\%D_{\eta_{O1}}$ is detected.

6.4. Verification

In Fig. 19, the grid convergence study is carried out for the FT simulation setup in wave condition WC2 at the advance ratio $J \approx 0.55$. The simulations are carried out across all of the considered grids, i.e., $n = 0.75$, 1.00, 1.25 and 1.50, with modified time steps to keep a similar Courant number.

The numerical uncertainties of the mean values of the propeller characteristics, shown in Fig. 19(a), are mostly smaller than the calm water values in Fig. 12. Nevertheless, it is important to highlight that, unlike the simulations in calm water, the simulations in waves are conducted without transition modeling. This difference could be a contributing factor to the reduced numerical uncertainties of torque and thrust coefficients in wave simulations. Similar to calm water, the numerical uncertainty of $\bar{\eta}_O$ is smaller than $\bar{K}_T$ and $\bar{K}_Q$. On the other hand, the numerical uncertainties of the 1st harmonic amplitudes are significantly large, especially for K_{Q1} and η_{O1}. Clearly, similar to the calm water grid convergence study conclusions, a linear line may be a better candidate for curve fitting.

6.5. Submergence depth effects

The calm water investigations are carried out only with the submergence depth of $3R$. Zhang et al. (2021a) observed no effects on the propeller characteristics from change of submergence in calm water for a fully-submerged and non-ventilating propeller. However, the submergence depth can have a significant impact in waves as the magnitude of the wave orbital velocities vary based on depth. In order to have an overview of the possible impacts, the POW tests as well as CFD simulations (FT with grid $n = 1.00$) in $2R$ submergence depth are carried out in wave condition WC2 at two advance ratios $J \approx 0.55$ and 0.60. The propeller characteristics in terms of the mean values and the normalized 1st harmonic amplitudes by the actual incident wave height are shown in Fig. 20.

The mean values of thrust, torque and efficiency from the CFD computations are almost identical in both submergence depths. However, the 1st harmonic amplitudes from the CFD are increased for the $2R$ submergence condition in comparison to $3R$, which may reveal the

Table 4
Regular head waves results of the fully turbulent (FT) simulations with grid $n = 1.00$ in comparison to the EFD data.

WC	$J \approx$	$E_{\bar{T}}$ (N) $\bar{T}_{\text{CFD}} - \overline{\bar{T}_{\text{EFD}}}$	$E\%D_{\bar{K}_T}$ (%) $100E_{\bar{K}_T}/\overline{\bar{K}_{T\,\text{EFD}}}$	$E\%D_{K_{T1}}$ (%) $100E_{K_{T1}}/\overline{K_{T1\,\text{EFD}}}$	$E_{\bar{Q}}$ (N m) $\bar{Q}_{\text{CFD}} - \overline{\bar{Q}_{\text{EFD}}}$	$E\%D_{\bar{K}_Q}$ (%) $100E_{\bar{K}_Q}/\overline{\bar{K}_{Q\,\text{EFD}}}$	$E\%D_{K_{Q_1}}$ (%) $100E_{K_{Q_1}}/\overline{K_{Q1\,\text{EFD}}}$	$E\%D_{\bar{\eta}_O}$ (%) $100E_{\bar{\eta}_O}/\overline{\bar{\eta}_{O\,\text{EFD}}}$	$E\%D_{\eta_{O1}}$ (%) $100E_{\eta_{O1}}/\overline{\eta_{O1\,\text{EFD}}}$
WC1	0.35	−2.078	−2.273	−2.961	0.012	0.317	−3.350	−2.642	−17.405
	0.55	1.706	7.758	−1.559	0.046	6.361	−1.363	0.864	−17.162
WC2	0.35	−1.284	−2.189	−1.001	0.035	0.537	−1.326	−3.120	−16.457
	0.45	−0.897	−1.713	−5.486	0.005	0.647	−9.305	−2.201	−9.643
	0.55	2.159	9.253	−5.389	0.057	7.215	−6.342	1.075	−20.860
	0.60	1.882	15.608	−4.044	0.042	9.497	−4.160	5.901	−23.344
WC3	0.45	−1.095	−2.397	−2.559	0.002	0.160	−6.320	−2.542	−6.335
	0.55	1.201	5.403	0.530	0.037	5.190	−0.196	0.036	−11.751
WC4	0.55	1.693	6.620	−2.984	0.046	5.457	−6.874	0.461	−13.136
	0.60	1.167	9.612	0.347	0.026	6.368	−2.262	3.737	−12.027
$\overline{\lvert E\%D \rvert}$		–	6.283	2.686	–	4.175	4.150	2.258	14.750

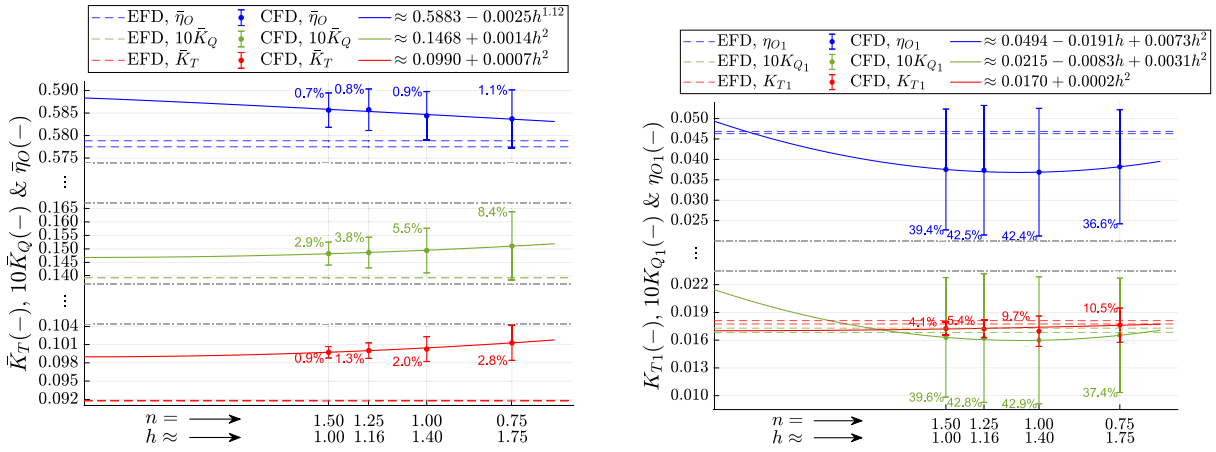

(a) Mean values. (b) 1st harmonic amplitudes.

Fig. 19. Grid convergence study in wave condition WC2 for the fully turbulent (FT) simulations at the advance ratio $J \approx 0.55$.

higher magnitudes of the wave orbital velocities closer to water surface in the $2R$ submergence.

The mean values from the EFD data represent almost similar $10\bar{K}_Q$ but slightly larger $\bar{K}_T$ and hence larger $\bar{\eta}_O$ for the $2R$ submergence. It is interesting that most of the mean propeller characteristics for the EFD and CFD data are more similar in $2R$ submergence in comparison to $3R$. The discrepancies of mean torque and thrust coefficients between CFD and EFD are smaller in 2R compared to 3R.

The 1st harmonic amplitudes from EFD are increased for the submergence $2R$.

7. Analyses and discussions

In Sections 5 and 6, the verification and validation of the POW performance simulations in different operational conditions in calm water and regular head waves are presented including a comprehensive analysis of the propeller characteristics. In the current section, more in-depth analysis of the flow field, computed integral forces and moments as well as the single-blade load variations from the simulations is carried out in a few selective operational conditions. To this end, only the simulations with the grid $n = 1.00$ at $J \approx 0.55$ in $3R$ submergence depth are analyzed. At the end of this section, the computational cost for running the CFD simulations is presented.

7.1. Calm water

In Table 5 the contribution of the pressure and shear components of the thrust and torque to the total value is analyzed for FT and TM simulations (in the last time step) in calm water with grid $n = 1.00$ at $J \approx 0.55$. In both FT and TM simulations, the pressure component of both thrust and torque is the dominant component. For the thrust, the shear component has an opposite sign but its contribution is substantially smaller than the pressure component. The dominance of the pressure component for torque is less pronounced compared to thrust, but still fairly significant.

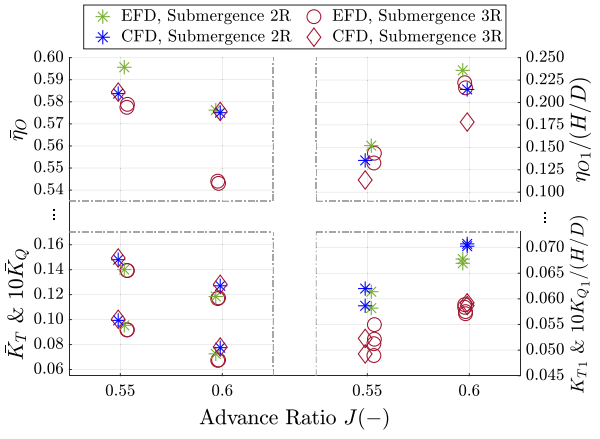

Fig. 20. EFD and CFD (only grid $n = 1.00$ and FT) results of the propeller performance in different submergence in terms of the mean values and the 1st harmonic amplitudes in wave condition WC2 in two advance ratios.

Table 5
Contribution of the pressure and shear components of thrust and torque in FT and TM simulations (last time step) in calm water with grid $n = 1.00$ at $J \approx 0.55$.

	Thrust (N)			Torque (N m)		
	FT	TM	100(FT−TM)/TM (%)	FT	TM	100(FT−TM)/TM (%)
Total	21.468	20.918	2.63	0.690	0.639	7.98
Pressure	22.006	21.249	3.56	0.579	0.572	1.22
Shear	−0.538	−0.331	62.54	0.111	0.067	65.67
|Pressure/Shear|	40.9	64.2	–	5.2	8.5	–

Based on the discussions in Section 5, more extensive separation (over the suction side of the propeller blades) is predicted by the TM simulation in comparison to the FT simulation. This together with the dominance of the laminar flow over the blades are found to be the main reasons for the thrust and torque differences seen between FT and TM simulations. According to Table 5 at $J \approx 0.55$, the total thrust is decreased around 2.63% from FT to TM simulation, where the pressure component decreased around 0.76 N and shear component increased 0.21 N. Although the variation of the shear component of thrust is significant in terms of percentage (62.54%), the pressure component is found to be more affected in terms of magnitude between these simulations. On the other hand, the decrease of total torque from FT to TM simulation is rather significant, which is mainly derived from the substantial decrease of the shear component (0.044 N m) compared to the smaller decrease of the pressure component (0.007 N m). These results reveal that transition effects lead to drop of total thrust originated mainly by the drop of pressure component, and drop of total torque originated from the substantial drop of the shear component.

Aside from the thrust and torque which are the force and moment defined based on the longitudinal axis of the Cartesian coordinate system (X), the forces and moments in the transversal (Y) and vertical (Z) axes of the coordinate system can be studied. These forces and moments are called T_Y and T_Z for forces as well as Q_Y and Q_Z for moments. In calm water simulations, most of these forces and moments are negligible, except T_Z (which is around 1.63 N at $J \approx 0.55$) which arises from the propeller induced disturbances on the free surface.

7.1.1. Single-blade analysis

Fig. 21 depicts the contribution of each blade (a single value for each blade representing the averaged value on that blade) in the total thrust and torque in the last time step of the FT and TM simulations at $J \approx 0.55$, as subsidiary information to Fig. 10. Due to the uniform inflow, the loading, both for thrust and torque, on different blades are very similar in terms of magnitude in each individual simulation. The small differences are speculated to be related to the disturbed free surface (due to the propeller action and suction of the free surface above the propeller center), resulting in a slightly lower loading on the blade at the azimuthal position $\theta \approx 30°$ and higher loading on the blade at $\theta \approx 210°$, in both FT and TM simulations. One interesting observation is that the thrust on the blades at $\theta \approx 120°$ and $\theta \approx 300°$ are almost equal, but the torque is different. However, such differences in terms of magnitude are very small since the color bar bound is limited to a small range. These unbalanced distributions of forces are the key reason for the observed large vertical force T_Z. Overall, the higher total loading in the FT simulation in comparison to TM simulation, which is also seen in Table 5, can be observed on each blade as well.

7.1.2. Incident flow field

In Fig. 22, the geometric advance angle distribution on a representative propeller disk (explained in Section 4.6.4) is shown in the calm water simulations at $J \approx 0.55$. Since the representative propeller disk is located in a position with negligible effects from the propeller (inconsequential propeller induced velocities), β is almost identical between the FT and TM simulations, hence only the FT simulation result is shown.

Due to the uniform inflow in the axial direction, the distribution of β over the disk is solely affected by the distribution of the geometric pitch angle (shown in Fig. 7) and the angular velocity at each radius caused by the propeller rotational speed. Therefore, the distribution of the geometric advance angle is almost constant in the azimuthal θ direction, but varying in radial direction, in which the maximum values ($\beta \approx 5°$) are seen approximately in $0.4 < r/R < 0.6$. The surface-averaged value of the geometric advance angle over the representative propeller disk in calm water is $\bar{\beta} \approx 3.52°$.

7.2. Regular waves

In Fig. 23 the contribution of the pressure and shear components of the thrust and torque to the total values are shown for the FT simulation in regular wave condition WC2 with the grid $n = 1.00$ at $J \approx 0.55$. The time series are derived from the last encountered wave in the simulation. To be consistent with the other time series provided in Section 6, the time series are synced in order to have the time origin $t/T_E = 0$ as the zero up-crossing of the analytical free surface elevation above the propeller center. This may therefore result in a discontinuity of the time series at $t/T_E \approx 0.41$, as the last encountered wave in the simulation does not necessarily start from the zero up-crossing of the free surface elevation. The time-averaged values (MEAN) are shown in the legends of the plots.

Similar to the calm water simulations, the pressure component of both thrust and torque is the dominant component in WC2. The comparison between calm water and the variation of the total thrust and total torque with respect to the free surface elevation are already discussed in Section 6. The oscillations of the shear component for both thrust and torque remain insignificant during the wave encounter and the values are almost identical to the values in FT simulation in calm water given in Table 5.

The mean values of T_Y, Q_Y and Q_Z are negligible, but the mean of T_Z is significant and similar to the calm water value. On the other hand, these forces and moments slightly vary during the wave encounter that may complicate the model test measurements in waves. For instance, there is inevitable mechanical interference in the experimental setup such as the shaft wobbling in the shaft line casing. Due to these non-axial forces and moments, such wobbling can be intensified, resulting in a varying asymmetric orientation of the propeller relative to the inflow direction during the wave encounter. Consequently, this imposes complex and irregular conversions of the non-uniform and unsteady incident flow field in waves, and in conjunction with the general asymmetric nature of the model tests, they may adversely affect the measurements. Such asymmetric conditions can be speculatively endorsed by noticing the oscillations at the propeller rotation frequency observed in the thrust and torque measurements which are not present in the CFD results, as explained in Section 4.6.3. It is worth mentioning that the oscillations in the propeller rotation frequency also exist in calm water measurements, which may hypothetically reveal the asymmetric nature of the model tests, e.g., minor misalignment of the installed propeller, even when the inflow is approximately uniform. These can be counted as a very important source of discrepancy seen in Sections 5 and 6.

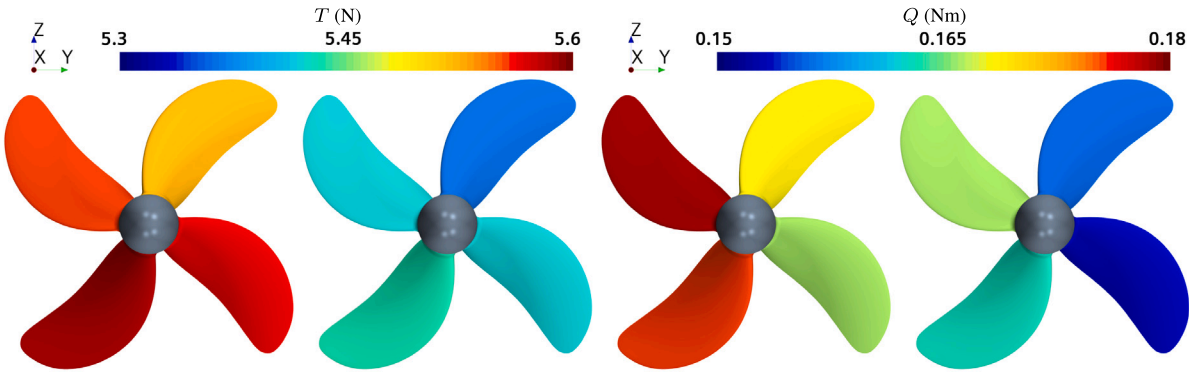

(a) FT simulation thrust. (b) TM simulation thrust. (c) FT simulation torque. (d) TM simulation torque.

Fig. 21. Contribution of each blade to the total thrust and torque in the last time step of the FT and TM simulations at $J \approx 0.55$.

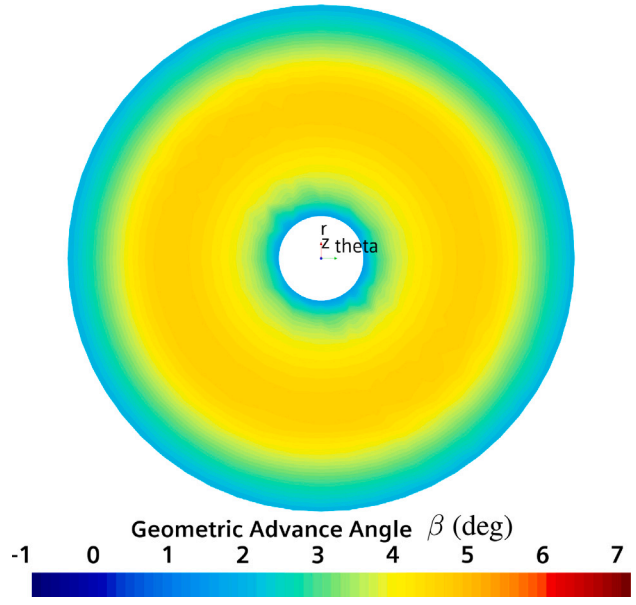

Fig. 22. Geometric advance angle distribution on a representative propeller disk in the calm water simulation at $J \approx 0.55$.

7.2.1. Single-blade analysis

Fig. 24 illustrates the contribution of the pressure and shear components on the total thrust and torque from different blades. The mean values of the total thrust and torque given in the legends of the plots are very similar to the values seen in Figs. 21(a) and 21(c) for different blades in the FT calm water simulation. The pressure component is the dominant component for each blade and the time series of the total thrust and torque mainly follows this component. The variation of the shear component in terms of magnitude remains insignificant for both thrust and torque.

For the thrust in Fig. 24(a), the oscillations are slightly smoothed out close to the wave crest and trough, i.e., near $t/T_E \approx 0.25$ and 0.75, where the values are large/small near wave trough/crest. This is similar to the trend of the thrust on the full geometry that is already justified in Section 6 by the axial component of the wave orbital velocities and its effects on the instantaneous advance ratio. The vertical velocity component of the wave orbital velocities become almost zero close to the wave peak and wave trough, hence the oblique flow environment becomes insignificant which may be counted as the main reason for the smoothed out thrust at these time instances.

On the other hand, the torque time series exhibit very different behavior compared to the thrust. As seen in Fig. 24(f) the shear component of the torque is smoothed out near the wave crest and trough where the vertical component of the wave orbital velocity diminishes. It is also seen that the overall variations of the shear component in terms of magnitude is insignificant throughout one encountered wave period. More importantly, although the blades total torque and their pressure component show a similar behavior as of thrust with respect to the free surface elevation, the oscillations at the propeller rotation frequency are very different. The total torque oscillations, as well as its pressure component, are primarily more pronounced during the time from the wave trough to the wave crest, where the propeller encounters an upward going velocity component, but smaller from the wave crest to the wave trough. Interestingly, all the blades generate similar torque close to $t/T_E \approx 0.33$ which experiences a smoother increase over nearly one full revolution of the blades. This occurs following the passage of wave crest, as the free surface elevation moves towards the zero down-crossing of the wave. At this time, the axial velocity component of the wave orbital velocities towards the propeller is decreasing though still positive, and the vertical velocity component is decreasing from zero towards increasingly negative values. As already seen in Fig. 23, the superimposed blades' thrust and torque demonstrate a smoother variation, opposite to that of individual blades presented in Fig. 24. This implies a smoother engine load variation, however, a more rigorous load variation which may lead to blade vibration and fatigue.

In Fig. 25, the blades' thrust and torque are extracted at four time instances of the free surface elevation with respect to the propeller center, i.e., zero up-crossing, crest, zero down-crossing and trough. In order to be consistent with the corresponding calm water results presented in Section 5, the extracted screenshots are chosen in order to have one of the blades at the azimuthal position $\theta \approx 30°$. Consequently, the extracted screenshots are not representing the exact time instances of the aforementioned wave elevation positions but marginally different. In Fig. 25(a), the schematic position of the analytical and modeled free surface elevation with respect to the propeller is shown in which the dimensions of the propeller as well as the free surface height are exaggerated for a clearer illustration. The waves are propagating towards the propeller, hence the four time instances of zero up-crossing, crest, zero down-crossing and trough are representing $t/T_E \approx 0$, 0.25, 0.5 and 0.75, respectively.

The overall observations in Figs. 24(a) and 24(b) can be endorsed in Figs. 25(b) and 25(c). The thrust on different blades is similar at the time of wave crest and trough, but significantly different at the time of zero up and down crossings. The torque on different blades is more similar at the time of wave crest and zero down-crossing in comparison to the wave trough and zero up-crossing. One interesting point is the smaller thrust and torque on the blades at the azimuthal position $\theta \approx 30°$ and 120° compared to other two blades at the time

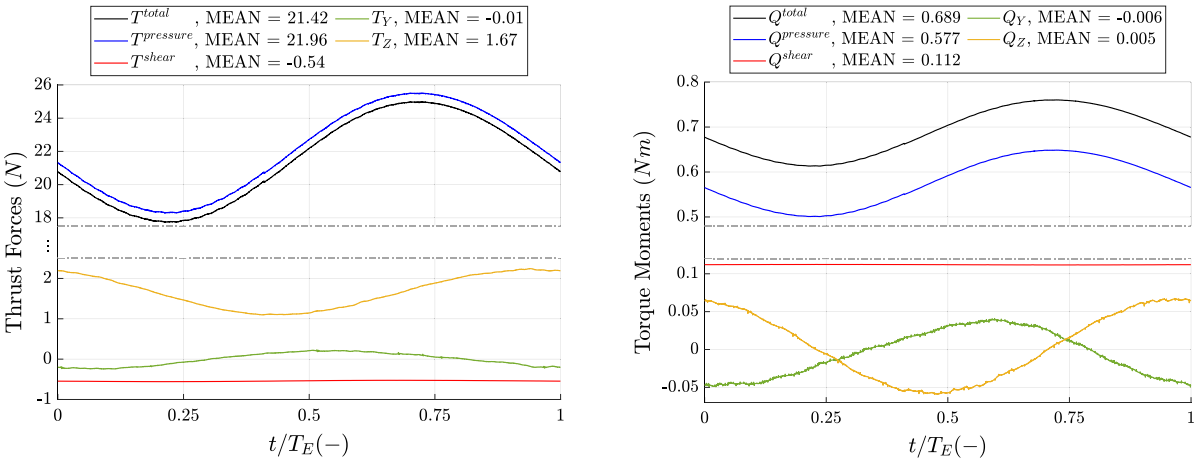

(a) Thrust. (b) Torque.

Fig. 23. Synced time series of the contribution of the pressure and shear components of the thrust and torque to the total values in the FT simulation in WC2 with the grid $n = 1.00$ at $J \approx 0.55$.

of zero up-crossing. Moreover, the thrust and torque on the blades at the azimuthal position $\theta \approx 30°$ and 120° are larger than the other two blades at the time of zero down-crossing. The main cause of load variations on the blades is the non-uniform distribution of the incident inflow that is addressed in the following section.

7.2.2. Incident flow field

In Fig. 26 the axial and vertical components of the wave orbital velocities non-dimensionalized by the advance velocity U as well as the geometric advance angle β on the representative propeller disk are shown at the exact time instances of wave trough, crest, zero up and down crossings with respect to the disk.

The axial component of the wave orbital velocity over the disk is almost zero at the time of zero up and down crossings. For the vertical component this occurs at the time of wave crest and trough. The axial and vertical components are maximum at the wave crest and zero up-crossing, respectively. One important point is that the wave orbital velocities at these time instances are non-uniformly distributed over the disk, since these velocities depend on the depth under the free surface. As a result, the distribution of the geometric advance angle over the disk becomes very complicated, as shown in Fig. 26(c).

At the zero up and down crossings, there is more significant non-uniformity for β in azimuthal direction θ which can explain the differences in the thrust and torque between the blades at $\theta \approx 30°$ and 120° versus the other two blades seen in Figs. 25(b) and 25(c) at these time instances. For instance, larger geometric advance angles are seen for $180° < \theta < 360°$ at the time of wave zero up-crossing which can describe the larger thrust and torque on the blades at $\theta \approx 210°$ and 300° at this time instance. Similarly, the overall small geometric advance angle in radial direction, which is almost uniformly distributed in the azimuthal direction at the time of wave crest, can be the reason for the rather light and similar loading of all blades at this time instance. Interestingly, this scenario is not fully valid at the time of wave trough. Although the value of the geometric advance angle at the wave trough is predominantly significant in the radial direction across the disk (which is the reason for the heavily loaded blades in Fig. 25), the distribution of β in the azimuthal direction is not as uniform as the one seen for the wave crest. At the wave trough, the geometric advance angle is slightly larger roughly in $-90° < \theta < 90°$. This can be explained by the fact that the free surface is closer to the disk at the time of wave trough in comparison to the wave crest, hence more significant variation of the wave orbital velocities with respect to depth is expected.

Although the unsteady and non-uniform distribution of β should be used for performing the single-blade analysis, the surface-averaged value of the geometric advance angle $\tilde{\beta}$ over the representative disk during the wave encounter can explain the variation of loading on the full geometry. The synced time series of $\tilde{\beta}$ is shown in Fig. 27 which represents the lower/higher propeller loading at the wave crest/trough. The values of the geometric advance angle can explain the variation of the propeller open water efficiency, seen in Section 6, during the wave encounter.

The velocity vectors in the rotating reference frame on three sections over the suction side and pressure side of the blade at $\theta \approx 30°$ are shown in Fig. 28 at four time instances of wave. The vectors are colored by the non-dimensionalized radial velocity u_r. The constrained streamlines are also shown. No evident distinction can be seen at different time instances and the velocity vectors and streamlines are very similar. The only observation is a minor difference between the streamlines close to the root on both suction side and pressure side, as the streamlines are slightly more radially directed at the time of wave trough and zero up-crossing. This may results in different trailing root vortex formation at different time instances. Overall the velocity vectors as well as the constrained streamlines are very similar to the calm water FT simulation results in Fig. 10(b).

The magnitude of the wall shear stress, shown in Fig. 29, is very similar for different blades and also at different time instances. This can support the insignificant variations of the shear component of torque in terms of magnitude in Fig. 24. The distribution of the magnitude of wall shear stress in waves mainly remains similar to the distribution in calm water FT simulation seen in Fig. 10(c).

On the other hand, the distribution of the hydrodynamic pressure over different blades and at different time instances of wave are very different. It is clear that the low pressure area on the suction side at the wave trough is more significant on all blades in comparison to other wave instances. At the wave crest, the opposite is valid as the lower pressure area shrank while the higher pressure area on the pressure side is more pronounced. At the zero up and down crossings, the distribution of the hydrodynamic pressure is rather similar. All these observations are basically supporting the conclusions derived regarding the pressure component of the thrust in Fig. 24.

Fig. 30 depicts the Q-criterion isosurface colored by the normalized helicity. The tip vortices for all blades are rather small/large at the time of wave crest/trough, which represents the significance of loading on the blades. It is very interesting that at the time of zero up and down crossings, the tip vortex at different blades is different. However, such

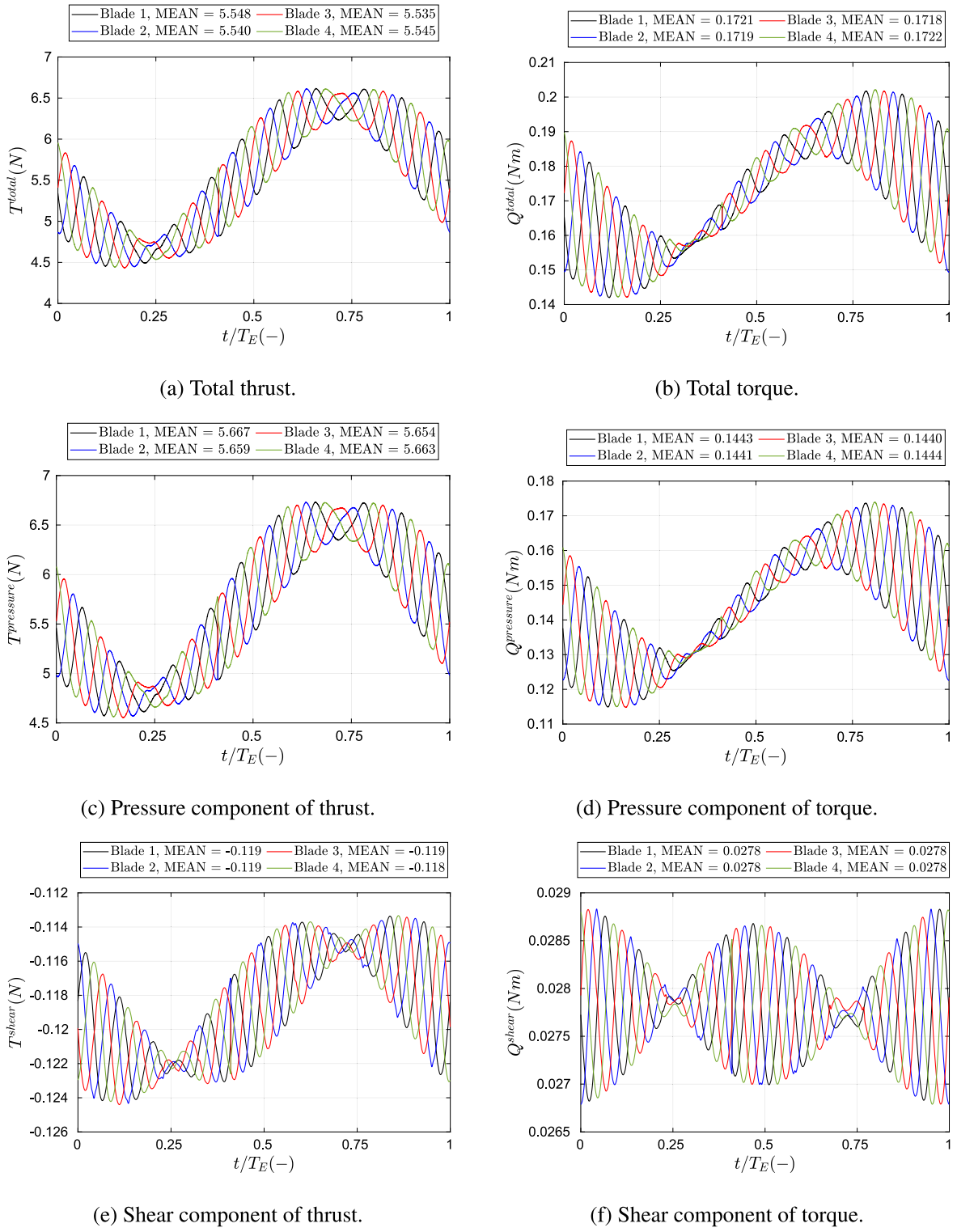

(a) Total thrust.

(b) Total torque.

(c) Pressure component of thrust.

(d) Pressure component of torque.

(e) Shear component of thrust.

(f) Shear component of torque.

Fig. 24. Synced time series of the contribution of the pressure and shear components of the thrust and torque to the total values for different blades in the FT simulation with the grid $n = 1.00$ at $J \approx 0.55$.

differences do not fully represent the loading on the blades. For instance, at the time of the zero up-crossing of the wave, the blades at $\theta \approx 210°$ and 300° are found to have larger thrust and torque in Fig. 25, but in Fig. 31 the largest tip vortices are related to the blades at $\theta \approx 120°$ and 210°. Nevertheless, the tip vortex augmentation and reduction are representing the tip loading which is a local phenomenon. Moreover, based on the Detached Eddy simulations conducted by Di Mascio et al. (2014), for a propeller operating in oblique flow environment, the root and hub vortices interact which brings instabilities to the tip vortices. For the POW in waves, the oblique flow environment is non-uniform and unsteady, hence such interactions become very complicated.

7.3. Computational costs

The computational costs in terms of 1 s of physical time simulations for different grid refinement levels n and advance ratios J are shown

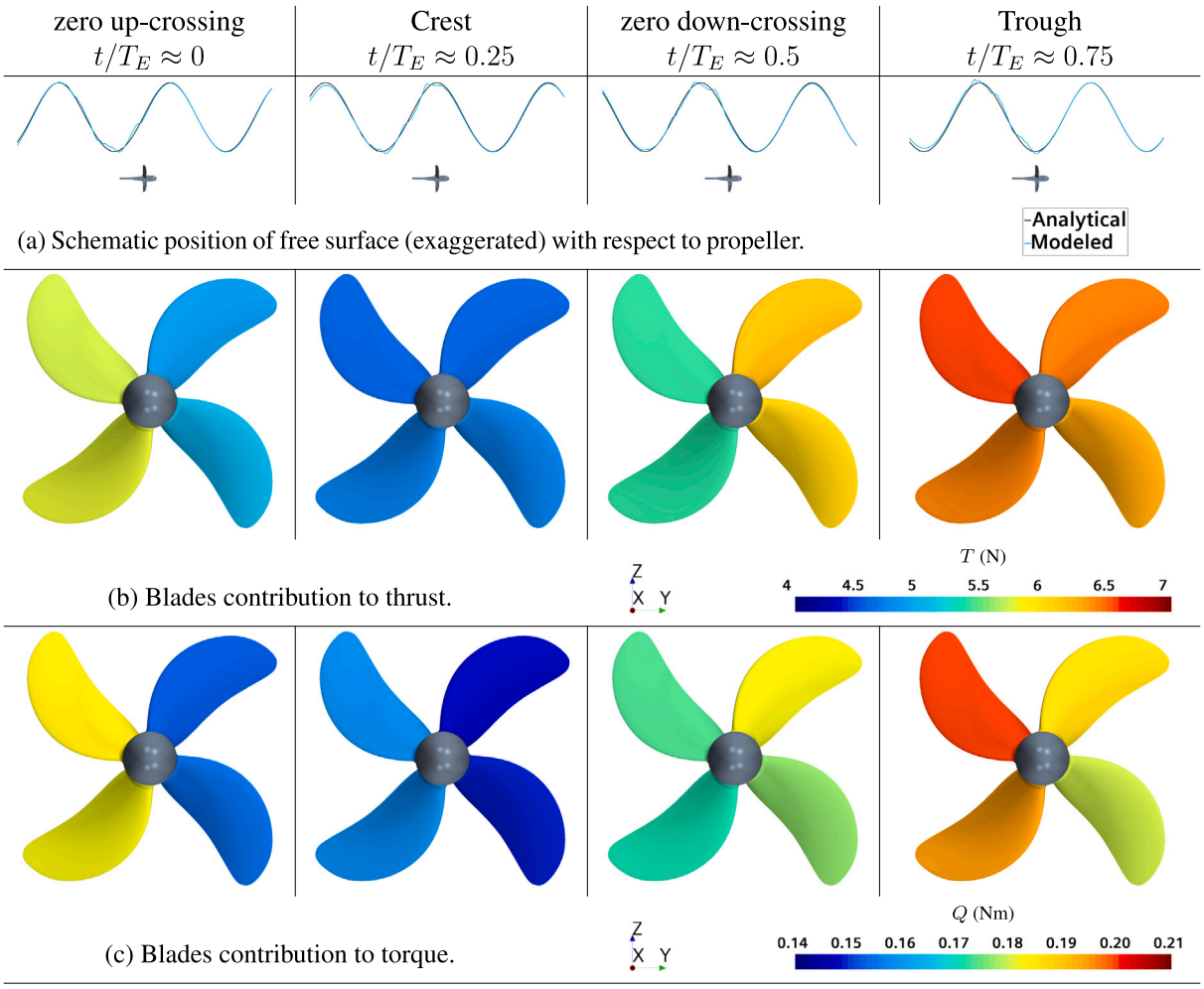

Fig. 25. Contribution of different blades to the total thrust and torque at four time instances of the free surface elevation with respect to the propeller in the FT simulation in WC2 at $J \approx 0.55$.

in Fig. 32. Approximately between 60 000 to 90 000 cells are allocated to each core in different simulations within the parallel computations. Different computing resources (clusters) with different configurations were employed for different simulations, thus there is an inconsistency (bias) in the direct comparison of the computational costs in different simulations. However, the computational costs presented in Fig. 32 can still provide valuable insights for an overall comparison in different simulations.

The computational costs of a TM simulation is larger than the FT simulation in the same grid and advance ratio, because of the additional equations involved in modeling the transition, as discussed in Section 4.1. The desired advance ratios in the simulations are derived from keeping the constant advance velocity (carriage speed) and varying the propeller rotational speed. The time step is chosen to achieve 1° of propeller rotation per time step in the simulations using grid $n = 1.00$. Consequently, the propeller rotational speed and hence the computational costs are lower for the simulations at the higher advance ratios employing this grid. The computational costs are significantly increased at the same advance ratio but higher grid refinement levels, due to the increase of the total number of cells and decrease of the time step (to keep the same Courant number between different grid refinement levels for the grid convergence study).

Since the same models and grid set are used for the simulations in calm water and regular head waves, the computational costs per 1 s of the physical time simulation are almost equal between these operational conditions. However, the total physical time of simulations to obtain the convergence varies in different operational conditions. For instance, the simulation of one encounter wave period demands more computational resources in the longer wave WC4 than the shorter one WC1–WC3, because T_E is larger in WC4. Therefore, the total computational power used for running simulations at different operational conditions cannot be directly perceived by the computational costs given in Fig. 32. A very rough estimation of the total computational costs used for running the FT simulations in calm water and in regular head wave WC2 both with grid $n = 1.00$ at advance ratio $J \approx 0.55$ implies running on 256 cores (CPUs) for 60 h and 100 h, respectively.

8. Conclusions

In this paper, the propeller open water (POW) performance of the KVLCC2 propeller (KP458) in calm water and regular head waves was investigated through systematic experimental and numerical approaches. For the numerical approach, the Computational Fluid Dynamics (CFD) simulations were carried out employing a Reynolds-Averaged Navier–Stokes (RANS) solver. The open water towing tank tests (EFD) and CFD simulations were carried out in five environmental conditions: first in calm water and then in four regular head wave conditions with different wave lengths and heights (WC1 to WC4).

The investigations mainly focused on four advance ratios, i.e., $J \approx 0.35$, 0.45, 0.55 and 0.60, derived from a constant advance velocity

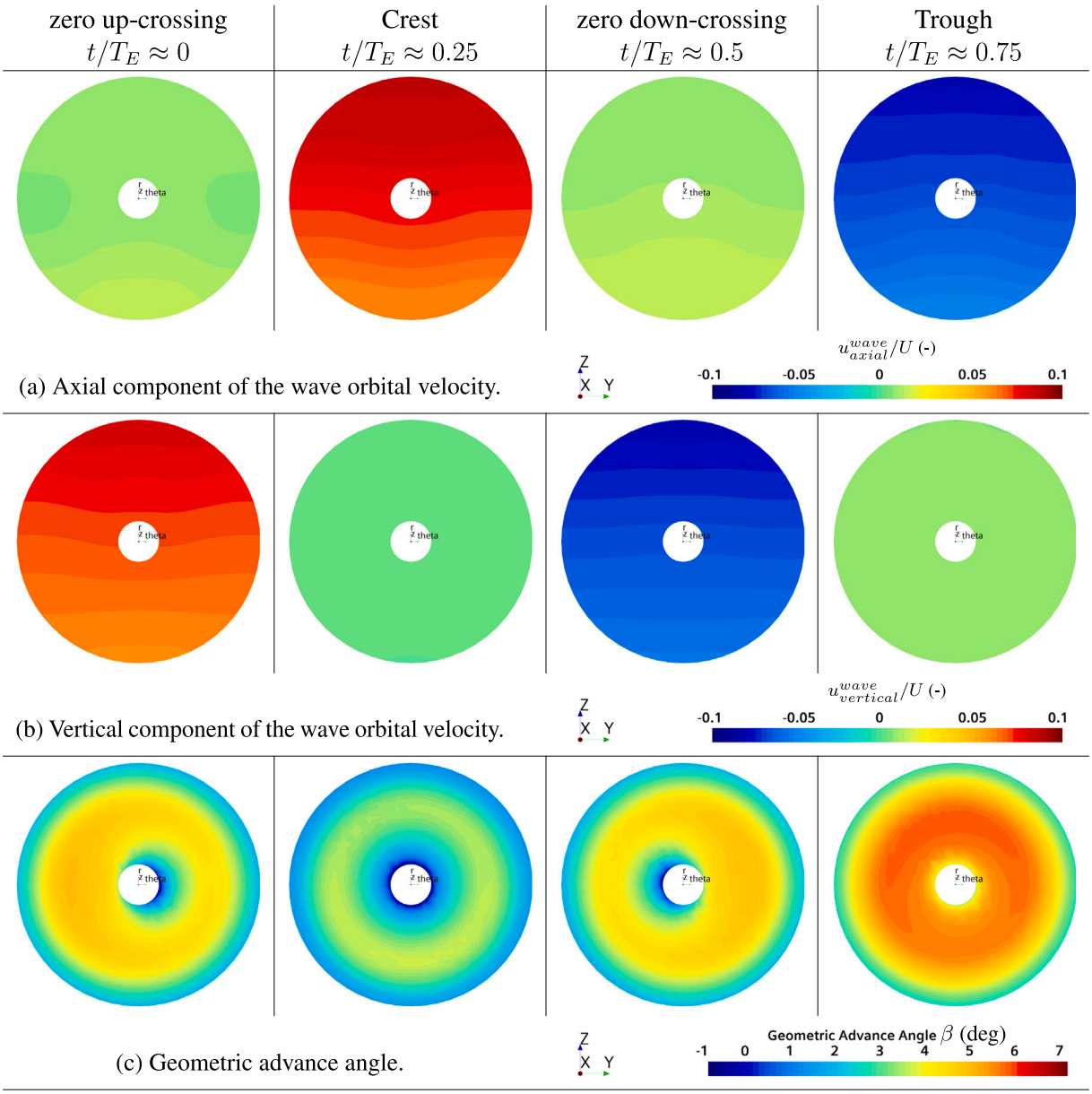

Fig. 26. Wave orbital velocities in axial and vertical directions as well as the geometric advance angle on the representative propeller disk at four time instances of the free surface elevation with respect to the disk in the FT simulation in WC2 at $J \approx 0.55$.

(carriage speed) and varying the propeller rotational speed. The considered advance velocity represents the design speed of KVLCC2 with the same scale factor as of the propeller. The aim was to perform a POW performance evaluation of the propeller under similar operational conditions as the propeller experiences behind the self-propelled KVLCC2 at its design speed, but disregarding propeller–hull interaction effects. Although the propeller with the submergence depth of $3R$ was primarily considered, the submergence effects were briefly examined through a limited analysis of the propeller performance with $2R$ submergence depth. The operational conditions, i.e., submergence depths, advance ratios as well as the environmental and wave conditions, were selected to avoid propeller ventilation during the whole period of encounter, while still being influenced by the incident waves.

The convergence of simulations was examined based on different criteria defined on the propeller thrust and torque in each operational condition using a carefully defined time window for the post-processing of the results. In order to understand and control the numerical and modeling errors in the performed RANS computations, a formal verification and validation (V & V) procedure was applied. The verification analysis, which only concerned the grid convergence study, was carried out in a selective operational conditions using the tool developed by Eça and Hoekstra (2014) based on the Least Squares fits to power series expansions. The simulations were carried out for up to four "as geometrically similar as possible" unstructured grids defined by refinement levels $n = 0.75$, 1.00, 1.25 and 1.50.

Calm Water - V & V

The flow regime, i.e., laminar, transitional or turbulent, on the propeller blades can have significant effects on the open water characteristics of the propeller. Our calm water investigations also revealed significant effects of the flow regime on the propeller performance, particularly evident at higher advance ratios ($J \approx 0.55$ and 0.60). The $\gamma - Re_\theta$ transition model was employed in a series of simulations in order

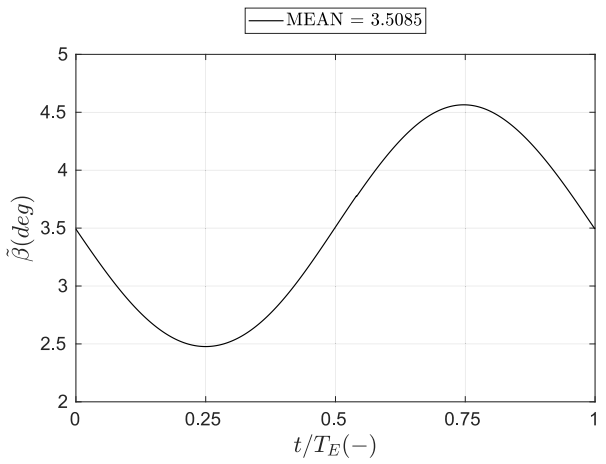

Fig. 27. Synced time series of the surface-averaged geometric advance angle in the FT simulation in WC2 with the grid $n = 1.00$ at $J \approx 0.55$.

to account for the effects of flow regime on the propeller performance. Efforts were made to mitigate the turbulence decay within certain part of the computational domain for a more accurate transition modeling. The towing tank tests in conjunction with the CFD simulations incorporating the transition model TM and the fully turbulent simulations FT (without transition model) revealed that although there was laminar flow dominance on the blades in calm water, the transition to turbulent can also be observed.

Overall, the open water characteristics of the propeller in calm water derived from the TM simulations agreed better than the FT simulations when compared to the EFD results. The validation errors are lower for the TM simulations, especially at higher advance ratios $J \approx 0.55$ and 0.60, where the torque coefficient and hence propeller open water efficiency were predicted with a notably higher accuracy in comparison to the FT simulations. The averaged absolute error $\overline{|E\%D|}$, computed by taking the average of the absolute errors in all advance ratios in calm water, was reduced from FT to TM simulations: approximately from 2.8% to 1.4% for thrust coefficient, from 7.3% to 1.7% for torque coefficient and from 7.6% to 3.1% for propeller efficiency.

The flow field analysis in calm water simulations at $J \approx 0.55$ showed that the constrained streamlines (limiting streamlines) were mainly radially directed in the laminar boundary layer (TM simulation) due to the dominance of the centrifugal forces, but more circumferentially oriented in the turbulent boundary layer (FT simulation) due to the existence of high shear forces. Consequently, lower magnitudes of the wall shear stress were observed on the blades for the TM simulation which might account for the lower torque predictions in this simulation in comparison to the FT simulation. Moreover, the limiting streamlines revealed a more pronounced flow separation on the suction side of the blades in the TM simulation.

The grid convergence study from the TM simulations at $J \approx 0.55$ in calm water resulted in numerical uncertainties approximately between 6% and 8% for both thrust coefficient K_T and torque coefficient K_Q, but smaller 1−4% for the propeller open water efficiency η_O. Since the CFD results from different grids exhibited high similarity, it was suggested that a linear curve fitting could have been a more practical alternative than the second-order method in the employed verification tool.

Regular Head Waves - V & V

From the Fourier analysis performed on the results in regular head waves, mainly the 0th harmonic amplitude (mean value) and the 1st harmonic amplitude which is the dominant harmonic amplitude were examined. The reconstructed time series, representing the time series for one wave encounter period, were also studied.

The reconstructed time series of K_T, K_Q and η_O were decreasing/increasing depending on whether the propeller disk was located in an analytical wave crest/trough. One of the primary contributors to these oscillations was found to be the alteration of the advance ratio, which arose from the temporal change in advance velocity induced by the wave orbital velocities. In the wave crest, the wave orbital velocity in the axial direction becomes maximum, leading to increased advance ratio and thus lower thrust and torque. The opposite holds for the wave trough. This can be perceived by considering the open water curves for K_T and K_Q in calm water and taking into account the temporal changes in advance ratio. The reconstructed time series of η_O exhibited a similar trend to that of K_T and K_Q with respect to the analytical free surface elevation above the propeller in all advance ratios. This cannot be entirely explained by solely relying on the open water curves from calm water. Nonetheless, to get the full picture, it is required to consider the possible effects of both axial and vertical wave orbital velocities on the flow regime as well as any alternation within the associated physical phenomena, such as flow separation, at different operational conditions of the propeller. Therefore, the effects of such unsteady and non-uniform incident flow were analyzed and the geometric advance angle was found to explain the variations of thrust and torque as well as the propeller efficiency as the correlation between the instantaneous thrust and torque.

The CFD investigations in one of the wave conditions (WC2) included both FT and TM simulations at different advance ratios. Based on these simulations as well as the clear change of propeller characteristics from EFD in waves in comparison to calm water, it was concluded that the laminar flow dominance on the blades, which was observed in calm water, might not hold in the case of regular head waves. The reason might lie in the complex change of the incident flow field in waves due to the unsteady and non-uniform oblique flow environment as well as the presumably higher turbulence level generated from the moving wave maker flaps in the towing tank during the tests in waves. Therefore, the TM simulations results in calm water and the FT simulations results in waves were analyzed to understand the impact of waves on the POW performance through the employed CFD approach.

The key observation from the current investigations, in both EFD and CFD, was that the regular head waves affect the time-averaged propeller performance in comparison to calm water, particularly at higher advance ratios. These effects were contemplated to be related to the change of flow regime between calm water and waves, due to the increased turbulence by the wave orbital velocities. According to the CFD investigations using both the FT and TM simulations in calm water and waves, one can speculate that if there was higher turbulence in calm water experiments (minimizing the laminar and transitional flow regimes on the blades), the time-averaged propeller performance in waves and calm water would have been identical. However, this remains as a speculation since there are not enough data in the current study to prove such speculation. A series of propeller open water experimental tests in calm water employing different grids to generate/increase turbulence upstream of the propeller in conjunction with paint tests are recommended as future work to explore such speculations.

In both EFD and CFD, the 0th harmonic amplitudes of K_T, K_Q and η_O (i.e., $\bar{K}_T$, $\bar{K}_Q$ and $\bar{\eta}_O$) in all of the considered waves were clustered at each advance ratio. Therefore, a similar effect from different wave conditions were seen at each advance ratio. In all of the considered wave conditions $\bar{K}_T$ and $\bar{K}_Q$ were decreasing for the higher advance ratios, following the same trend as of calm water curves. However, the trend of $\bar{\eta}_O$ was slightly different from the calm water curve trend at the higher advance ratios. Overall, the largest discrepancies of the 0th harmonic amplitudes between CFD and EFD were seen for $\bar{K}_T$ and $\bar{K}_Q$ at the higher advance ratios $J \approx 0.55$ and 0.60, while $\bar{\eta}_O$ as the correlation between thrust and torque coefficients was agreed better. The averaged absolute error for $\bar{K}_T$, $\bar{K}_Q$ and $\bar{\eta}_O$ in all of the wave conditions and advance ratios were 6.3%, 4.2% and 2.3%, respectively,

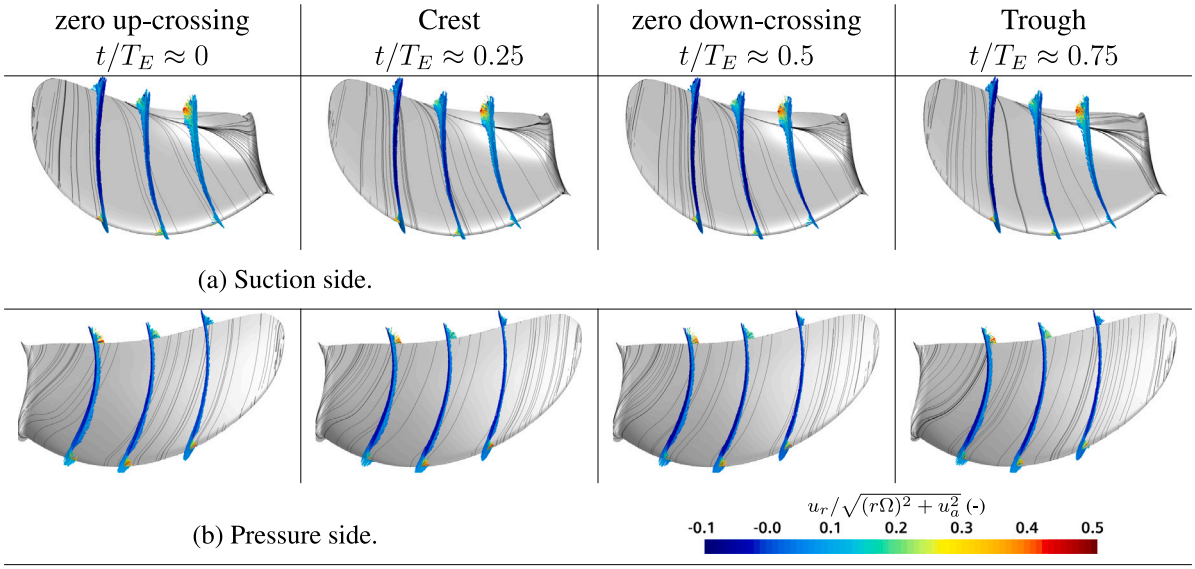

Fig. 28. Velocity vectors on the blade at $\theta \approx 30°$ in the rotating reference frame, colored by the non-dimensionalized radial velocity u_r, at four time instances of the free surface elevation with respect to the propeller in the FT simulation in WC2 at $J \approx 0.55$.

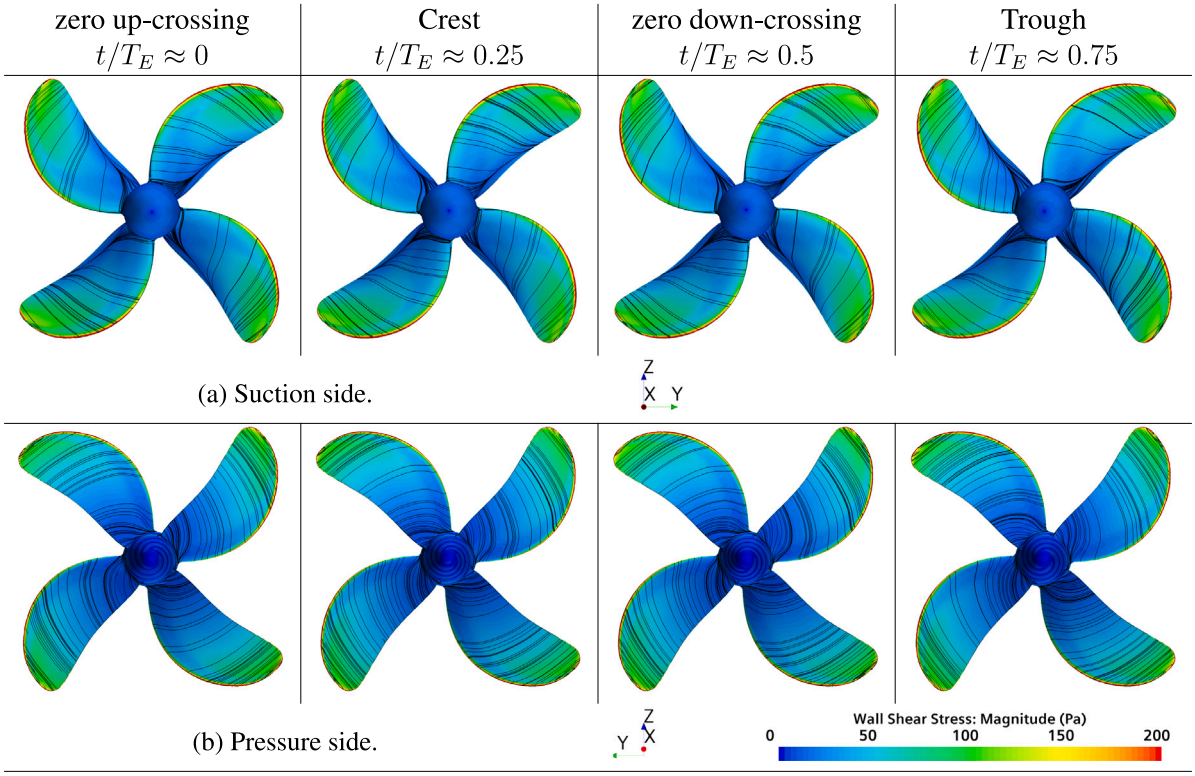

Fig. 29. Magnitude of the wall shear stress at four time instances of the free surface elevation with respect to the propeller in the FT simulation in WC2 at $J \approx 0.55$.

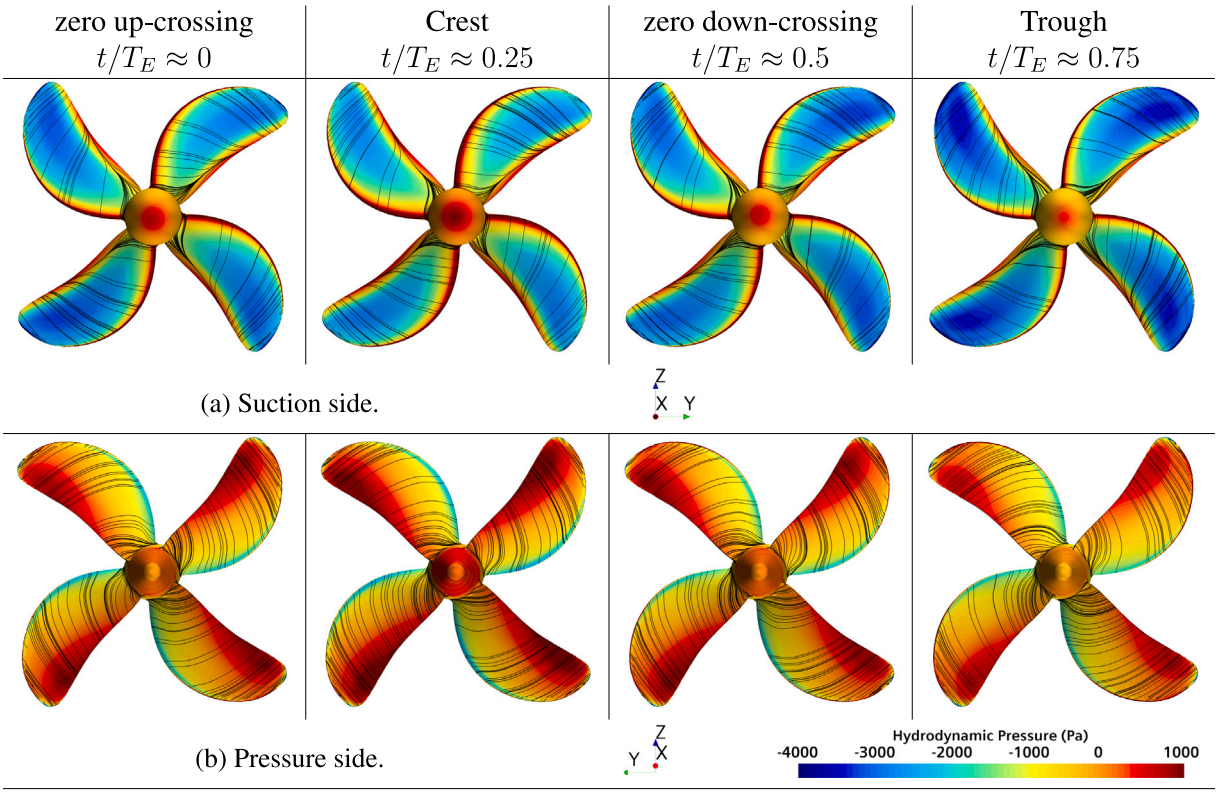

Fig. 30. Hydrodynamic pressure at four time instances of the free surface elevation with respect to the propeller in the FT simulation in WC2 at $J \approx 0.55$.

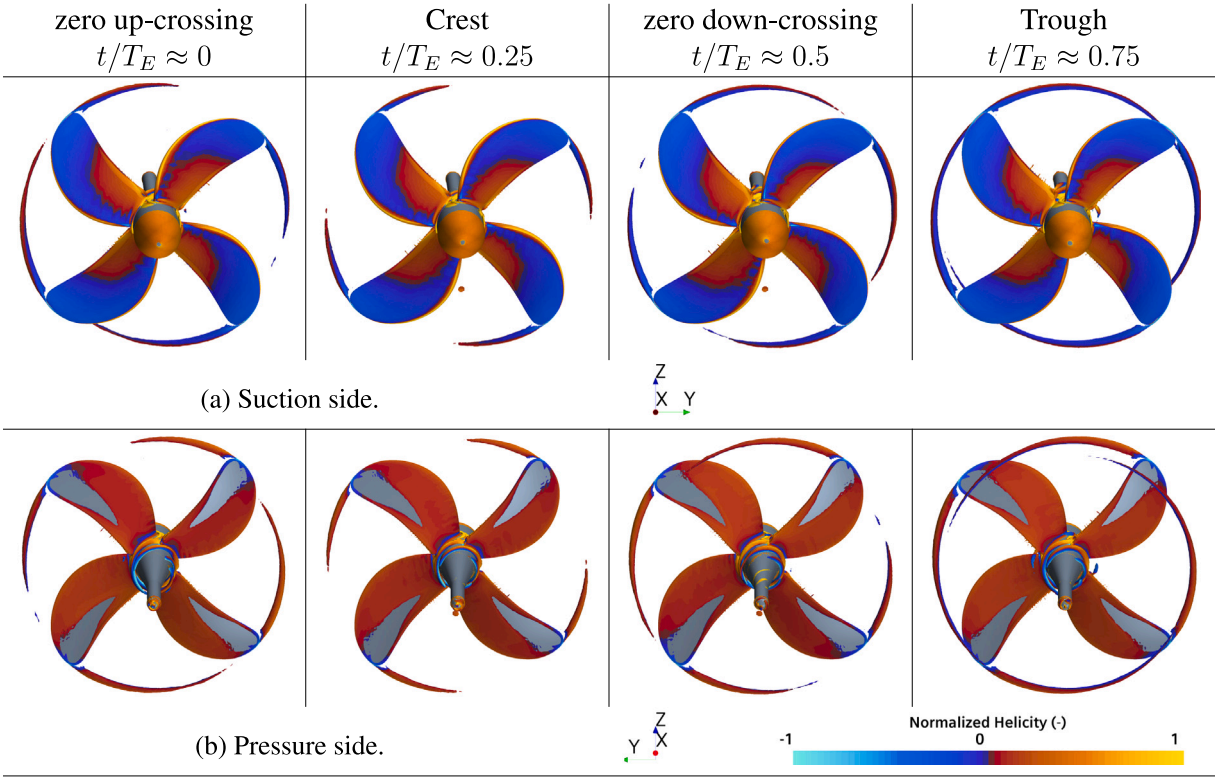

Fig. 31. Q-criterion isosurface colored by the normalized helicity at four time instances of the free surface elevation with respect to the propeller in the FT simulation in WC2 at $J \approx 0.55$.

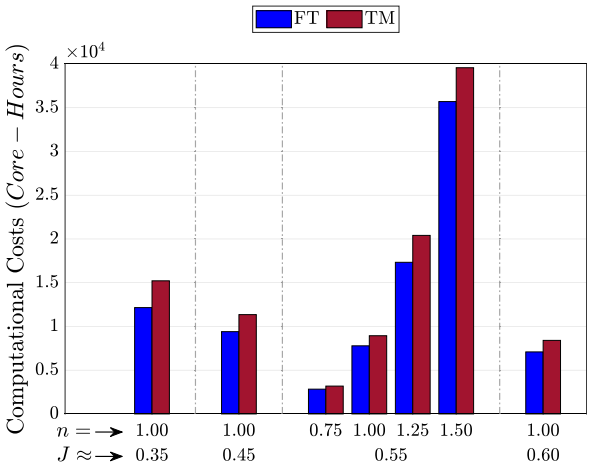

Fig. 32. Approximate computational costs in terms of Core-Hours per 1 s of physical time simulations in calm water and regular head waves.

which are higher than the calm water values for thrust and torque, but slightly lower for efficiency.

In both EFD and CFD, the 1st harmonic amplitudes of K_T, K_Q and η_O (i.e., K_{T1}, K_{Q1} and η_{O1}) were increasing at higher advance ratios in the same wave condition. This may be related to the fact that in the higher advance ratios the propeller rotational speed is lower, hence the effects of the axial component of the wave orbital velocities become more significant on the advance ratio. When the actual measured wave heights were used to normalize K_{T1}, K_{Q1} and η_{O1}, a roughly linear relation between the wave height and the 1st harmonic amplitudes of the propeller characteristics was observed. However, this relation might not hold at the higher advance ratios where the 2nd harmonic amplitudes are not negligible. Moreover, the wave length effects on this relation were not fully resolved through the current considered wave conditions. Overall, K_{T1}, K_{Q1} and η_{O1} were mainly under-predicted by CFD in comparison to EFD and the averaged absolute errors were smaller (2.7% and 4.2%) for the thrust and torque coefficients but very significant (14.8%) for efficiency.

The grid convergence study from the FT simulations in WC2 at $J \approx 0.55$ resulted in numerical uncertainties approximately $0.9-2.8\%$ for $\bar{K}_T$, $2.9-8.4\%$ for $\bar{K}_Q$, and $0.7-1.1\%$ for $\bar{\eta}_O$, which were mainly lower than calm water values. Substantially larger numerical uncertainties were seen for K_{T1}, K_{Q1} and η_{O1}, especially for K_{Q1} and η_{O1} ($36.6-42.9\%$). However, similar to the calm water grid convergence study conclusions, a linear fit might be a better candidate for curve fitting as the results at different grids were rather similar.

Extraction of pressure and shear components of thrust and torque on a single blade through a full encounter period reveals that the dynamics of thrust and torque in waves are predominantly influenced by the pressure component.

Final Remarks

The general results from CFD were promising compared with the experimental measurements. The unsteady and non-uniform oblique flow into propeller are inherent characteristics of waves. The investigations of the incident flow field, e.g., the geometric advance angle derived from the geometric pitch distribution of the blades and the wave orbital velocities over a representative propeller disk, as well as the single-blade force and moment analysis from the CFD investigations revealed the potential sources of discrepancies between EFD and CFD. Asymmetric conditions, such as a slight misalignment of the shaft with respect to the inflow direction, as well as the mechanical interference, e.g., shaft line vibrations and wobbling in the shaft line casing, is inevitable in the experiments. The oscillations observed in the measured thrust and torque, occurring at the propeller rotation frequency, were speculated to be related to such asymmetries, but not proven in the current study. Such oscillations are not present in the CFD results. It is speculated that these vibrations alter the flow over the blades resulting in a different flow transition, separation and development of vortical structures. This in turn leads to a different thrust and torque measurement in the towing tank tests in comparison to the fairly ideal conditions in CFD. The uncertainty of the EFD data should not be overlooked either.

It is important to emphasize that here in this study the RANS approach was employed which inherently includes simplifications and approximations that might have shortcomings in capturing the flow physics. Higher fidelity CFD approaches, such as simulations incorporating Large Eddy simulation, are recommended to be employed in order to carry out similar investigations as the ones performed here. Single-blade force measurements, turbulence level measurements and paint tests in the towing tank experiments could further help understating the flow regime effects, hence recommended for future investigations. Overall, the flow field analyses in this study provided valuable insight into the propeller–wave interaction effects and contributed to the comprehension of the underlying physical mechanisms. One crucial question arising from the current investigations pertains to the turbulence levels present in the flow behind the self-propelled KVLCC2 at model-scale, hence how the flow regime will impact the propeller performance under the self-propulsion conditions in both calm water and regular head waves.

CRediT authorship contribution statement

Mohsen Irannezhad: Writing – review & editing, Writing – original draft, Visualization, Investigation, Formal analysis, Data curation, Conceptualization. **Martin Kjellberg:** Writing – review & editing, Conceptualization. **Rickard E. Bensow:** Writing – review & editing, Conceptualization. **Arash Eslamdoost:** Writing – review & editing, Writing – original draft, Supervision, Resources, Project administration, Funding acquisition, Conceptualization.

Declaration of competing interest

The authors declare that they have no known competing financial interests or personal relationships that could have appeared to influence the work reported in this paper.

Data availability

Data will be made available on request.

Acknowledgments

This research is funded by The Swedish Transport Administration through Lighthouse (Swedish Maritime Competence Center). The experimental measurements are carried out at SSPA Towing Tank. The simulations were performed on the resources provided by the National Academic Infrastructure for Supercomputing in Sweden (NAISS) and the Swedish National Infrastructure for Computing (SNIC) at Chalmers Centre for Computational Science and Engineering (C3SE) and National Supercomputer Center at Linköping University (NSC) partially funded by the Swedish Research Council through grant agreements no. 2022-06725 and no. 2018-05973. Gabriele Mazza is acknowledged for conducting the open water experiments.

Appendix

The reconstructed time series of experimental measurements results in WC1, WC3 and WC4 in $3R$ submergence depth are shown in Figs. A.1–A.3, respectively.

The reconstructed time series from EFD and CFD (only for FT simulations with grid $n = 1.00$) for different wave conditions in $3R$ submergence depth at $J \approx 0.35$, 0.45 and 0.60 are shown in Figs. A.4–A.6, respectively.

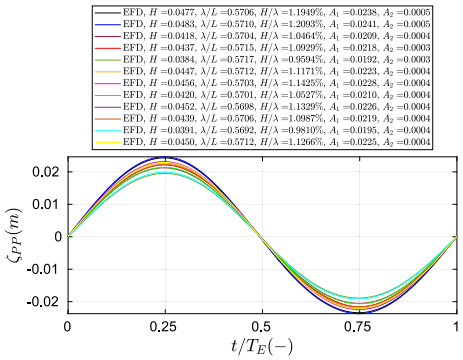

(a) Wave elevation at propeller center.

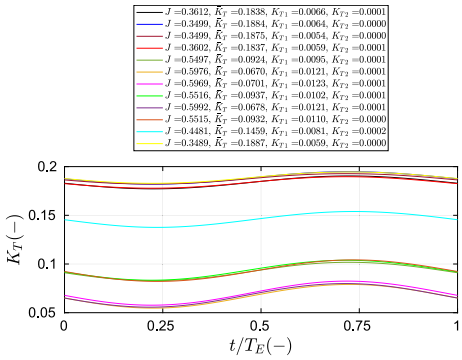

(b) Thrust coefficient.

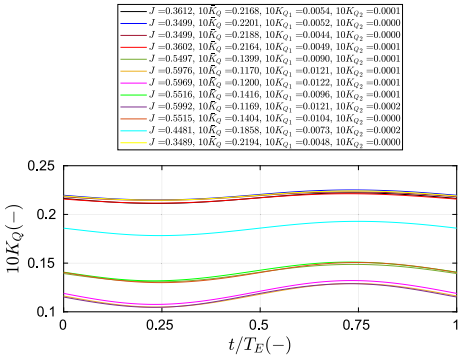

(c) Torque coefficient.

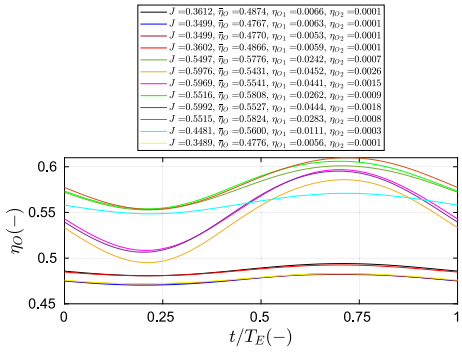

(d) Efficiency.

Fig. A.1. Reconstructed time series of experimental measurements results in wave condition WC1.

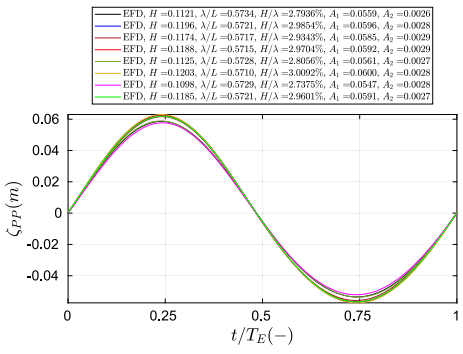

(a) Wave elevation at propeller center.

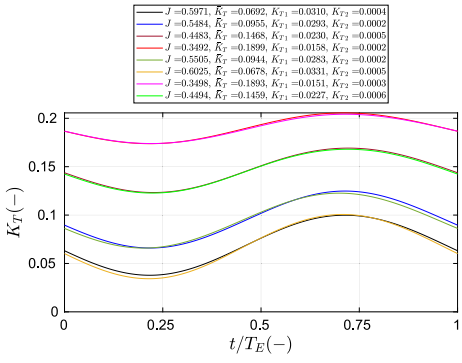

(b) Thrust coefficient.

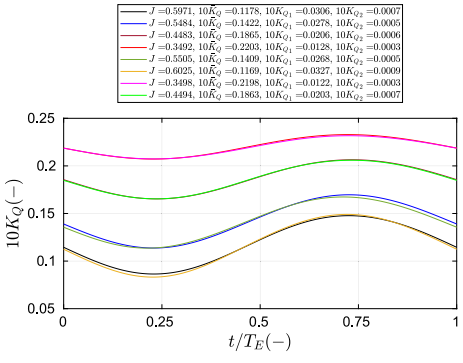

(c) Torque coefficient.

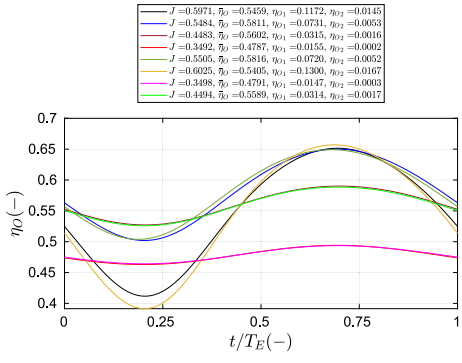

(d) Efficiency.

Fig. A.2. Reconstructed time series of experimental measurements results in wave condition WC3.

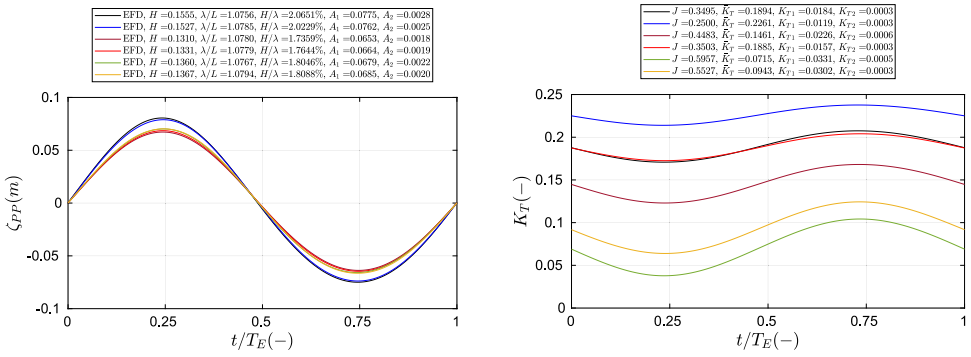

(a) Wave elevation at propeller center.

(b) Thrust coefficient.

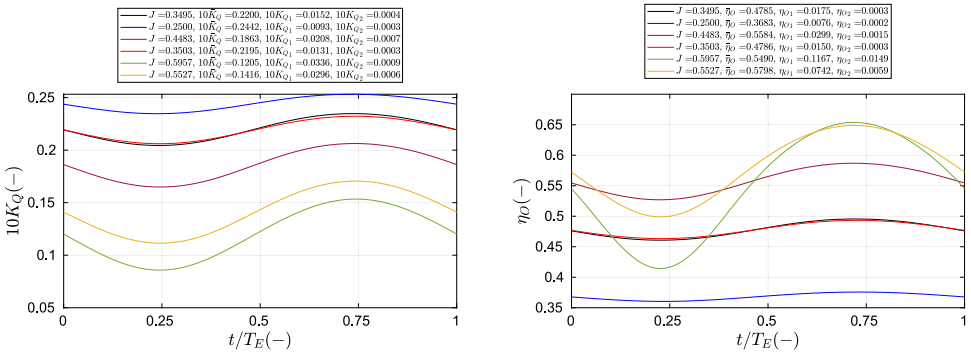

(c) Torque coefficient.

(d) Efficiency.

Fig. A.3. Reconstructed time series of experimental measurements results in wave condition WC4.

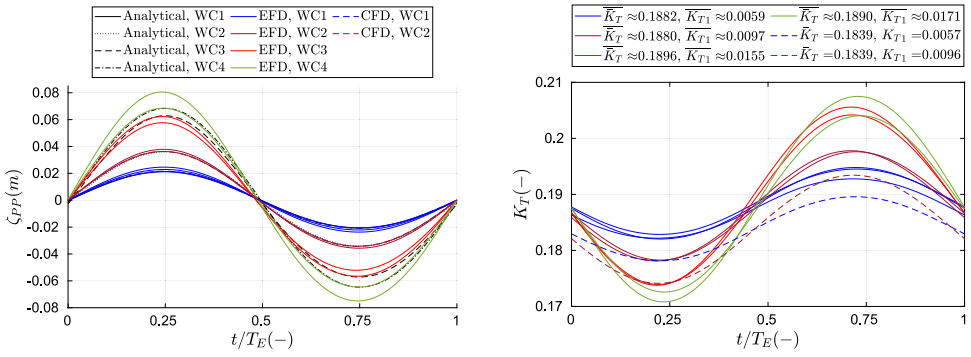

(a) Wave elevation at propeller center.

(b) Thrust coefficient.

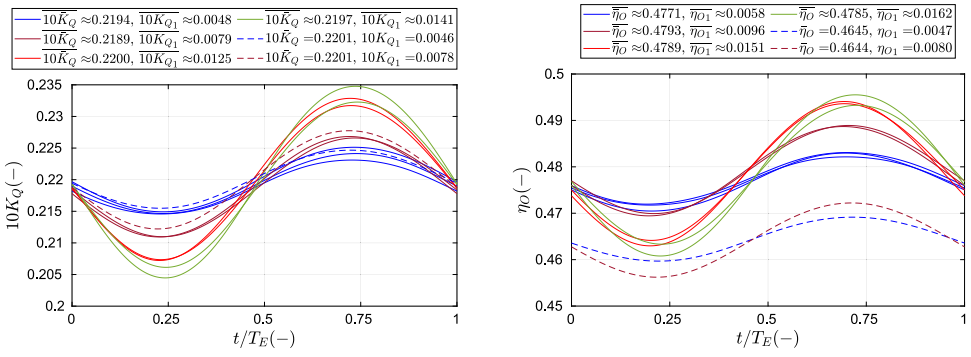

(c) Torque coefficient.

(d) Efficiency.

Fig. A.4. Reconstructed time series from the results of EFD and CFD (only for FT simulations with grid $n = 1.00$) in different wave conditions at $J \approx 0.35$.

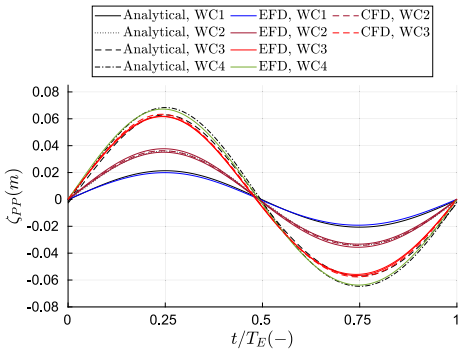

(a) Wave elevation at propeller center.

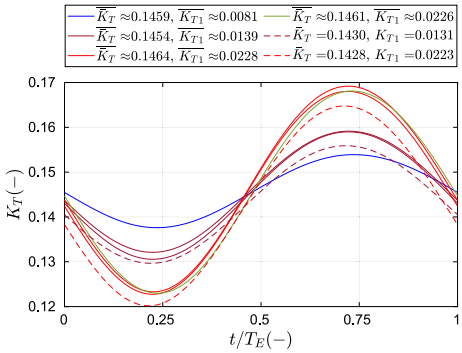

(b) Thrust coefficient.

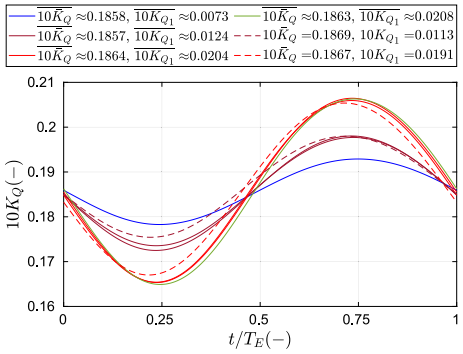

(c) Torque coefficient.

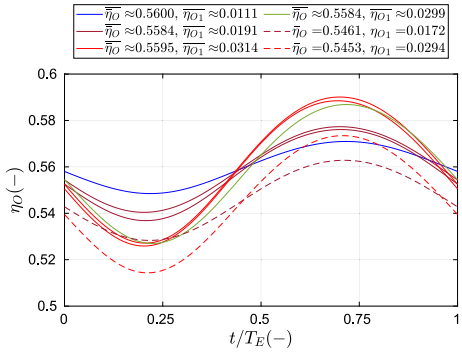

(d) Efficiency.

Fig. A.5. Reconstructed time series from the results of EFD and CFD (only for FT simulations with grid $n = 1.00$) in different wave conditions at $J \approx 0.45$.

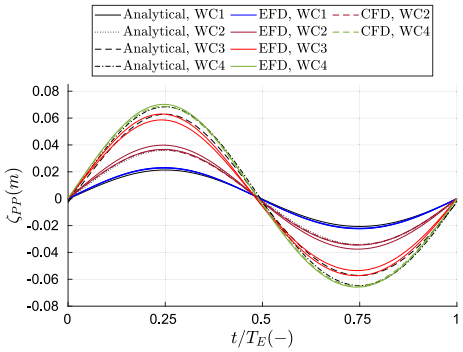

(a) Wave elevation at propeller center.

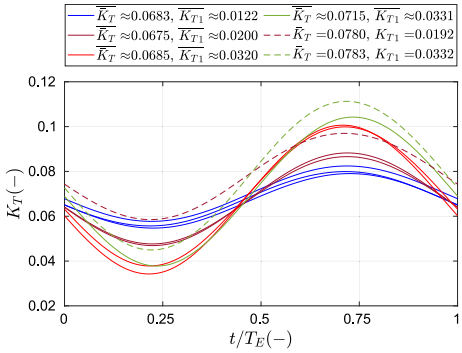

(b) Thrust coefficient.

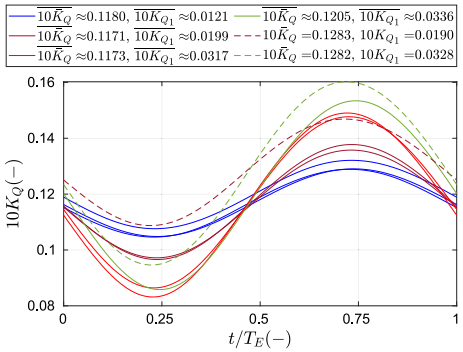

(c) Torque coefficient.

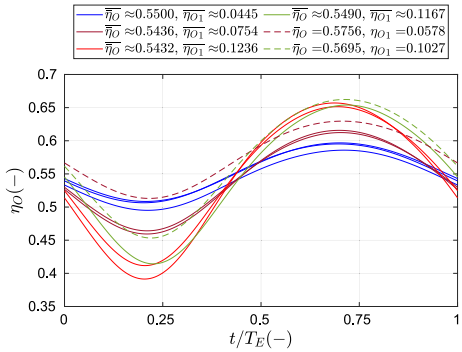

(d) Efficiency.

Fig. A.6. Reconstructed time series from the results of EFD and CFD (only for FT simulations with grid $n = 1.00$) in different wave conditions at $J \approx 0.60$.

References

Baltazar, J., Rijpkema, D., Falcão de Campos, J., 2018. On the use of the $\gamma - Re_{\theta t}$ transition model for the prediction of the propeller performance at model-scale. Ocean Eng. (ISSN: 0029-8018) 170, 6–19. http://dx.doi.org/10.1016/j.oceaneng.2018.10.005.

Baltazar, J., Rijpkema, D., Falcão de Campos, J., 2021. Prediction of the propeller performance at different Reynolds number regimes with RANS. J. Mar. Sci. Eng. (ISSN: 2077-1312) 9 (10), http://dx.doi.org/10.3390/jmse9101115.

Berndt, J.C., Perić, R., Abdel-Maksoud, M., 2021. Improved simulation of flows with free-surface waves by optimizing the angle factor in the HRIC interface-sharpening scheme. J. Appl. Fluid Mech. (ISSN: 1735-3572) 14 (3), 909–920. http://dx.doi.org/10.47176/jafm.14.03.32062, https://www.jafmonline.net/article_1132.html.

Bhattacharyya, A., Krasilnikov, V., Steen, S., 2016. Scale effects on open water characteristics of a controllable pitch propeller working within different duct designs. Ocean Eng. (ISSN: 0029-8018) 112, 226–242. http://dx.doi.org/10.1016/j.oceaneng.2015.12.024.

Bhattacharyya, A., Neitzel, J., Steen, S., Abdel-Maksoud, M., Krasilnikov, V., 2015. Influence of flow transition on open and ducted propeller characteristics. In: Proceedings of the Fourth International Symposium on Marine Propulsors. Austin, Texas, USA, https://api.semanticscholar.org/CorpusID:41386324.

Califano, A., Steen, S., 2011. Numerical simulations of a fully ssubmerged propeller subject to ventilation. Ocean Eng. (ISSN: 0029-8018) 38 (14), 1582–1599. http://dx.doi.org/10.1016/j.oceaneng.2011.07.010.

Crepier, P., 2017. Ship resistance prediction: verification and validation exercise on unstructured grids. In: MARINE VII : Proceedings of the VII International Conference on Computational Methods in Marine Engineering. CIMNE, ISBN: 978-84-946909-8-3, pp. 365–376, http://hdl.handle.net/2117/331841.

Di Mascio, A., Muscari, R., Dubbioso, G., 2014. On the wake dynamics of a propeller operating in drift. J. Fluid Mech. 754, 263–307. http://dx.doi.org/10.1017/jfm.2014.390.

Eça, L., Hoekstra, M., 2014. A procedure for the estimation of the numerical uncertainty of CFD calculations based on grid refinement studies. J. Comput. Phys. (ISSN: 0021-9991) 262, 104–130. http://dx.doi.org/10.1016/j.jcp.2014.01.006.

Eça, L., Klaij, C., Vaz, G., Hoekstra, M., Pereira, F., 2016. On code verification of RANS solvers. J. Comput. Phys. (ISSN: 0021-9991) 310, 418–439. http://dx.doi.org/10.1016/j.jcp.2016.01.002.

Eça, L., Vaz, G., Toxopeus, S.L., Hoekstra, M., 2019. Numerical errors in unsteady flow simulations. J. Verif. Valid. Uncertain. Quant. (ISSN: 2377-2158) 4 (2), 021001. http://dx.doi.org/10.1115/1.4043975.

Eom, M.-J., Jang, Y.-H., Paik, K.-J., 2021a. A study on the propeller open water performance due to immersion depth and regular wave. Ocean Eng. (ISSN: 0029-8018) 219, 108265. http://dx.doi.org/10.1016/j.oceaneng.2020.108265.

Eom, M.-J., Paik, K.-J., Jang, Y.-H., Ha, J.-Y., Park, D.-W., 2021b. A method for predicting propeller performance considering ship motion in regular waves. Ocean Eng. (ISSN: 0029-8018) 232, 109135. http://dx.doi.org/10.1016/j.oceaneng.2021.109135.

Faltinsen, O.M., Minsaas, K.J., Liapis, N., Skjørdal, S.O., 1980. Prediction of resistance and propulsion of a ship in a seaway. In: Proceedings of the 13^{Th} Symposium on Naval Hydrodynamics. Tokyo, pp. 505–529.

Fenton, J., 1985. A fifth-order stokes theory for steady waves. J. Waterway, Port, Coastal Ocean Eng. 111 (2), 216–234. http://dx.doi.org/10.1061/(ASCE)0733-950X(1985)111:2(216).

Gaggero, S., 2022. Influence of laminar-to-turbulent transition on model sscale propeller performances. Part I: Fully wetted conditions. Ships Offshore Struct. 17 (4), 715–727. http://dx.doi.org/10.1080/17445302.2020.1863658.

Gerritsma, J., van den Bosch, J., Beukelman, W., 1961. Propulsion in regular and irregular waves. Int. Shipbuild. Prog. 8 (82), 235–247. http://dx.doi.org/10.3233/ISP-1961-88201.

Irannezhad, M., 2022. Numerical Investigation of Ship Responses in Calm Water and Regular Head Waves. Report No. 2022:04, Department of Mechanics and Maritime Sciences, Chalmers University of Technology, (ISSN: 1652-8565) Thesis for the degree of Licentiate of Engineering, https://research.chalmers.se/publication/530499/file/530499_Fulltext.pdf.

Irannezhad, M., Bensow, R.E., Kjellberg, M., Eslamdoost, A., 2021. Towards uncertainty analysis of CFD simulation of ship responses in regular head waves. In: Proceedings of the 23rd Numerical Towing Tank Symposium. NuTTS 2021, Duisburg, Germany, pp. 37–42, https://www.uni-due.de/imperia/md/content/ist/nutts_23_2021_mulheim.pdf.

Irannezhad, M., Bensow, R.E., Kjellberg, M., Eslamdoost, A., 2023. Comprehensive computational analysis of the impact of regular head waves on ship bare hull performance. Ocean Eng. (ISSN: 0029-8018) 288, 116049. http://dx.doi.org/10.1016/j.oceaneng.2023.116049.

ITTC, 2014. International towing tank conference. Recommended procedures and guidelines 7.5-03-02-03, "practical guidelines for ship cfd applications". In: 27^{th} ITTC, 2014.

ITTC, 2017. International towing tank conference. Recommended procedures and guidelines 7.5-02-03-01.5, "predicting powering margins". In: 28^{th} ITTC, 2017.

ITTC, 2021a. International towing tank conference. final report and recommendations from the resistance and propulsion committee. In: 29^{th} ITTC, 2021.

ITTC, 2021b. International towing tank conference. final report and recommendations from the seakeeping committee. In: 29^{th} ITTC, 2021.

ITTC, 2021c. International towing tank conference. final report and recommendations from the specialist committee on modelling of environmental conditions. In: 29^{th} ITTC, 2021.

Jang, Y.-H., Eom, M.-J., Paik, K.-J., Kim, S.-H., Song, G.-s., 2020. A numerical study on the open water performance of a propeller with sinusoidal pitch motion. Brodogradnja 71, 71–83. http://dx.doi.org/10.21278/brod71105.

Jang, Y.-H., Eom, M.-J., Shin, H.-W., Paik, K.-J., 2019. A numerical study on the propeller performance by the ship motion in regular head waves. In: Proceedings of the 6th International Symposium on Marine Propulsors. SMP'19, Rome, Italy, https://www.marinepropulsors.com/proceedings/2019/THA4-2.pdf, II-485.

Kan, K., Li, H., Yang, Z., 2023. Large eddy simulation of turbulent wake flow around a marine propeller under the influence of incident waves. Phys. Fluids (ISSN: 1070-6631) 35 (5), 055124. http://dx.doi.org/10.1063/5.0152232.

Koushan, K., Spence, S.J.B., Hamstad, T., 2009. Experimental investigation of the effect of waves and ventilation on thruster loadings. In: Proceedings of the 1st International Symposium on Marine Propulsors. SMP'09, Trondheim, Norway.

Langtry, R.B., 2006. A Correlation-Based Transition Model Using Local Variables for Unstructured Parallelized CFD Codes (PhD. thesis). University of Stuttgart, http://dx.doi.org/10.18419/opus-1705.

Lopes, R.M.A., 2021. Simulation of Transition from Laminar to Turbulent Regime in Practical Applications of Incompressible Flow (PhD. thesis). https://scholar.tecnico.ulisboa.pt/records/bV62M9x_O_iZ4CAESvlH8UhVOY5aJAmcA-nj, open-access.

Lopes, R., Eça, L., Vaz, G., Kerkvliet, M., 2021. Assessing numerical aspects of transitional flow simulations using the RANS equations. Int. J. Comput. Fluid Dyn. 35 (3), 157–178. http://dx.doi.org/10.1080/10618562.2020.1870962.

Lopes, R., Eça, L., Vaz, G., Kerkvliet, M., 2022. A technique to control the decay of freestream turbulence for transitional flow simulations. AIAA J. 60 (6), 3565–3580. http://dx.doi.org/10.2514/1.J061266.

Malan, P., Suluksna, K., Juntasaro, E., 2009. Calibrating the Gamma-re_θ transition model for commercial CFD. In: 47th AIAA Aerospace Sciences Meeting Including the New Horizons Forum and Aerospace Exposition. http://dx.doi.org/10.2514/6.2009-1142.

McCarthy, J.H., Norley, W.H., Ober, G.L., 1961. The Performance of a Fully Submerged Propeller in Regular Waves. Report No. 1440, Hydromechanics Laboratory Research and Development Report, David Taylor Model Basin, Washington DC, https://api.semanticscholar.org/CorpusID:107976638.

Menter, F.R., 1994. Two-equation eddy-viscosity turbulence models for engineering applications. AIAA J. 32 (8), 1598–1605. http://dx.doi.org/10.2514/3.12149.

Menter, F.R., Langtry, R.B., Likki, S.R., Suzen, Y.B., Huang, P.G., Volker, S., 2004. A correlation-based transition model using local variables—Part I: Model formulation. J. Turbomach. (ISSN: 0889-504X) 413–422. http://dx.doi.org/10.1115/1.2184352.

Minsaas, K.J., Faltinsen, O.M., Persson, B., 1983. On the importance of added resistance, propeller immersion and propeller ventilation for large ships in a seaway. https://api.semanticscholar.org/CorpusID:108043054.

Moor, D.I., Murdey, D.C., 1970. Motions and propulsion of single screw models in head seas, Part II. Trans. R. Inst. Nav. Archit. 112 (2).

Muzaferija, S., Perić, M., 1998. Computation of free surface flows using interface-tracking and interface-capturing methods. In: Mahrenholtz, O., Markiewicz, M. (Eds.), Nonlinear Water Wave Interaction. WIT Press, Computational Mechanics Publications, Southampton, pp. 59–100.

Nakamura, S., Naito, S., 1975. Propulsive performance of a container ship in waves. J. Soc. Nav. Archit. Jpn 15 (158), 24–48.

Nakamura, S., Naito, S., Inoue, R., 1975. Open-water characteristics and load fluctuations of a propeller in waves. J. Kans. Soc. Nav. Arch., Jpn (159), 41.

Perić, R., Abdel-Maksoud, M., 2018. Analytical prediction of reflection coefficients for wave absorbing layers in flow simulations of regular free-surface waves. Ocean Eng. (ISSN: 0029-8018) 147, 132–147. http://dx.doi.org/10.1016/j.oceaneng.2017.10.009, https://www.sciencedirect.com/science/article/pii/S0029801817306066.

Perić, R., Abdel-Maksoud, M., 2020. Reducing Undesired Wave Reflection at Domain Boundaries in 3D Finite Volume-Based Flow Simulations via Forcing Zones. J. Ship Res. (ISSN: 0022-4502) 64 (01), 23–47. http://dx.doi.org/10.5957/jsr.2020.64.1.23.

Perić, R., Vukčević, V., Abdel-Maksoud, M., Jasak, H., 2022. Optimizing wave generation and wave damping in 3D-flow simulations with implicit relaxation zones. Coast. Eng. (ISSN: 0378-3839) 171, 104035. http://dx.doi.org/10.1016/j.coastaleng.2021.104035, https://www.sciencedirect.com/science/article/pii/S0378383921001794.

Politis, G.K., 1999. Ventilated marine propeller performance in regular and irregular waves; An experimental investigation. In: WIT Transactions on Modelling and Simulation vol 21. https://www.witpress.com/Secure/elibrary/papers/CMEM99/CMEM99017FU.pdf.

Roache, P.J., 1998. Verification of codes and calculations. AIAA J. 36 (5), 696–702. http://dx.doi.org/10.2514/2.457.

Sigmund, S., 2019. Performance of Ships in Waves (Ph.D. thesis). http://dx.doi.org/10.17185/duepublico/70021.

2020. Simcenter STAR-CCM+ user guide. Version 2020.3.

Tavakoli, S., Khojasteh, D., Haghani, M., Hirdaris, S., 2023. A review on the progress and research directions of ocean engineering. Ocean Eng. (ISSN: 0029-8018) 272, 113617. http://dx.doi.org/10.1016/j.oceaneng.2023.113617, https://www.sciencedirect.com/science/article/pii/S002980182300001X.

Tokgoz, E., Wu, P.-C., Takasu, S., Toda, Y., 2017. Computation and experiment of propeller thrust fluctuation in waves for propeller open water condition. J. Jpn Soc. Nav. Archit. Ocean Eng. 25, 55–62. http://dx.doi.org/10.2534/jjasnaoe.25.55.

Van Sluijs, M.F., 1972. Performance and Propeller Load Fluctuations of a Ship in Waves. Report No. 163 S, Netherlands Ship Research Centre TNO, https://repository.tudelft.nl/islandora/object/uuid:393be90b-6d2d-48d4-ae64-c5429d972075/datastream/OBJ.

Xin, C., 2012. Experimental research on hydrodynamic characteristics of propeller in waves. J. Ship Mech. https://api.semanticscholar.org/CorpusID:123360792.

Yao, H., Zhang, H., 2018. Numerical simulation of boundary-layer transition flow of a model propeller and the full-scale propeller for studying scale effects. J. Mar. Sci. Technol. 23, http://dx.doi.org/10.1007/s00773-018-0528-4.

Zhang, W., Ma, N., Gu, X., Feng, P., 2021a. Dynamic loads and thrust hysteresis of near-surface open propeller in regular head waves - an experimental study in a circulating water channel. Ocean Eng. (ISSN: 0029-8018) 219, 108359. http://dx.doi.org/10.1016/j.oceaneng.2020.108359, https://www.sciencedirect.com/science/article/pii/S0029801820312671.

Zhang, W., Ma, N., Gu, X., Feng, P., 2021b. RANS simulation of open propeller dynamic loads in regular head waves considering coupled oblique-flow and free-surface effect. Ocean Eng. (ISSN: 0029-8018) 234, 108741. http://dx.doi.org/10.1016/j.oceaneng.2021.108741, https://www.sciencedirect.com/science/article/pii/S0029801821001761.

Zhao, Q., Guo, C., Su, Y., Liu, T., Meng, X., 2017. Study on unsteady hydrodynamic performance of propeller in waves. J. Mar. Sci. Appl. 16 (3), 305–312. http://dx.doi.org/10.1007/s11804-017-1419-5.